CONVENTIONAL AND FLASH SINTERING OF STOICHIOMETRIC ALKALINE OR NIOBIUM EXCESS SODIUM POTASSIUM NIOBATE CERAMICS

by

GULCAN CORAPCIOGLU

Submitted to the Graduate School of Engineering and Natural Sciences
in partial fulfillment of
the requirements for the degree of
Doctor of Philosophy

Sabancı University
May 2016

CONVENTIONAL AND FLASH SINTERING OF
STOICHIOMETRIC ALKALINE OR NIOBIUM EXCESS
SODIUM POTASSIUM NIOBATE CERAMICS

APPROVED BY:

Prof. Dr Mehmet Ali Gülgün.....
(Thesis Supervisor)

Assoc. Prof. Dr. Cleva Ow-Yang.....

Assoc. Prof. Dr. Burc Mısırlıoğlu.....

Prof. Dr. Miran Ceh.(Jozef Stefan Institute) .....

Assoc. Prof. Dr. Ebru Menşur Alkoy (Maltepe Üniversitesi) .....

DATE OF APPROVAL: 10/05/2016

ABSTRACT

CONVENTIONAL AND FLASH SINTERING OF
STOICHIOMETRIC ALKALINE OR NIOBIUM EXCESS
SODIUM POTASSIUM NIOBATE CERAMICS

GULCAN CORAPCIOGLU

PhD Dissertation, May 2016

Supervisor: Prof. Dr. Mehmet Ali Gulgun

Keywords: Lead-free piezoelectric, sodium potassium niobate (KNN), conventional sintering, flash sintering, grain boundary, scanning transmission electron microscopy (STEM), electron diffraction

This study investigated conventional and flash sintering of stoichiometric, alkaline or niobium excess sodium potassium niobate ceramics. Two shrinkage rate peaks were observed for alkaline excess composition whereas a single shrinkage rate peak (higher temperature peak) was observed for stoichiometric ($K_{0.5}Na_{0.5}NbO_3$) and niobium excess compositions by dilatometry. Sintering analysis showed that transient liquid phase sintering was the active sintering mechanism for alkaline excess composition. The low temperature shrinkage rate peak was related to pre-melted liquid film that facilitates the rearrangement of grains during the initial stages of sintering. The reason for this liquid

film produced by alkaline excess was explained by the low eutectic temperature (710°C) of Na_2CO_3-K_2CO_3 system.

94% theoretical density was obtained in 30 second with 250 V/cm. electric-field, 20 mA/mm^2 current density, at 990°C by flash sintering. Compared to conventional sintering conditions, 1100°C for 2-8 hours, the temperature and duration decrease were very important. Chemical composition of flash sintered sample was investigated using a scanning electron microscope, SEM and a scanning transmission electron microscope (STEM) equipped with an energy-dispersive X-ray spectroscopy (EDX) detector. EDX mapping analysis, revealed a core-shell type microstructure where K-rich regions seemed to constitute the shell around the Na-rich regions while O and Nb distributions were homogenous. Na and K heterogeneity was observed within the grain. The temperature reached during flash was predicted with the help of $KNbO_3$-$NaNbO_3$ equilibrium phase diagram. Core-shell formation was explained by grain boundary melting via Joule heating. Electron diffraction studies and TEM-dark field images showed that chemical boundaries were not coinciding with structural boundaries as would be expected. Extra diffraction spots were observed in the Na rich core region.

The lowest flash sintering temperature was achieved in alkaline excess composition for DC and AC electric-fields. Isothermal experiments showed that alkaline excess composition had the shortest incubation time.

ÖZET

STOKİYOMETRİK ALKALİ VEYA NİOBYUM EXCESS
SODYUM POTASYUM NİOBAT SERAMİKLERİN
KONVANSİYONEL VE FLASH SİNTERLENMESİ

GÜLCAN ÇORAPCIOĞLU

PhD, Mayıs 2016

Danışman: Prof. Dr. Mehmet Ali Gülgün

Anahtar Kelimeler: Kurşunsuz piezoelektrik, sodyum potasyum niyobat (KNN), konvansiyonel sinterleme, flash sinterleme, tane sınırı, taramalı geçirimli elektron mikroskopu (STEM), elektron diffraksiyonu

Bu çalışmada sitokiyometrik ($K_{0.5}Na_{0.5}NbO_3$), alkalice zengin (Na ve K) ve niobiumca zengin (Nb) sodyum potasyum niobat (KNN) kompozisyonlarının, konvansiyonel ve flash sinterleme teknikleri ile sinterleme davranışını incelenmiştir. Dilatometre analizleri sonucunda alkalice zengin kompozisyonda iki tane küçülme hızı piki gözlenirken sitokiyometrik ve niobiumca zengin kompozisyonda bir tane küçülme hızı piki (yüksek sıcaklık piki) gözlenmiştir. Sinterleme analizleri sonucunda alkalice zengin kompozisyonda geçici sıvı faz sinterlemesinin aktif mekanizma olduğu belirlenmiştir. Düşük sıcaklıkta gözlenen küçülme hızı piki erimiş sıvı film ile ilişkili olup sinterlemenin başlangıç aşamasında tanelerin yeniden düzenlenmesine yardımcı

olmaktadır. Alkali fazlası sonucu elde edilen sıvı faz Na_2CO_3-K_2CO_3 sisteminin düşük ötektik erime sıcaklığı (710°C) ile açıklanmıştır.

Flash sinterleme ile 94% teorik yoğunluk 990°C de 30 sn. içerisince 250 V/cm electrik alanı ve 20 mA/mm^2 akım yoğunluğu altında elde edilmiştir. Konvansiyonel sinterleme koşulları olan 1100°C, 2-8 saat ile karşılaştırıldığında sıcaklık ve sürede elde edilen düşüş önemlidir.

Flash sinterleme yapılan numunenin kimyasal kompozisyonu taramalı elektron mikroskobunda (SEM) ve taramalı geçirimli elektron mikroskobunda (STEM) enerji dağılımlı X-Ray spektroskopisi (EDX) ile incelenmiştir. EDX haritalaması, O ve Nb dağılımının homojen olduğunu, ancak potasyumca zengin bölgenin sodyumca zengin bölgeyi çevrelediği core-shell tipi bir mikroyapıya sahip olduğunu göstermiştir. Sodyum ve potasyumdaki heterojen dağılımın tane içerisinde de olduğu belirlenmiştir. Flash sırasında ulaşılan sıcaklık $KNbO_3$-$NaNbO_3$ faz digramı yardımı ile tespit edilmiştir. Core-shell yapının oluşumu Joule heating nedeni ile tane sınırındaki erime ile açıklanmıştır. Elektron diffraksiyon çalışmaları ve TEM-Dark field analizleri kimyasal sınırların beklenildiği gibi tane sınırları ile aynı olmadığını göstermiştir. Sodyumca zengin olan bölgelerde extra difraksiyon noktaları tespit edilmiştir

DC ve de AC electric-field altında en düşük flash sinterleme sıcaklığı alkalice zengin kompozisyonda elde edilmiştir. İzotermal denemeler en kısa inkübasyon süresinin alkalice zengin kompozisyona ait olduğunu göstermiştir.

ACKNOWLEDGEMENT

I would like to express my special appreciation to my supervisor Prof. Dr. Mehmet Ali Gulgun for the opportunity of working with him. I would like to thank you for your unconditional support, encouraging my research, and guide me to grow as a research scientist. You are a great mentor. It was a great privileged to know you and work with you.

I would like to thank to Assoc. Prof. Dr. Cleva Ow-Yang for supporting and guiding me. Your advices are valuable.

I would like to thank to Assoc. Prof. Saso Stum for his support and guidance.

I would like to acknowledged the members of my thesis jury, Assoc. Prof. Dr. Cleva Ow-Yang, Prof. Dr. Miran Ceh, Assoc. Prof. Dr. Burc Mısırlıoglu, Assoc. Prof. Dr Ebru Mensur Alkoy, for their support.

I would like to thank to Prof. Rishi Raj for giving me the opportunity of working with his group at University of Colorado at Boulder, USA. Special thanks to Dr. Jean-Marie Lebrun, Dr. Shikhar K. Jha, Lilian Menezes and Timothy Morrissey for their friendship and support.

I would like to thank to Kim Kisslinger at Brookhaven National Laboratory for his support on TEM sample preparation.

Gratitude to all my colleagues and friends at MAT-SU for providing a positive and a friendly environment. I am grateful to Dr. Guliz Inan Akmehmet, Sorour Parapar, Melike Mercan Yıldızhan, Dr. Shalima Shawuti and all group members for sharing the joy of life, science and friendship.

Special thanks to Turgay Gonul, and Burcin Yıldız for their valuable supports.

I would like to thank to the administrative and technical secretary staff of SU-MDBF and SU-SUNUM for their guidance and assistance.

I am also highly thankful to my family and friends for their support and unconditional love.

Finally, I would like to acknowledge the financial and technical support of the Turkish Foundation for Fundamental Research (TUBITAK), TUBITAK Fellowship Program (2214/A- Grant 1059B141300914), Colorado University and Sabancı University.
This research used resources of the Center for Functional Nanomaterials, which is a U.S. DOE Office of Science Facility, at Brookhaven National Laboratory under Contract No. DE-SC0012704
Special thanks to everything that support and guide me all those years...

Knowledge should mean a full grasp of knowledge
Knowledge means to know yourself, heart and soul.
If you have failed to understand yourself,
Then all of your reading has missed its call

Yunus Emre

Gulcan Corapcioglu

TABLE OF CONTENTS

LIST OF FIGURES

LIST OF TABLES

LIST OF ABBREVIATIONS

AC:	Alternatif current
AFM:	Atomic force microscopy
BF:	Bright field
BLSF:	Bismuth layer-structured ferroelectrics
BNT:	Bizmuth sodium titanate
BKT:	Bizmuth potassium titanate
BSE:	Back scattered electron
CCD:	Charged-coupled device
DC:	Direct Current
DF:	Dark field
DTA:	Differential Thermal Analysis
EDX:	Energy Dispersive X-Ray Spectroscopy
EIS:	Electrochemical Impedance Spectroscopy
EELS:	Electron Energy Loss Spectroscopy
FIB:	Focus Ion Beam
HP:	Hot pressing
ICP:	Inductively coupled plasma
JCPDS:	Joint Committee on Powder Diffraction Standards
HR-TEM:	High Resolution Transmission Electron Microscopy
KCT:	Potassium cupper tantalate

KNN:	Sodium potassium niobate
LKNN:	Lityum modified Sodium potassium niobate
LKNNT:	Lithium and tantalum modified sodium potassium niobate
PZT:	Lead zirconate titanate
PZN-PT:	Lead zinc nionate-lead titanate
PMN-PT:	Lead magnesium nionate-lead titanate
PVB:	Polyvinyl butyral
RT:	Room Temperature
RoHS:	Restriction of the use of certain hazardous substances in electrical and electronic equipment
SEM:	Scanning Electron Microscopy
SOFC:	Solid Oxide Fuel Cell
STA:	Simultaneous Thermal Analysis
STEM:	Sacanning transmission electron microscope
STM:	Scanning tunneling microscope
SPS:	Spark plasma sintering
TEM:	Transmission Electron Microscopy
ThD:	Theoretical density
TPB:	Triple Phase Boundary
TGA:	Thermal Gravimetric Analysis
UTHSCSA:	University of Texas Health Science Center San Antonio
XRD:	X-Ray Diffraction
YSZ:	Yttria stabilized zirconia
Y-TZP:	Yttria stabilized tetragonal zirconia phase
WEEE:	Waste electrical and electronic equipment

CHAPTER 1

1. INTRODUCTION

1.1. Piezoelectricity

"Piezo" is a Greek word meaning "to squeeze". Piezoelectric effect is known as production of electric charge when force is applied to the material. This reversible phenomenon is referred to as the direct piezoelectric effect or generator action . When electric field is applied to the material, mechanical deformation occurs. This phenomenon refers to converse piezoelectric effect or motor action.

Piezoelectricity was first discovered by Pierre and Jacque Curie in 1880. They observe piezoelectricity in the crystals of tourmaline, quartz, topaz, cane sugar, and Rochelle salt. In 1881, the term "piezoelectricity" was first suggested by W. Hankel, and the converse effect was deduced by Lipmann from thermodynamics principles. Nowadays, piezoelectric materials, being the largest group of smart-functional electronic materials, used for various applications such as actuator, transducer and sensor.

The microscopic origin of the piezoelectric effect is the displacement of ionic charges within a crystal structure. Above a critical temperature, the Curie point, each perovskite crystal exhibits a simple cubic symmetry with no dipole moment (Fig 1.1-a). At temperatures below the Curie point they has tetragonal or rhombohedral symmetry and a dipole moment (Figure 1.1-b). In the absence of external strain, although the alignment gives a net dipole moment to the domain (adjoining dipoles form regions of local alignment) the charge distribution within the crystal is symmetric and the net electric dipole moment is zero (Figure 1.2-a). The domains in a piezo ceramic are

aligned by applying strong electric field, usually at a temperature slightly below the Curie point (Figure 1.2-b). Domains aligned with the field, and the element lengthens in the direction of the field. When the electric field is removed most of the dipoles keep their configuration of alignment (Figure 1.2-c). The element now has a permanent polarization, the remanent polarization, and is permanently elongated. Similar result obtained when an external stress is applied. The charges are displaced and the charge distribution is no longer symmetric. A net polarization develops and an internal electric field appears. A material can only be piezoelectric if the unit cell has no center of inversion [1-3].

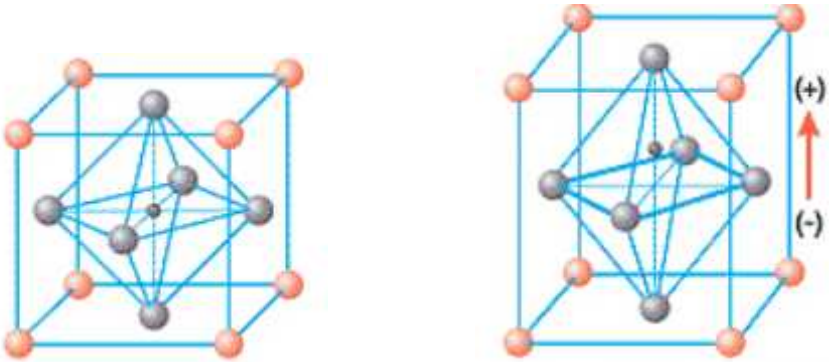

a) Temperature above Curie point b) Temperature belov Curie point

Figure 1.1. Crystal structure of perovskite piezoelectric ceramic [4]

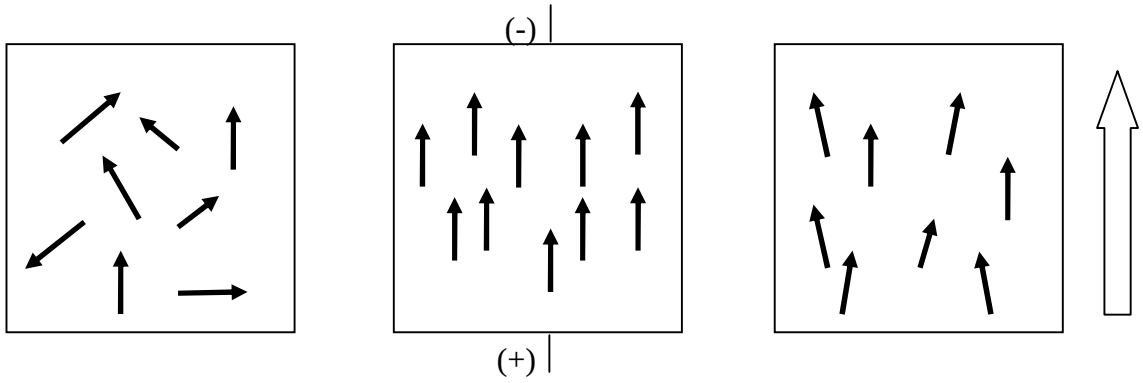

a) Before polarization b) Polarization in electric field c) Remanent polarization after electric field removed

Figure 1.2. Polarization of piezoelectric ceramic

The piezoelectric effect has many different applications areas such as production and fuel igniting devices, detection of sound, generation of high voltages, electronic

frequency generation, microbalances, and ultra fine focusing of optical assemblies. It is also used in scientific instrumental techniques with atomic resolution, such as scanning probe microscopes (STM, AFM, etc) [5,6].

In addition another application area of piezoelectric materials is energy harvesting devices. IDTechEx finds that the money spent on piezoelectric energy harvesting investments will grow to $145 million in 2018. Thereafter, it will create a $300 million market by 2022 in more complex devices such as remote controls, sensors and wireless sensor networks [7]

1.1.1. Piezoelectricity-Ferroelectricity-Crystal Systems

The smallest unit repeating in the lattice is called the unit cell. Whether piezoelectricity exist in the crystal depends on a specific symmetry exist in the unit cell. All crystalls dividen into 32 different classes in terms of symmetry groups. 21 classes out of 32 classes are non-centrosymmetric. Non-centrosymetry is the necessary condition for piezoelectricity. 20 class out of 21 class are piezoelectric. Piezoelectric effect is linear and reversible. 10 out of 20 classes are pyroelectric. Unlike piezoelectricity, pyroelectricity produce polarization spontaneously and form permanent dipoles in the structure. This polarization changes with temperature. A subgroup of pyroelectrics are known as ferroelectrics. These material possess spontaneous dipoles and these dipoles reversible under electric field. Four types of ceramic ferroelectrics based on its unitcell structure: (1) the tungsten–bronze group, (2) the oxygen octahedral group, (3) the pyrochlore group, and (4) the bismuth layer–structure group.The second group (ABO_3 perovskite type) is the most important category (Figure 1.3) [8].

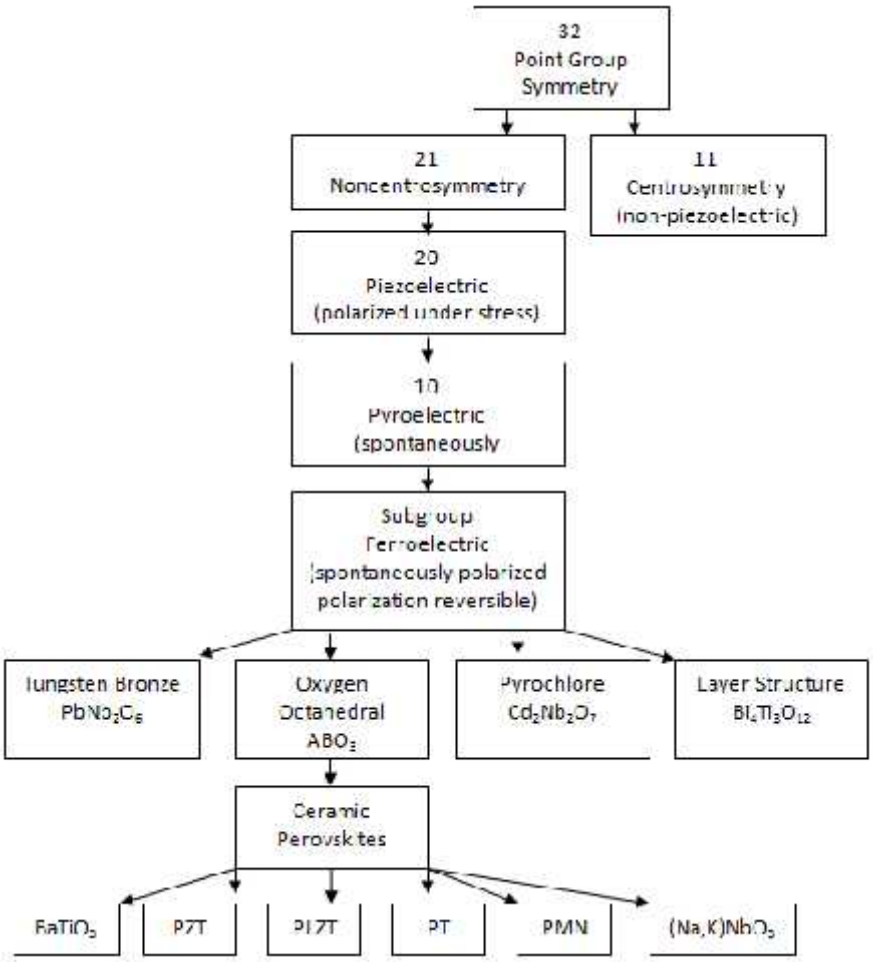

Figure 1.3. 32 symmetry groups and its subgroups [8].

1.1.2.Perovskites

Perovskites contains ABO_3 chemical composition. Large cation (A site) is placed on the corners of simple unit cell and smaller cation in the body center (B site) and oxygen in the centers of the faces. Smaller cation fills (Ti, Zr, Sn, Nb etc.) the octahedral holes and the larger cation (Pb, Ba, Sr, Ca, Na etc.) fills the dodecahedral holes. The structure is a network of corner-linked oxygen octahedra (Figure 1.4).

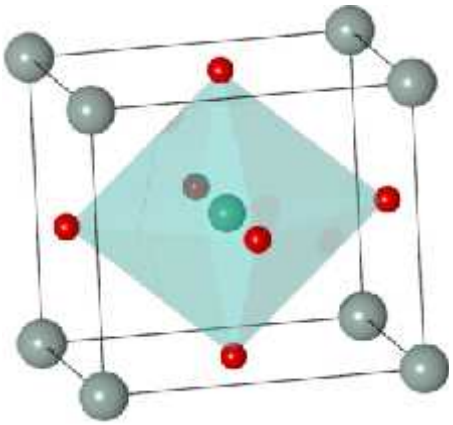

Figure 1.4. Perovskite structure (Cubic perovskite unit cell. A-site cations are gray, on the corner, B-site cations green inside the cell, oxygen red, on the faces.)

The Goldschmidt tolerance factor (t) can be used to explain the distortion of the perovskite structure from the perfect cubic perovskite structure. The Goldschmidt tolerance factor based on the geometrical packing of charge spheres and is determined from ionic radii.

$$t = \frac{(\mathrm{Ra} + \mathrm{Ro})}{\sqrt{2}(\mathrm{Rb} + \mathrm{Ro})}$$

A perovskite structure is stable only if the tolerance factor is in the range 0.9< t <1.1; larger deviations of t from unity generally prevent crystallization in ABO_3 structure [9,10].

1.2. Sintering

Sintering is defined as the heat treatment of the powder compact to obtain a highest density in a defined shape with control over microstructure such as grain size, grain shape etc. The driving force for sintering is the reduction in the surface free energy. It can be achieved by elimination of internal surface area associated with pores by transferring of material from higher chemical potential regions of lower chemical potential.

The decrease in surface free energy of a spherical particle with a radius r is given as $E_s = 3\gamma_{sv}V_m / r$, where γ_{sv} is the specific surface energy of the particle and V_m is the molar volume. As the radius of the particles decreases surface energy increases.

Sintering can be classified into two main parts as solid state sintering and liquid phase sintering. In solid state sintering densification of powder compact occurs at a temperature that is 0.5-0.9 of the melting temperature. Pore elimination is achieved by atomic diffusion in solid state. There is a competition between densification and coarsening depending on the dominant sintering mechanism. Liquid phase sintering is the consolidation technique of the powder compact in the presence of liquid less than a few volume percentage. Temperature reaches above the solidus temperature of one of the components. The purpose of liquid phase is to enhance densification rate and to obtain specific grain boundary properties. There is another sintering technique called transient liquid phase sintering. In this technique the liquid phase formed at the initial stage of sintering, consumed during the sintering process. At the end of the sintering only solid phase exist. Strong sensitivity to processing parameters were indicated for transient liquid phase sintering [11,12].

1.2.1. Sintering Mechanisms

There are six sintering mechanism in solid state sintering according to three particle model. They define the mass transport direction between source and sink. These are surface diffusion, lattice diffusion (from surface), vapor transport, grain boundary diffusion, lattice diffusion (from grain boundary) and plastic flow. Surface diffusion and vapor transport favors coarsening. These mechanisms reduce the neck surface curvature and reduce the driving force for sintering. Grain boundary diffusion and lattice diffusion favors densification. In these mechanism during neck growth occurs particle centers move toward each other. The mechanisms are summarized in Figure 1.5 and Table 1.1 [11,12].

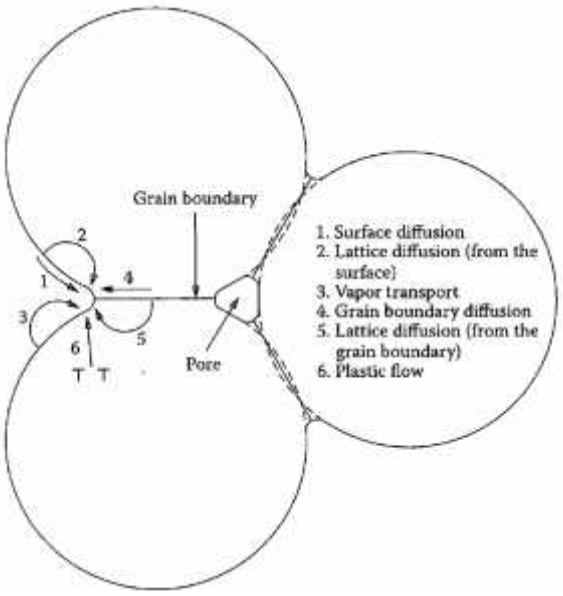

Figure 1.5. Schematic of densification mechanisms

Table 1.1: Densification mechanisms

Mechanism	**Source**	**Sink**	**Densification**
1. Surface Diffusion	Surface	Neck	No
2. Lattice Diffusion	Surface	Neck	No
3. Vapor Transport	Surface	Neck	No
4. Grain Boundary Diffusion	Grain Boundary	Neck	Yes
5. Lattice Diffusion	Grain Boundary	Neck	Yes
6. Plastic Flow	Dislocation	Neck	Yes

1.2.2. Stages of Sintering

Solid-State Sintering: Solid-state sintering has 3 steps; initial sintering, intermediate sintering and final sintering. Formation of necks occurs among particles in the initial step of sintering. In intermediate sintering stage, particle coalescence occurs and density increase is observed. Final densification occurs by removal of the isolated pores.

Liquid Phase Sintering: Liquid phase sintering (LPS) is generally applied to alloys and composites A permanent liquid phase is generated during sintering using additive.

There are three stages: rearrangement, solution precipitation and final densification. In rearrangement step, as the liquid melt it covers the solid grains. Liquid fill the pores and solid grains rearrange due to capillary action. In solution-precipitation step, atoms with high capillary pressure goes into solution and precipitates low chemical potential areas. This is called contact-flattening. Oswald ripening occurs. It is defined as the dissolution of smaller particles and precipitation on to larger particles. In final densification step, densification of solid skeletal increase the density [13].

1.2.3. Field Assisted Sintering Techniques (FAST)

The aim of these techniques is to produce fine grained high density materials by preventing the grain growth during later stages of sintering. The advantages are reduction in sintering temperatures and sintering time and prevention of grain growth.

1.2.3.1. Spark Plasma Sintering

Spark plasma sintering (SPS) is one of the well known field assisted sintering techniques. In SPS sample is placed in a graphite die. An external pressure around 300 MPa is applied while heating of the sample proceed. The main characteristic of SPS is high current (1 to 10 kA) and low voltage (below 10 V/cm) DC pulse application to graphite die for consolidation. This pulse initiate joule heating which facilitates high heating rates up to 500°C/min. Rapid densification occurs because of high pressure and high heating rate. Disadvantages are high operating costs, difficulty to control current and temperature. It is not suitable for mass production [13,15,16].
Full density KNN ceramics were obtained by spark plasma sintering (SPS). Smaller grain sizes (200-300 nm.) and lower sintering temperature (920°C) were observed [15]

1.2.3.2. Flash Sintering

Flash sintering is a two electrode method. Sintering occurs in a few seconds (less than 5 s) The abrupt nature of the sintering process in flash sintering distinguishes it from FAST sintering techniques which require high pressure and high currents. Flash sintering requires high field (100-500 V/cm) and low current (20-80 mA/mm^2). In flash

sintering electric field is applied to the sample via two electrodes while the sample is heated. The furnace temperature is controlled independently. This method has only recently been initiated at the University of Colorado. It reduces the sintering temperature compared to conventional sintering. The main characteristic of flash sintering is abrupt current increase and sudden densification (in a few seconds) that appear at the same time [17-26].

Power dissipation, I^2R, (V=I*R) increases as the resistance falls under voltage control. The non-linear increase in the current in the specimen is controlled by setting a current limit at the beginning of the experiment. When the limit value is reached power supply switches to current control. After that, power dissipation, I^2R, reaches a quasi-steady-state rate depending on the reduction of the resistance leads to a stable specimen temperature [25-26].

Flash sintering was applied to yttria [20] , yttria doped zirconia [17] , Mg doped alumina [21], Co_2MnO_4 [22] , SiC [23] , $SrTiO_3$ [24] and TiO_2 [25] up to now. It usually reduces the sintering temperature compared to conventional sintering and prevents grain growth. However for $SrTiO_3$ and TiO_2 at higher applied fields (150V/cm) grain growth was observed.

1.2.3.2.1. Effect of Electric-Field and Current Density on Flash Sintering

The flash effect can be observed by both DC and AC electric fields. Electric field and current density were sintering parameters for DC field experiment whereas electric field, current density and frequency were sintering parameters for AC field experiments. Applied electric field determines the flash sintering temperature for constant heating rate experiments. Flash sintering temperature is the temperature where abrupt shrinkage was observed. As the electric field increase flash sintering temperature decrease. Figure 1.6 shows the relation between electric field and flash sintering temperature for constant heating rate experiments for 3% yttria stbilized zirconia [26]

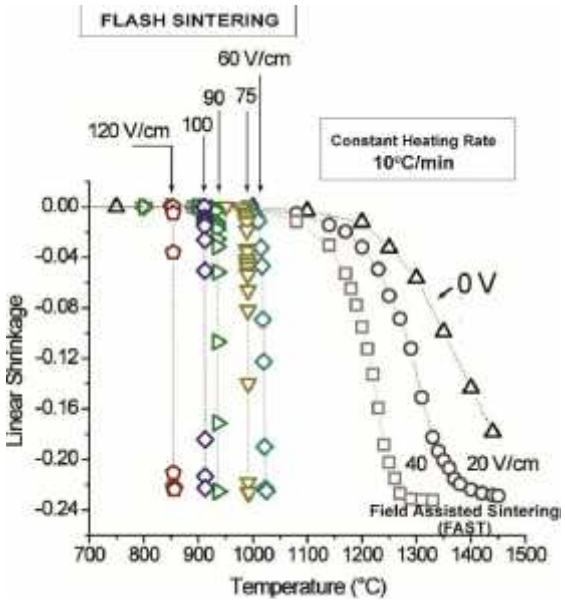

Figure 1.6. Flash sintering of 3 mole% yttria stabilized zirconia (3YSZ) [17].

Current density value determines the final density of the material. Figure 1.7 shows the current density-material density relation at constant temperature. As the current density increased density of the material increased.

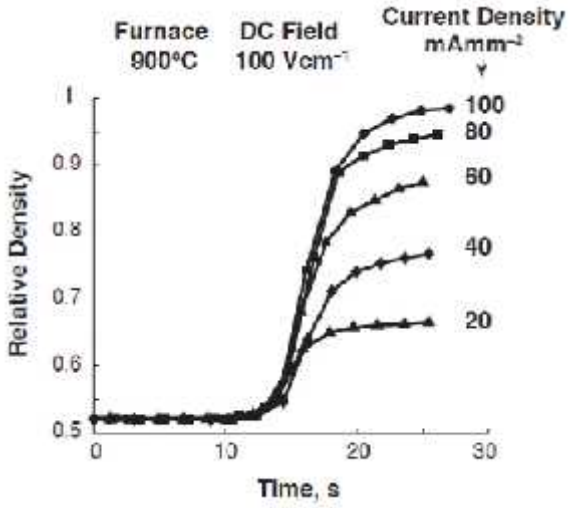

Figure 1.7. Effect of current density during isothermal (900°C) flash sintering at 100 V/cm. [26]

1.2.3.2.2. Isothermal Flash Sintering

One of the mechanisms proposed for flash sintering was defect avalanche. Nucleation of defect was proposed as one of the reasons to initiate flash. The relation between

incubation time and electric field was investigated. Electric field was accepted as a driving force for nucleation , and nucleation was accepted as a driving force for flash. It was hypothesized that an embryo of high dielectric constant was formed under the influence of the electric field and after reaching a critical size it initiate flash.

Isothermal experiments were done to determine the incubation time for sintering. The sample was heated at a constant temperature. After stabilization electric field was applied. There is a certain time needed for the initiation of the flash event depending on the magnitude of the electric field. This period was called as "incubation time". A non-linear relation was found between incubation time and applied electric field (Figure 1.8). As the temperature is lowered, a higher field is required to initiate the flash.

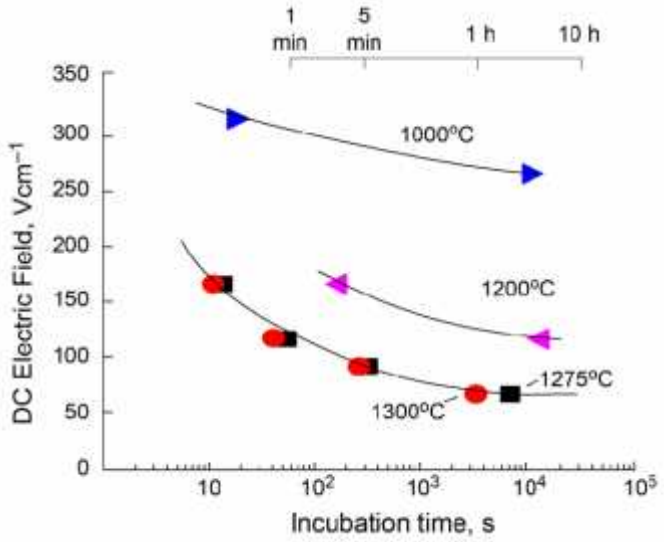

Figure 1.8. Effect of DC electric field on the onset of flash sintering at different isothermal furnace temperature (1000°C, 1200°C, 1275°C and 1300°C) in a) liner b) semi-log diagrams [26].

1.2.3.2.3. Mechanisms of Flash Sintering

There are proposed three possible mechanisms to explain flash event: 1) Joule heating, increase in specimen temperature via electrical energy, at grain boundaries. The effect of Joule heating was reported in YSZ and SiC. However, Raj et al. showed that only joule heating was not enough to achieve a fast sintering/diffusion rate assuming that sintering is grain boundary driven solid state sintering. (2) the production of Frenkel defect pairs (interstitial and vacancy) and their ionization under electrical field. The mechanism is explained as vacancy-interstitial pairs of both anions and cations can

ionize under electric field producing hole and electron. The vacancy and interstitial are now free to move within the lattice. So vacancy will migrate toward the grain boundary and interstitial towards the pore. It explains the abrupt increase in both electrical conductivity and solid-state diffusion during flash sintering. (3) Space charge layer adjacent to grain boundaries (can have strength of 10–1000Vcm^{-1}) may interact with external electric field and change the diffusion kinetics [17-19]. Positive electric charge around grain boundaries were determined for Al_2O_3 by observing grain boundary motion under bias [27] and visualized for Mn doped $SrTiO_3$ by electron holography [28].

Narayan suggested that ionic and electronic transport along dislocations and grain boundaries were increased depending on the increase in the defect segregation. As a result dislocation mobility and selective Joule heating rose creating a selective melting of grain boundaries. Therefore, higher sintering rates observed during flash sintering was claimed to be due to 6-8 orders of magnitude higher diffusivities of melted grain boundaries. These boundaries were devoid of any glassy film at the end of cooling [29].

Zhang and co-workers claimed that flash initiated as a thermal runaway for ZnO based systems. They found ~320 °C reduction on the flash sintering temperature of powder ZnO compared to single crystal ZnO (~870 for single crystal and ~550 for powder ZnO) and emphasized the importance of grain boundaries during flash [30].

1.3. Piezoelectric Materials

The most well known pizoelectric material was solid solution of $PbZrO_3$-$PbTiO_3$ (Pb(Zr1-*x*Ti*x*)O3 or PZT) and it derivatives such as Pb($Zn_{1/3}Nb_{2/3}$)O3-$PbTiO_3$ (PZN-PT) and Pb($Mg_{1/3}Nb_{2/3}$)O3-$PbTiO_3$ (PMN-PT). Most commercially used piezoelectric materials have preovskite structure. PZT is generally used at a morphotropic phase boundary (MPB) around x = 0.48 composition because of their superior dielectric, piezoelectric and electromechanical coupling coefficients.

However, the large amount of lead contained (60%) in PZT materials begin to create a big problem , due to the environmental concern and government regulations against hazardous substances. In 2006, the European Union has accepted regulations Waste Electrical and Electronic Equipment (WEEE) and Restriction of the use of certain

Hazardous Substances in electrical and electronic equipment (RoHS), to protect human health as well as environment. Similar regulations are also planned or established in North America, Japan, Korea and China Australia, New Zealand, and Thailand. The maximum allowed concentration was set to 0.1 wt% for lead, mercury, hexavalent chromium etc [2,10].

1.3.1. Lead-free Piezoelectric Materials

Lead-based piezoceramics has been kept as a market leader for more than half a century not only for their excellent properties but also their low production cost. Therefore, both economical parameters and functional properties are important in the development of lead-free piezoceramics. Relative prices for the commercially available raw materials either in the form of carbonates or oxides are provided in Figure 1.9.

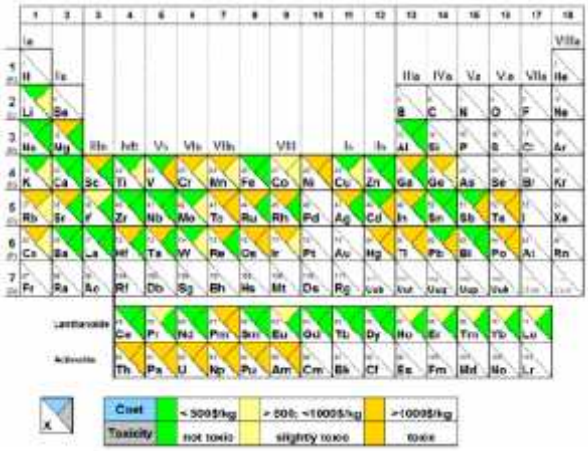

Figure 1.9. Diagram showing relative cost and toxicity of the elements of interest [10]

Therefore, significant efforts have been devoted to the development of competitive lead-free counterparts, such as $BaTiO_3$, $Bi_{1/2}Na_{1/2}TiO_3$-based perovskites, bismuth layer-structured ferroelectrics (BLSF), and (K, Na)NbO_3 (KNN)-based perovskites

$BaTiO_3$

Barium titanate has a perovskite crystallographic structure. Phase transition from tetragonal to cubic (paraelectric phase) occurs at 120°C. Low Curie temperture prevents this material used for various applications. Curie temperature can be modified by chemical substitution.

Bismuth Based Titanates

Bismuth has been related to disorders of the nervous system. The acute and chronic toxicity of bismuth is not clarified. The use of bismuth in piezoelectric materials can be considered less harmful than lead.

Bismuth titanates are suitable for high temperature applications because they have high Curie temperatures. Bismuth titanates have high Curie temperatures (Tc= 685 °C for $Bi_4Ti_3O_{12}$ and T=940 °C for Bi_3TiNbO_9). Since $Bi_4Ti_3O_{12}$ has high conductivity it is difficult to pole. They have low piezoelectric properties.

$(Bi_{0.5}Na_{0.5})TiO_3$ (BNT) has perovskite structure. It has high Curie temperature (Tc = 320°C). They require high sintering temperature (around 1200°C) and bismuth ion vaporization is observed during sintering.

$(Bi_{0.5}K_{0.5})TiO_3$ (BKT) is a tetragonal lead-free ferroelectric and it has a high Curie temperature of 370°C. It has lower piezoelectric properties compared to BNT. It is difficult to sinter and pole [14,15].

1.3.1.1. Sodium Potassium Niobates (KNN)

The piezoelectricity in KNN was discovered in 1950s. $K_{1-x}Na_xNbO_3$ abbreviated as KNN, is the most investigated lead-free ferroelectric system. In 2004, group at Toyota Central Research Laboratory reported on KNN materials modified by Li, Ta, and Sb, with piezoelectric constants comparable to those of PZT at room temperature. At higher temperatures KNN has higher piezoelectric coefficient when compared with its counterpart PZT among all lead-free ceramic materials (Figure 1.10) [10].

KNN is the solid solution between ferroelectric $KNbO_3$ and anti-ferroelectric $NaNbO_3$. Both are orthorhombic at room temperature and change their phases as the temperature increases like barium titanates. The Curie temperature of $KNbO_3$ is 434°C .$NaNbO_3$ has higher Curie temperature (480°C) than $KNbO_3$. KNN has perovskite crystal structure ABO_3 (simple cubic cell with the large cation at the corners (A site), small cation in the body center (B site), oxygen in the center of all six faces. KNN has a low density (4.51g/cm3) and high curie temperature (420°C) [10,14,15].

KNN ceramics have an orthorhombic structure with space group Amm2 at room temperature. It has an orthorhombic structure while the perovskite type ABO_3 subcell possesses monoclinic symmetry. There is no standard JAPDS-ICDD files for exact

$K_{0.5}Na_{0.5}NbO_3$ even up to now. Therefore, the structure analysis of KNN-based ceramics is not clear enough. The enhanced piezoelectric properties in the modified KNN were firstly attributed to the formation of the MPB similar to the PZT system. But later it was explained by polymorphic phase transition (PPT) [10,14,15]..

Pure KNN ceramics have the following polymorphisms, low temperature (<123°C) rhombohedral (R) phase, room temperature orthorhombic (O) phase, high temperature tetragonal (T, 200~410°C and cubic (C, >410 °C) phases [10,14].

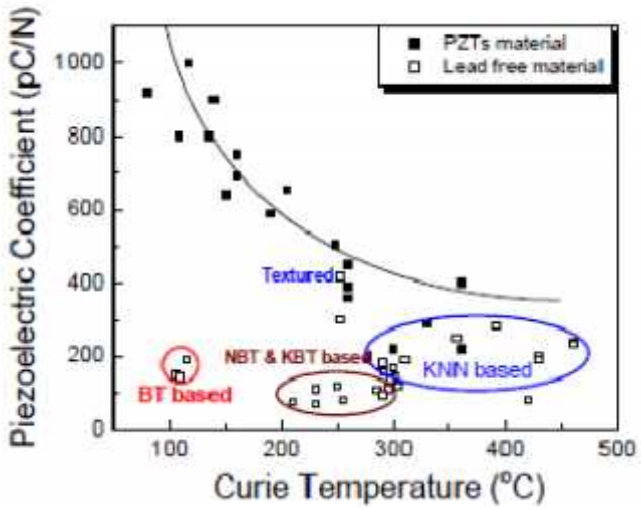

Figure 1.10. Room temperature value of d_{33} as a function of Tc for various piezoceramics [31].

The obstacles in front of KNN in replacing PZT in most applications are related to the difficulties in the synthesis and sintering of KNN. The number of successful attempts that reached above 95% density in KNN are very limited. Main problems are associated with the poor sintering ability of KNN because of narrow range of sintering temperatures, volatilization of alkali elements, and formation of secondary phases.

According to the phase diagram of $KNbO_3$-$NaNbO_3$ for the composition of x=0.5 the solidus part is about 1140°C. KNN system has a phase stability up to 1140°C which is a low temperature to reach a full density and above this temperature evaporation of alkaline is dominant. Recent studies show that evaporation is important actually after 950°C [10,14,15]..

1.3.1.2. Sintering Mechanism of KNN

Since most of the investigations were focused on the electrical properties of KNN ceramics there is still little known about the basic sintering mechanisms of stoichiometric KNN. Kang stated that grain growth in KNN was related to facetting at atomic level at grain boundaries and it can be controlled by changing sintering atmosphere. Koruza and co workers investigated sintering mechanism at the initial stage for $NaNbO_3$ by measuring the specific surface area during isothermal sintering. The surface diffusion was identified as the dominant material transport mechanism during the initial sintering stage. The activation energy for this mechanism was found in the range of 50–60 kJ/mol. The surface diffusion is one of the non-densifying mechanisms. The the poor densification of $NaNbO_3$ ceramics were related to the early activation of surface diffusion which reduce the curvature which is the driving force of densification. Due to the similarity in the lattice energies and crystal structures, the same mechanisms are suggested to be active also in, $KNbO_3$ and $(K,Na)NbO_3$ [32].

1.3.1.3. Sintering of KNN Ceramics and Electrical Properties

The difficulty in producing highly dense and phase-pure KNN with reproducible microstructure and properties were associated with powder synthesis and sintering steps. Moisture sensitive secondary phases, chemical and structural inhomogeneity, volatile components, narrow range of sintering temperature, and low solidus temperature (1140°C at x=0.5) were most widely mentioned handicaps which affected the final product [2,10,14]. Apart from these parameters, it was proposed/introduced that polymorphism of Nb_2O_5 precursor affected the sintering of KNN [33].

Various sintering variables such as time, temperature, heating rate [34] sintering atmosphere [35], sintering regime [36], A/B stoichiometry [37-38], pressure/field assisted sintering techniques [39-41] were studied with/without additives to [10,42] obtain dense product. In general, studies with KNN concentrated on using different sintering additives rather than investigating the pure KNN system. Li, Li-Ta [10,43], Cu [44], Zn, Sn, Sc, Cd [45] sintering aids were used to enhance densification by introducing a liquid phase to KNN.

Acker and co-workers [37] studied the effect of A/B excess compositions on sintering of KNN by using dilatometer. Two shrinkage rate peaks were observed for A excess

composition. The low temperature shrinkage rate peak was attributed to premelted grain boundary wetting film. They stated that if low temperature shrinkage rate peak would be related to the sintering of fine-grained powders it had to appear in the shrinkage rate curves of all (A/B and stoichiometric) KNN compositions. However, it appeared only in A excess composition.

Various groups observed two shrinkage rate peaks during sintering. It was interpreted in various ways. In general discussions related to the first shrinkage rate peak focused on two main phenomena: First one is particle size effect if the system contains nano powders; and the second one is a liquid phase formation and rearrangement if the system has liquid during sintering. Other suggestions were phase transition and change in sintering mechanism depending on the studied system.

S. Lanfredi and co-workers [46] studied sintering of $NaNbO_3$ ceramics systems and they observed two shrinkage rate peaks. They explained the first shrinkage rate peak by the initial sintering of nanopowders creating agglomerates. They related the second shrinkage rate peak by the sintering of agglomerates amoung each other. Ravi B.G. and co-workers [47] observed nanocrystalline alumina powders had more than one shrinkage rate peak compared to coarse alumina powders. They proposed different sintering mechanism of nanocrystalline powders created the first shrinkage rate peak. The dominant sintering mechanism changes from surface diffusion to grain boundary diffusion to bulk diffusion from nanopowders, to bimodal powders and to coarse powders, respectively. However, they mentioned the effect of phase transformation and broad particle size distribution could also be a reason of the first shrinkage rate peak.

There were some studies that relate the first shrinkage peak to the liquid formation. Tajika M. and co-workers [48] observed two shrinkage rate peaks on the dilatometer curve of AlN powders with Y_2O_3 sintering aid. They suggested that the low temperature peak which appeared at the same temperature of formation of Al-O-Y is caused by particle rearrangement in the presence of liquid. Wang X.X and co-workers [49] studied $LiBiO_2$+CuO added $Pb(Zr_{0.53}Ti_{0.47})O_3$ ceramics. They explained the low temperature shrinkage rate peak at 600°C as a result of a particle rearrangement since the additives had a melting temperature at 571°C. Chick et al. [50] studied the sintering behavior in a Ca-deficient $La_{0.7}Ca_{0.29}CrO_3$ and a Ca-enriched $La_{0.7}Ca_{0.31}CrO_3$ system. They proposed that two shrinkage peaks found in Ca-enriched sample was due to liquid-phase sintering caused by the melting of $CaCrO_4$. Kanka B. and co-workers [51] explained their two

shrinkage rate peaks behavior by a volume increase induced by mullitization as a result of formation of a glassy phase in the Al_2O_3+SiO_2 system

One other explanation was a volume increase because of phase transition from perovskite to garnet structure for $Nd_{3x}Y_{3-3x}Al_5O_{12}$ (Nd:YAG) system studied by Stevenson A.J and co-workers [52].

Polymorphism of Nb_2O_5 precursor was introduced as an important parameter that affects both synthesis and sintering of KNN. Hrescak J. and co-workers used different Nb_2O_5 precursors (orthorhombic and monoclinic) to synthesize KNN. They observed the surface of larger monoclinic Nb_2O_5 particles was surrounded by the reproduced nanocrystalline orthorhombic Nb_2O_5 particles after ball milling. Since the reaction in the Na_2CO_3/Nb_2O_5 diffusion couple started at 500°C, while for the K_2CO_3/Nb_2O_5 diffusion couple started at 600°C (the parabolic rate constant at 600°C for the Na_2CO_3/Nb_2O_5 diffusion couple was ten times higher than for the K_2CO_3/Nb_2O_5 diffusion couple, 1×10^{-14} m^2/s versus 3×10^{-15} m^2/s, respectively) first reaction will be between nanocrystalline Nb_2O_5 and Na_2CO_3. During later stages of synthesis of KNN this preference, shift the stoichiometry to Na rich side of $K_{1-x}Na_xNbO_3$ solid solution. The difference in the sintering behavior KNN-ortho and the KNN-mono was explained by the starting alkaline inhomogeneity of KNN-mono after calcination [33-53].

Li, Li-Ta, Cu sintering aids were used to enhance densification by introducing a liquid phase to the KNN Excess Na added, to Li modified KNN with a composition of $(1-x)(Na_{0.535}K_{0.48})NbO_3$-$x$LiNbO$_3$ with x = 0.08 sintered at 900°C and 950°C. Microstructure investigations showed that grain size increased from 1-2 μm to 20-40 μm with a density increased from 3.95 g/cm3 to 4.36 g/cm3 which was an indication of liquid phase sintering

In addition, it was found that in normal sintering of KNN ceramics, density increased within a narrow temperature range followed by a decrease if the temperature exceeded the optimal value [38].

Zuo and co-workers [45] studied the effect of adding different additives on the densification behavior of KNN. A reduction of density was observed after reaching a maximum value after certain temperature for ZnO and SnO additives. (Figure 1.13)

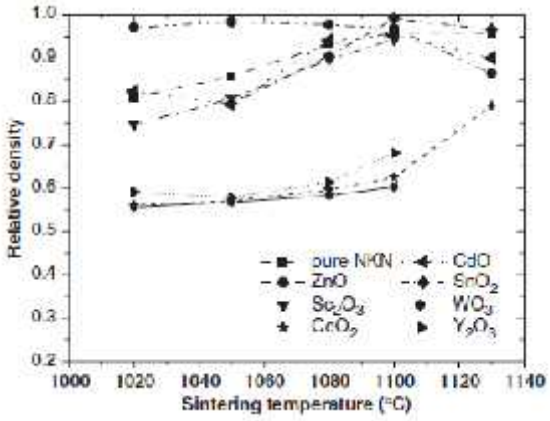

Figure 1.13. Effect of adding 1 mole % oxide additive on densification of KNN [45]

Therefore, it is important to know the chemistry and the morphology of the precursors, sintering behavior of the material and additive effects on the densification in order to have a better understanding about the KNN ceramics.

Piezoelectric properties were enhanced as the density of the material increased for pure KNN as shown in Table 1.2.

Table 1.2. Density property relation of pure and doped KNN

Additive	-	-	-	-	-	-	ZnO	SnO
Density, ρ (% of 4.51 g/cm^3)	94.2	95.3	96	96.7	98	98.4	97	98
Piezoelectric Constant, d_{33} (pC/N)	80	100	92	99	107	102	117	108
Electromechanical Coupling, kp	0.36	0.39	31	34	40	38	44	39
Reference	[54]	[55]	[45]	[45]	[45]	[45]	[45]	[45]

It was observed that addition of ZnO increased the piezoelectric coefficient more that the addition of SnO.

However, the highest piezoelectric strain coefficients were obtained at the temperatures lower than that for the highest density for KNN, Li and Li-Ta modified KNN. Figure 1.11 shows the change in the sintered densities of the KNN, Li-KNN (LKNN) and Li/Ta-KNN (LKNNT) samples as a function of sintering temperature. Addition of Ta shifted the maximum sintering point to higher temperature, whereas the densification

behavior was almost the same both for the samples without and with Li doping. The temperature where the maximum d_{33} value was obtained different from the point where the peak density was achieved.

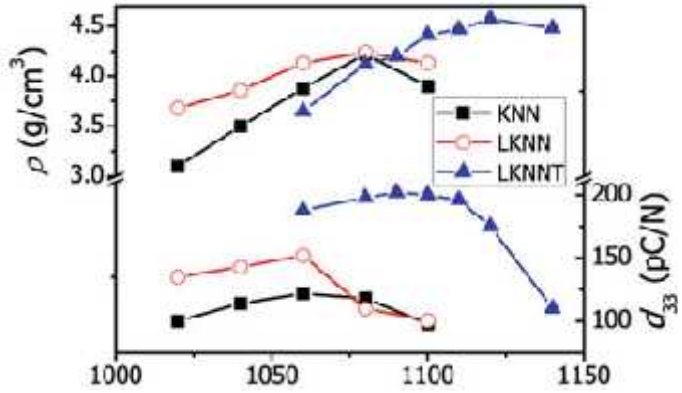

Figure 1.11. Density and piezoelectric coefficient d_{33} of KNN, LKNN and LKNNT samples as a function of sintering temperature [14]

This difference was explained by the volatilization of alkali components during the sintering The volatilization cause composition deviation. Inductively coupled plasma (ICP) analysis confirmed the volatilization was more effective after 1000°C, as shown in Figure 1.12 .

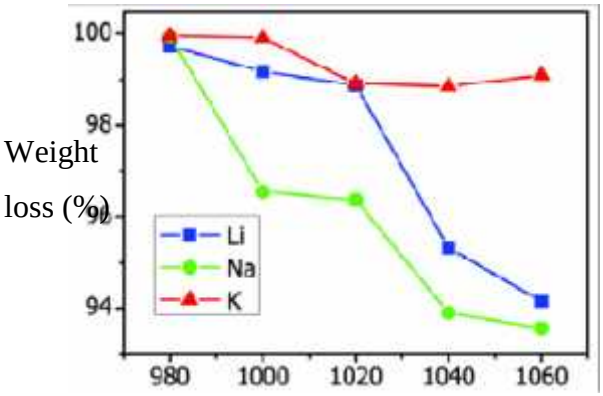

Figure 1.12. Weight loss of alkaline elements in KNN based ceramics as a function of sintering temperature [14].

In addition, higher piezoelectric coefficient (148 pC/N) was observed by SPS [15].

CHAPTER 2

2. EXPERIMENTAL STUDIES

2.1. Materials

Na_2CO_3 (Sigma-Aldrich), K_2CO_3, sodium potassium tartrate $KO_2CCH(OH)CH(OH)CO_2Na.4H_2O$ (99.5% Fluka) niobium pentoxide (Nb_2O_5.99.5% Alfa Aesar and Merck) were used.

Potassium sodium tartrate tetrahydrate is known as Rochelle salt. It is a double salt of tartaric acid (Fig.2.1).

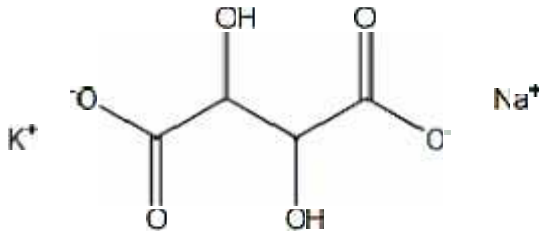

Fig.2.1. 2D configuration of sodium potassium tartrte [56].

Nb_2O_5 has different polymorphs. Pseudohexagonal (TT-Nb_2O_5), orthorhombic (T-Nb_2O_5), and monoclinic (H-Nb_2O_5) crystal phases are the most common ones. Lattice constant of the phases are : pseudohexagonal phase a= 3.60 A° , b= 3.61 A° , c= 3.92, orthorhombic phase is a= 6.19 A° , b= 3.625 A° , c= 3.94 and monoclinic is a= 21.14 A° , b= 3.82 A° , c= 19.45 A°. Amorphous Nb_2O_5 crystallizes at 500°C into TT or T phases, at 800°C transforms into M phase (tetragonal), and above 1000°C it forms the H phase. H-Nb_2O_5 is the most thermodynamically stable crystal phase while the TT- and M-Nb_2O_5 forms are mostly metastable. T-Nb_2O_5 phase is constructed with the

orthorhombic unit cell where each Nb atom is surrounded by six or seven oxygen atoms, creating distorted octahedra or pentagonal bipyramids [57].

2.2. Synthesis of KNN

KNN ceramics are generally synthesized by solid state reaction route using carbonates like K_2CO_3, Na_2CO_3, and oxide like Nb_2O_5. The chemical reaction was shown below. Synthesize temperatures are between 800-900°C. Synthesis temperature was reduced to 450 °C by using urea.

$$1/4\ Na_2CO_3 + 1/4\ K_2CO_3 + 1/2\ Nb_2O_5 \longrightarrow (Na_{0.5}K_{0.5})NbO_3 + 1/2\ CO_2$$

Hygroscopic and volatile nature of precursors prevent obtaining single phase and dense KNN. Malic reported that polymorphism of niobium oxide powder has affected the purity of the powder and consequent densification behavior [33].
KNN powders were synthesized by using solution methods like sol-gel, molten salt and hydrothermal synthesize.

2.3. Sintering of Sodium Potassium Niobate (KNN)

Conventional sintering experiments were conducted by Protherm furnace at 1100°C for 2 hours. Dilatometer was used to identify the onset of sintering and to investigate the shrinkage rate behavior.
Flash sintering experiment were conducted with the furnace shown in Figure 2.1. Constant heating rate experiments were done by applying electric-field while the furnace was heating. Isothermal experiment were done by keeping the furnace at constant temperature and after the stabilization electric-field was applied.

Figure 2.1:Flash Sintering Furnace

2.4. Characterization Methods

In this study, various characterization methods were used in order to get structural and chemical information from the material both micro and nano level. The techniques used listed below:

X-Ray diffraction (XRD) was used to identify the crystal structure and phases of the powders and sintered material.

SEM was used for identification of microstructure, grain sizes of powders and sintered KNN, chemical investigation.

TG-DTA was used to analyze precursors in order to get information about decomposition of raw materials.

Dilatometer was used to find out the sintering temperature and investigate the shrinkage rate behavior.

Focused Ion Beam (FIB) to prepare ultra-thin and uniform lamellas for further TEM analyses.

Transmission Electron Microscopy (TEM) was used to obtain detailed information from the materials at nanometer scale resolution. Crystal structure, grain boundaries and chemical composition were analyzed.

2.5. Experimental Techniques

2.5.1. X-Ray Diffraction (XRD)

X-rays are electromagnetic radiation They have shorter wavelength than light. x-rays used in diffraction have wavelengths approximately in the range 0.5-2.5A, whereas the wavelength of visible light is of the order of 6000A.

X-ray diffraction (XRD) is a commonly used technique for obtaining qualitative and quantitative data on atomic scale structure from crystalline and non-crystalline (amorphous) materials. It is non-destructive and can be applied to metals and alloys, minerals, inorganic compounds, thin-film coatings, ceramics, polymers and organic materials. X-ray Powder diffraction is used for crystalline phase identification and crystal structure refinement. In addition to these, crystallite size identification, lattice strain, chemical composition, and crystal orientation can be analyzed by XRD.

When X-ray beam interacts with repeating planes of atoms that form a crystal lattice part of the beam is transmitted, part is absorbed by the sample, part is refracted and scattered, and part is diffracted. Bragg's Law, $n\lambda=2d\sin\theta$, can used to measure the distances between the planes of the atoms for the diffracted beam. n is the order of the diffracted beam, λ is the wavelength of the incident X-ray beam, d is the distance between adjacent planes of atoms (the d-spacings), and θ is the angle of incidence of the X-ray beam.

The phase identification of the samples was evaluated by X-ray powder diffraction (XRD, Bruker, D8 Advance, Cu-Kα radiation; λ = 0.15064 nm) at room temperature. The XRD was operated at 40 kV and 40 mA. scans at rate of 1^o/min with step 0.02^o between 20-80^o [58].

2.5.2. Scanning Transmission Electron Microscopy (SEM)

The resolving power of human eye is 0.2 mm. It can be enhanced by using lenses (microscope) which magnify this distance. But wavelength of the light used for illumination is the limiting factor for light microscopes. Therefore, electrons were used with shorter wavelengths and better resolution.

Electrons produced at the top of the column, accelerated down. It passes through condenser lenses, condenser aperture, objective aperture and objective lens in order to produce focused beam. The position of the electron beam on the sample is controlled by scan coils situated above the objective lens. SEM scans a focused electron beam over a surface to create an image. The electrons in the beam interact with the sample, producing Auger electrons, secondary electrons, backscattered electrons and cathodoluminescence. These signals are detected by detectors and give information about the surface topography and composition [59].

Secondary electrons were used for morphological investigations. Density of sintered pellet was analyzed from SEM micrographs of the polished samples by UTHSCSA Image Tool Program (developed in the Department of Dental Diagnostic Science at The University of Texas Health Science Center, San Antonio, Texas).

Energy dispersive X-ray spectrometry was used for chemical-elemental analyses. Elemental mapping of the specified regions on the samples were acquired by using EDX. For the microstructure observation, such as the morphology and grain sizes, scanning electron microscopy (FEG-SEM Leo Supra 35, Oberkochen, Germany) was employed. Chemica analysis were done by SEM JEOL 6010 LV equipped by EDX detector.

2.5.3. Dilatometer

A dilatometer is a thermo-mechanical analytical tool used for obtaining highly precise measurements of volume changes in solids, powders. The definition of dilatometer is given as "Dilatometry (DIL) is the method of choice for highly precise measurement of dimension changes to solids, melts, powders and pastes at a programmed temperature change and with negligible sample strain (e.g. ASTM E831, ASTM D696). It is a useful technique for studying martensitic transformation in the quenching of steels, the

shrinkage from a green ceramic body during binder burnout and sintering, glass transition temperature, devitrification of glasses and solid state transformation such as α to β transition. There are different type of dilatometers. Capacitance dilatometers, push rod dilatometers, laser dilatometers and optical dilatometers [60].
Netzsch Horizontal Push Rod Dilatometer (DIL 402 PC push rod, Netzsch, Germany) was used for the experiments.

2.5.4. Thermogravimetric Analyzer (TG-DTA)

Definition of Thermal Analysis is given as "A group of techniques in which a physical property of a substance is measured as a function of temperature while the substance is subjected to a controlled temperature program." (ICTA, ASTM 473-85). Thermogravimetry (TG) quantitatively measures the weight changes in a material as a function of temperature under a controlled atmosphere. The technique is useful for transformations invlving the absorption or evolution of gasses from the specimen.
In Differential Thermal Analysis (DTA) analysis, the device measures the the difference in temperature between a sample and reference which are exposed to the same heating schedule. The reference material does not go any transformation in the temprature range of interest. The temperature difference between sample and the reference is measured by differential thermocouple in which one junction is connected to sample crucible and other one is connected with the reference crucible. The sample temperature is measured as a voltage difference between these two junctions. DTA curve provides data on glass transitions, crystallization, melting and sublimation. Endothermic or exothermic reactions can be detected. The area under a DTA peak corresponds to the enthalpy change [60]. Thermal properties of the samples were studied using differential thermal analysis (Netzsch STA 449C Jupiter, Germany).

2.5.5. Transmission Electron Microscope (TEM)

In transmission electron microscope (TEM), less than 200 nm thin sample is bombarded by energetic beam (generally 200 kV) of single-energy electrons. High energy-thin sample conditions let the electrons transmit through the sample. Interaction of high energy beam of electrons with the specimen produced many signals shown in Figure 2.2. The signals magnified by electromagnetic lenses before observing on the

phosphorous screen. There are different TEM techniques that give information about the material.

Electron diffraction is used to determine the crystallographic structure of the material. Amplitude-contrast imaging such as diffraction contrast, gives information about the chemistry and microstructure and defects. Phase-contrast imaging such as high resolution TEM gives information about the microstructure of a material and its defects at an atomic resolution [59].

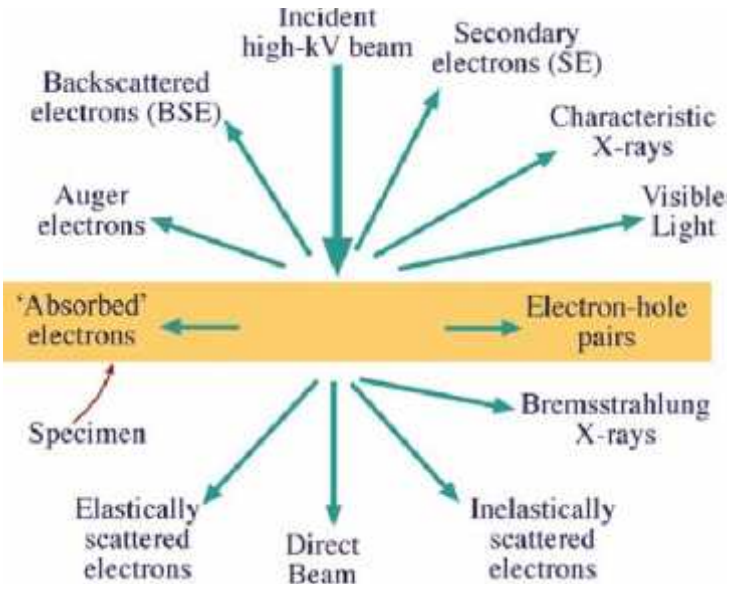

Figure 2.2. Signals generated when a high-energy beam of electrons interacts with a thin specimen [61].

2.5.6. Techniques used for TEM Analysis

2.5.6.1. Amplitude-contrast Imaging

Amplitude-contrast images are formed by inserting an objective aperture into the back focal plane of the objective lens. Bright-field images are formed if only the directly transmitted electron beam is selected by objective aperture. Dark-field images are formed if scattered electron beam is selected by objective aperture.

2.5.6.2. Phase-contrast Imaging

Phase contrast occurs when more than one electron beam contributes to the image. The phase difference between transmitted and scattered beams creates fringes. Moiré

patterns, Fresnel contrast at defects, and high-resolution TEM (HRTEM) imaging can be obtained by phase contrast imaging. This techniques is sensitive to sample thickness, orientation, astigmatism and focus of the objective lens. In HRTEM imaging, the lattice fringes are not direct images of the atomic structure but can give information on the lattice spacing and atomic structure of the crystal. Individual atomic columns can be separately resolved in many crystalline inorganic materials. During recording of the experimental image phase information is lost. Therefore computer simulation is necessary for the correct interpretation of HRTEM images.

2.5.6.3. Electron Diffraction

Diffraction patterns can be obtained when the back focal plane of the objective lens is set as the object plane for the intermediate lens. The selected area diffraction aperture is used to select a specific region in the sample. This technique is used to determine whether a specimen is single crystal, polycrystalline, or amorphous. It allows to identify the crystallographic structure, symmetry, lattice constants, and orientation of samples. Diffraction patterns from small areas can be obtained by converging the beam producing a convergent beam diffraction pattern, but this destroys any coherence and broadens the diffraction spots into discs. It can be used to measure specimen thickness and lattice parameters, and to determine point group and space group information.

2.5.7. Scanning Transmission Electron Microscopy (Atomic resolution Z-contrast imaging)

In the scanning transmission electron microscopy (STEM) mode, a focused convergent electron beam is created by adjusting the microscope lenses. This focused probe is then scanned across the sample and various signals are collected. The convergence of the beam destroys its coherency. Z-contrast images are incoherent, have double the resolution of coherent images, and do not reverse contrast with focus or specimen thickness. The images represent a direct map of the scattering power at atomic resolution. Because the image is formed from high-angle scattering from the atomic nuclei, the scattering cross section depends on atomic number (Z) squared [61].

High special resolution compositional maps and line profiles may be obtained in the STEM mode by collecting the (EDS) energy dispersive X-ray spectroscopy and (EELS)

energy loss. TEM sample was prepared by Focused Ion Beam (FIB) and was examined in a JEOL ARM200 ColdFEG, high resolution, scanning transmission electron microscope (HRSTEM). Chemical composition was investigated by analytical electron microscopy utilizing a STEM equipped with an EDS spectrometer (JEOL Centurion EDX spectrometer).

CHAPTER 3

3. SINTERING ANALYSIS OF ALKALINE OR NIOBIUM EXCESS SODIUM POTASSIUM NIOBATE BY DILATOMETER

3.1. Abstract

Stoichiometric ($K_{0.5}Na_{0.5}NbO_3$), A-site excess (alkaline) and B-site excess (niobium oxide) KNN powders were synthesized by using different precursors, i.e. System 1) Na and K carbonates and (monoclinic+orthorhombic) Nb_2O_5 powder and System-2) Na-K tartrate and (orthorhombic) Nb_2O_5 powders. Sintering behavior was investigated by dilatometry. Double shrinkage rate peaks were observed for A-site excess composition whereas single shrinkage rate peak was observed for stoichiometric and B-site excess compositions. The low temperature shrinkage rate peaks for A-site excess composition was caused by the Na_2CO_3-K_2CO_3 eutectic-melting. The intensity of low temperature shrinkage rate peak was correlated with the A-site excess amount. The liquid film that appeared at low temperature helps the rearrangement of the grains during early sintering.

3.2. Experimental Studies

A-excess (mole%), stoichiometric $K_{0.5}Na_{0.5}NbO_3$ and B-excess (mole%) KNN compositions were synthesized using Na_2CO_3 and K_2CO_3, and niobium pentaoxide

(Nb_2O_5.99.5% Alfa Aesar) were used. Before mixing raw materials was fired in the furnace at 250°C for 6 hrs .in order to remove any moisture. The powder mixture was ball milled for 24 hours with isoprophanol for homogenization. After drying, KNN powder was synthesized in an alumina crucible at 800 °C.

Sodium potassium tartrate tetrahydrate known as Rochelle salt $KO_2CCH(OH)CH(OH)CO_2Na.4H_2O$, (99.5% Fluka) and Nb_2O_5 (+99%, Merck) was used to synthesize KNN powders. Before mixing carbonates were fired in the furnace at 250°C for 3 hrs .in order to remove any moisture. The powder mixture was ball milled for 24 hours with isopropanol for homogenization. After drying, KNN powder was synthesized in an alumina crucible at different temperature among 600-800 °C to find out the optimum temperature.

Synthesized KNN powders were ball milled and dried. They were compacted into disks with 12.5 mm diameter and cold isostatical pressed up to 200 MPa , respectively.

Synthesized powders were characterized by using X-Ray diffraction (XRD, Bruker D8 Advanced), equipped with Cu Kα radiation

Dilatometer measurements (Netzsch DIL 402 PC) were done to investigate the sintering behavior of the samples from the shrinkage and shrinkage rate curves.

The microstructures of synthesized and sintered samples were investigated by Scanning Electron Microscopy (JEOL 6010 LV) and (Zeiss Leo Supra)) equipped with EDX apparatus.

3.3. Results

3.3.1. Precursors

XRD analysis of Nb_2O_5 precursor showed that the Alfa Aesar- Nb_2O_5 powder contains orthorhombic + monoclinic phases whereas Merck- Nb_2O_5 powder has only orthorhombic phase. (Fig.3.1, a) and c)) Fig.3.1. b) and d) shows the morphology of Nb_2O_5 powders. Single phase Merck- Nb_2O_5 powder composed of homogenous small grains with a particle size around 100 nm. Alfa Aesar- Nb_2O_5 powder contains bigger facetted grains in addition to smaller homogenous grains.

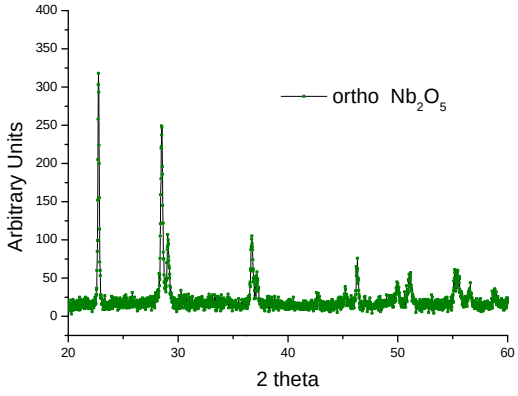

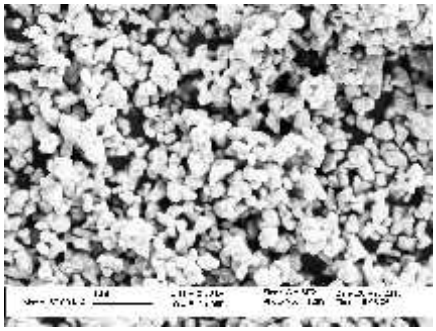

a) XRD analysis of Nb_2O_5 powder (orthorhombic)

b) SEM micrograph of Nb_2O_5 powder (orthorhombic)

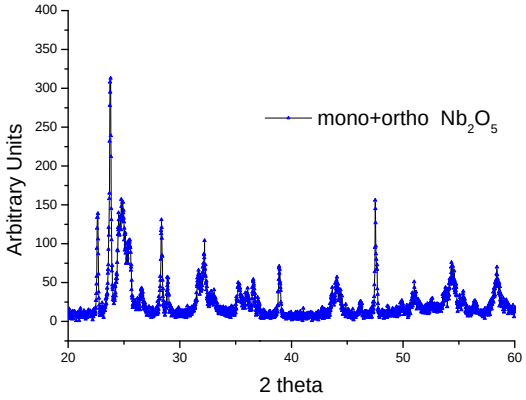

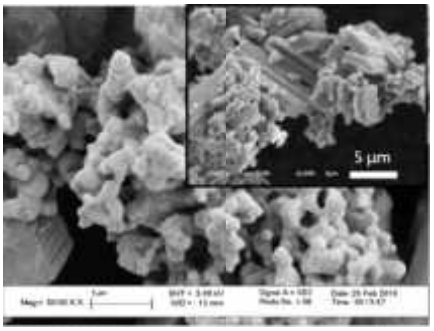

Fig.3.1. c) XRD analysis of Nb_2O_5 powder (orthorhombic+ monoclinic)

d) SEM micrograph Nb_2O_5 powder (orthorhombic+ monoclinic)

Thermogravimetric analysis were done with Na_2CO_3-K_2CO_3 mixture. Mass loss at 100°C indicates the decomposition of water in TG plot. An endothermic peak at 710°C in DTA plot indicates the melting of Na_2CO_3-K_2CO_3 system around 710°C (Fig.3.2-a).

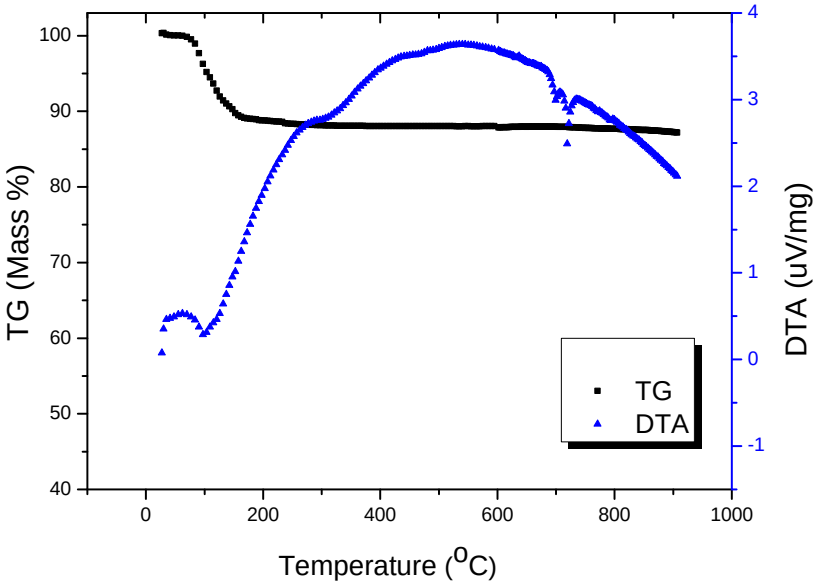

a)

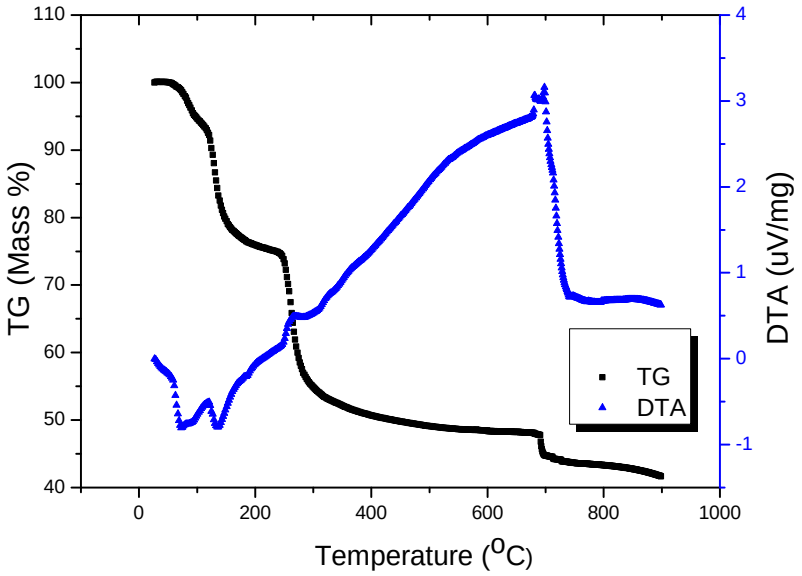

b)

Fig.3.2. Thermogravimetric analysis of a) Na_2CO_3-K_2CO_3, b) Na-K tartrate (Endo=Down position)

The decomposition of tartrate was analyzed by thermogravimetric analysis. Two endothermic peaks appear at 75°C and 138°C in DTA. Dehydration and melting occurred simultaneously. Weight loss around 250°C was attributed to decomposition of

tartrate to oxalate [62]. Decomposition of oxalates appeared at around 700°C (Fig.3.2-b). Decomposition and melting occurred simultaneously.

3.3.2. Synthesis of KNN of by Carbonate Precursors

Thermogravimetric analysis showed that mass loss finished at 700°C (Fig.3.3). This indicates absence of decomposition after that temperature. Therefore, KNN powders were synthesized at 800°C.

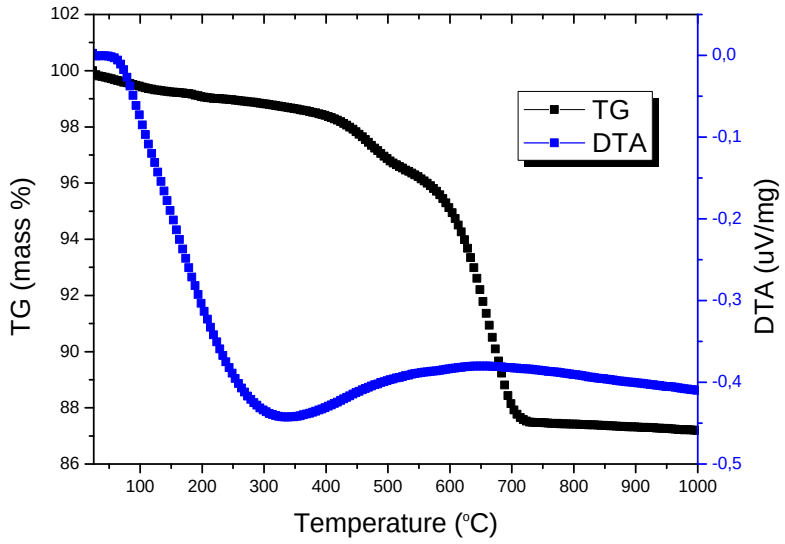

Fig.3.3. Thermogravimetric analysis of powder mixtures, a) Na_2CO_3-K_2CO_3-Nb_2O_5

Different amounts of alkaline and niobium excess KNN compositions were prepared with Na_2CO_3, K_2CO_3 and Nb_2O_5. XRD analysis showed Na rich $K_{1-x}Na_xNbO_3$ solid solution appeared for B excess composition (Fig.3.4). JCP2.2CA number 01-077-0033 was used for indexing KNN XRD peaks. Larger grains were obtained with A excess composition compared to stoichiometric and B excess composition (Fig.3.5).

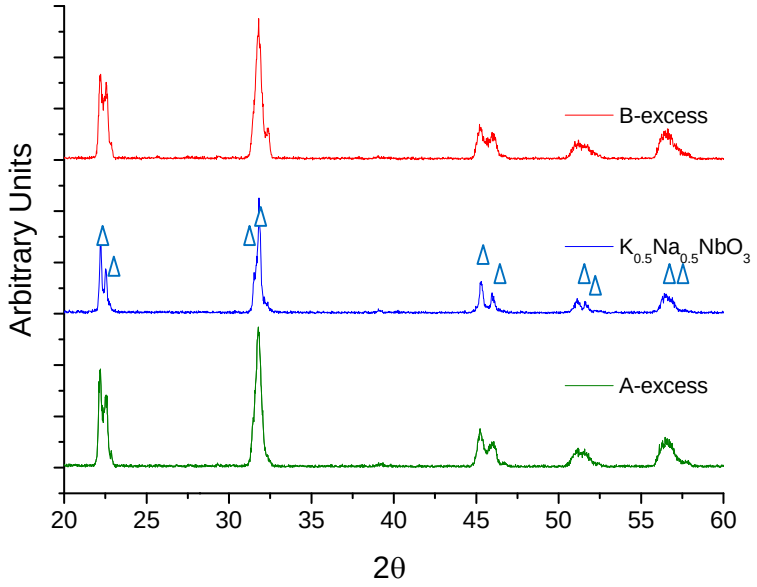

Fig.3.4. XRD analysis of A/B excess KNN powders prepared from carbonates.

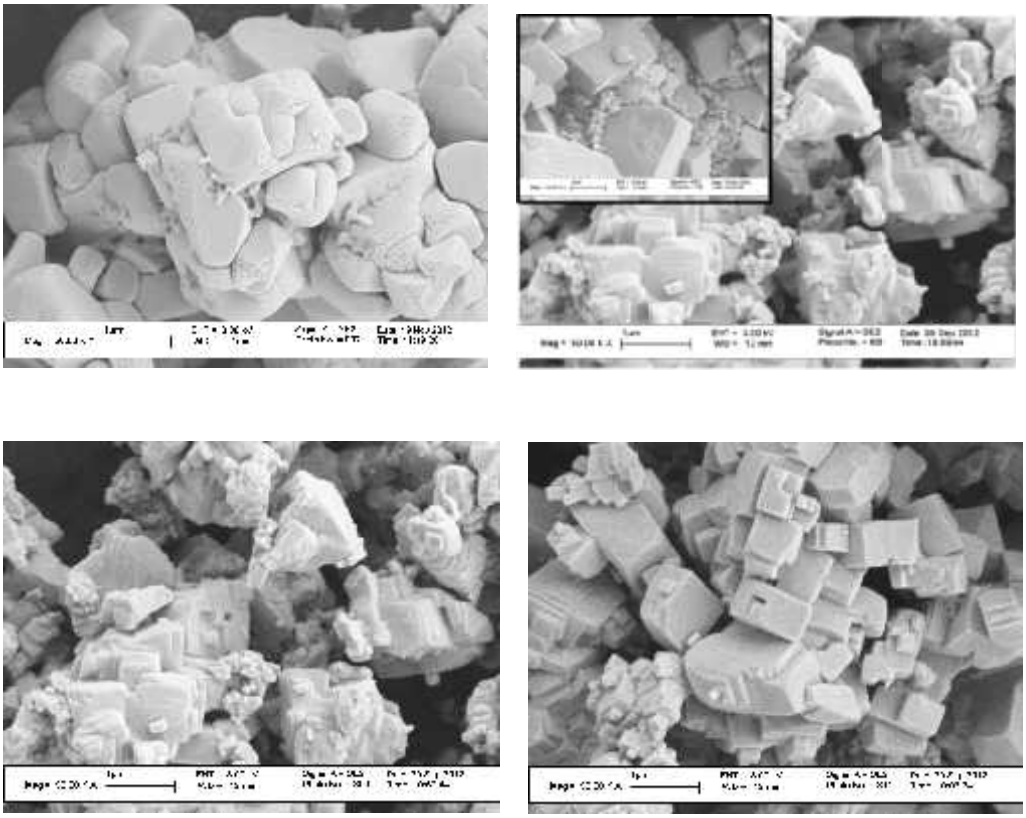

Fig.3.5. SEM micrograps of excess KNN powders prepared with carbonates source a) 3% A-excess, b) 2% A-excess, c) Stoichiometric, d) 2% B-excess

3.3.3. Sintering Analysis of KNN Powder Produced by Carbonate Precursors

Dilatometer analysis were done with different amounts of alkaline or niobium excess compositions prepared with Na and K carbonate precursors. Shrinkage began at about 750°C for 3% and 2% A excess composition whereas it began at about 1000°C for 2% B excess composition and 950°C for stoichiometric composition. 2% B excess composition and stoichiometric composition showed one shrinkage rate peak at 1060°C and 1040°C, respectively. 2% A excess composition showed two shrinkage rate peaks at 800°C and 1050°C. 3% A excess composition has one broad and deep shrinkage rate peak between 800°C and 950 °C. (Fig. 3.6).

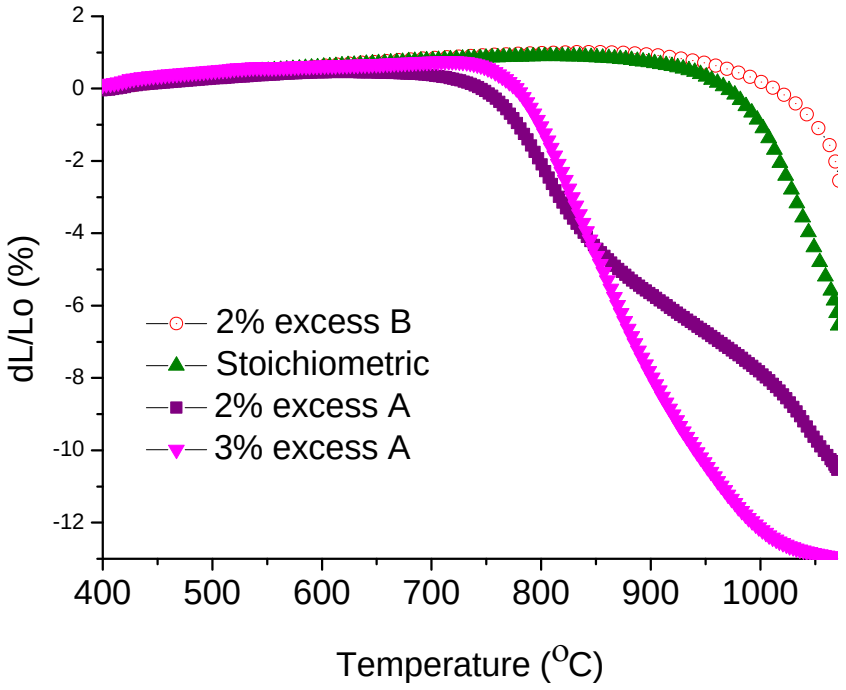

a)

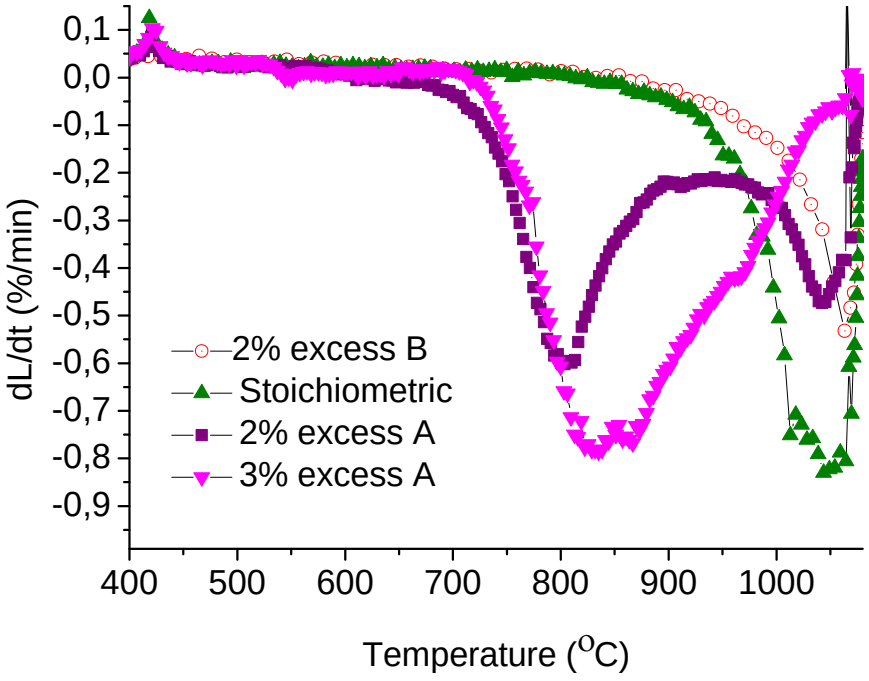

b)

Fig. 3.6. Dilatometer analysis a) Shrinkage curves, b) Shrinkage rate curves of alkaline or niobium excess KNN prepared with carbonates precursors.

XRD analysis of sintered KNN samples showed single phase KNN as shown in Fig.3.7.

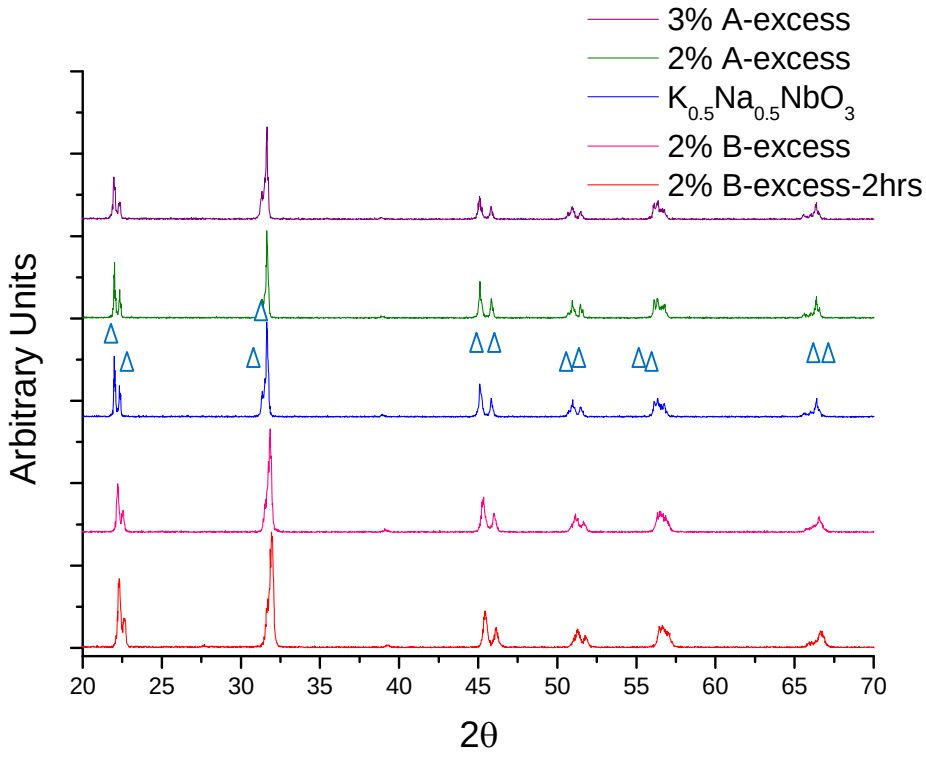

Fig.3.7. XRD analysis of sintered A/B excess KNN samples prepared from carbonates.

3.3.4. Microstructure Investigation of Sintered KNN Samples Produced by Carbonate Precursors

SEM micrographs of sintered A or B excess compositions prepared with Na and K carbonates source were shown in Fig.3.8. Smallest gain size were obtained for B excess composition. Grain sizes were increase with increasing A excess amount. 3% A-excess composition showed secondary phase.

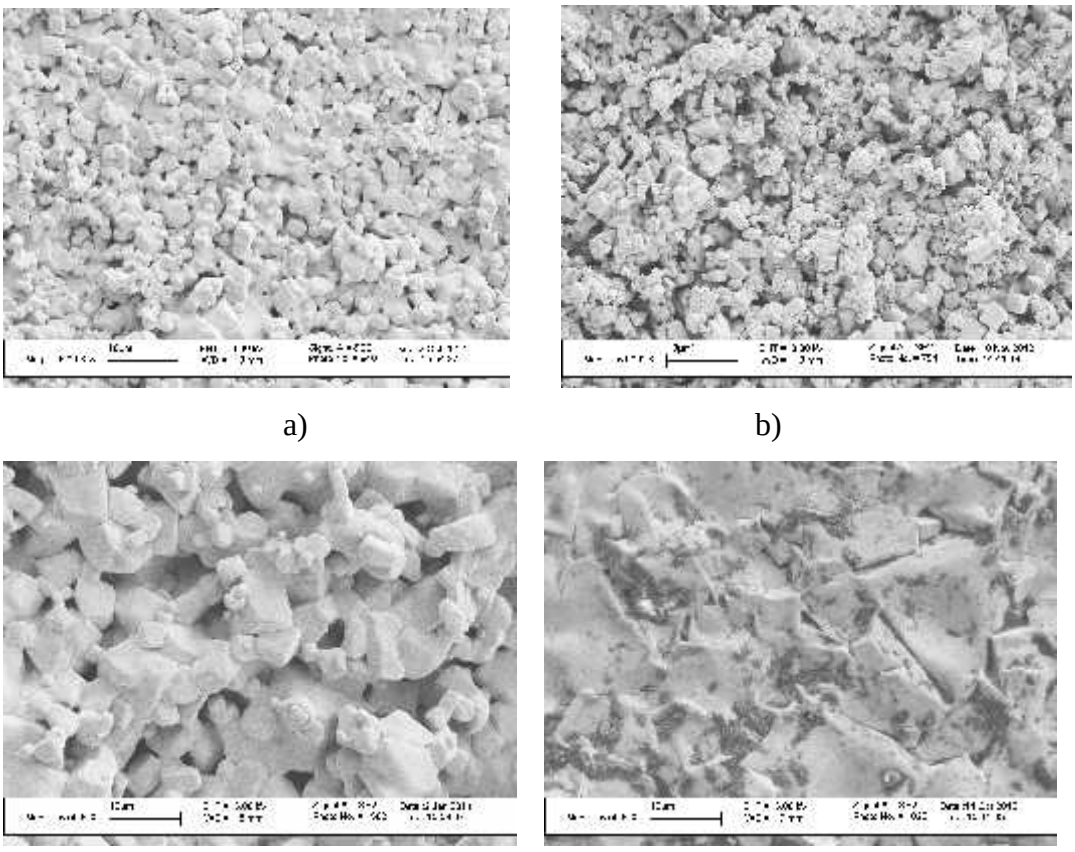

a) b)

c) d)

Fig.3.8. SEM micrographs of sintered A or B excess KNN samples prepared with Na and K carbonates source, a) stoichiometric, b) 2% B-excess , c) 2% A-excess, d) 3% A-excess

3.3.5. Synthesis of A or B Excess KNN by Tartrate Precursor

Thermogravimetric analysis and XRD analysis were done to find out the optimum synthesis conditions (for single phase KNN) with different precursors. TG analysis showed that mass loss finished at 700°C for Na-K tartrate + Nb_2O_5 system (Fig.3.9). This indicates absence of decomposition after that temperature.

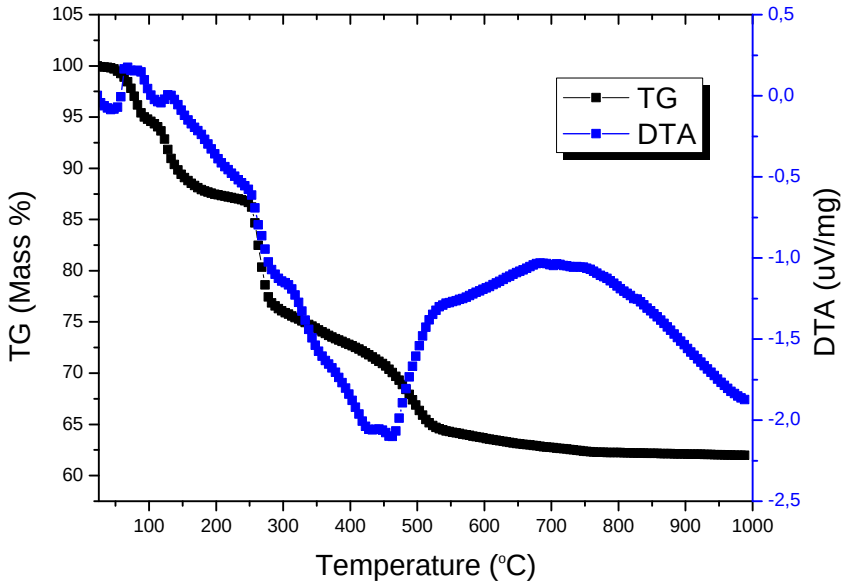

Fig.3.9. Thermogravimetric analysis of Na-K tartrate+ Nb_2O_5 mixture

XRD analysis were done with KNN powders prepared with tartrate source and synthesized at different temperatures. Fig.3.10 showed there were some unreacted phases up to 800°C. Single phase KNN was obtained at 800°C for 2 hrs (Fig.3.10) Both thermogravimetric and XRD analysis showed that 800°C is a suitable temperature to synthesize single phase KNN

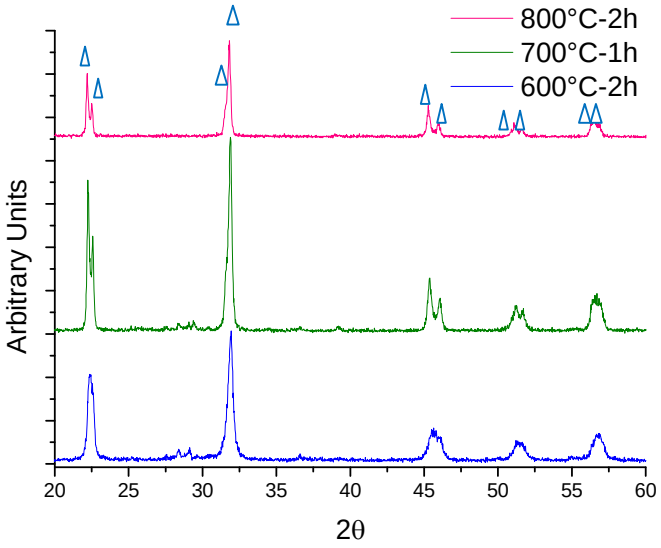

Fig.3.10. XRD analysis of synthesized powders with Na-K tartrate source.

Different amounts of A or B excess KNN compositions were prepared with Na-K tartrate source. Single phase KNNs were detected by XRD analysis of the excess compositions (Fig.3.11). SEM micrographs shows that as the A-excess amount increase, grain sizes were increased. Largest grain size were observed for 2% A-excess composition whereas smallest grain size were observed for 1% B-excess composition (Fig.3.12)

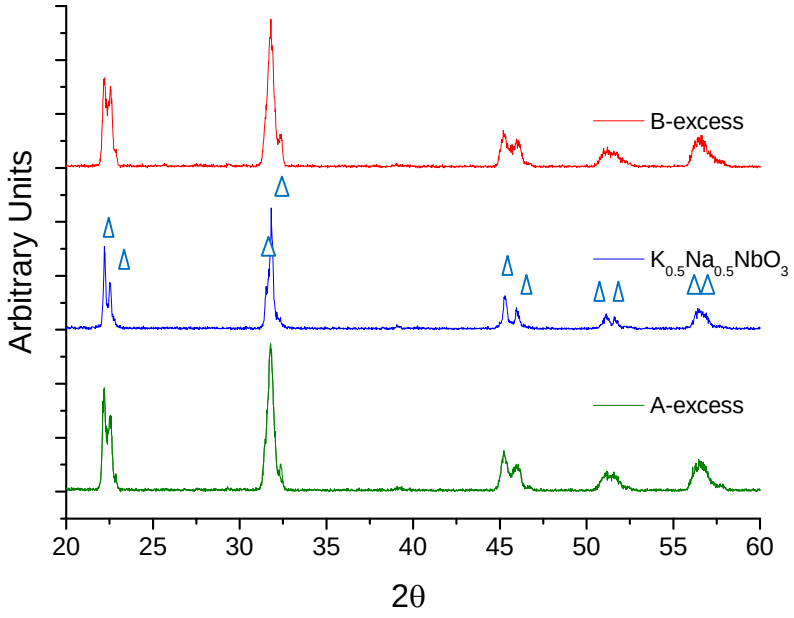

Fig.3.11. XRD analysis of A/B excess KNN powders prepared with Na-K tartrate source.

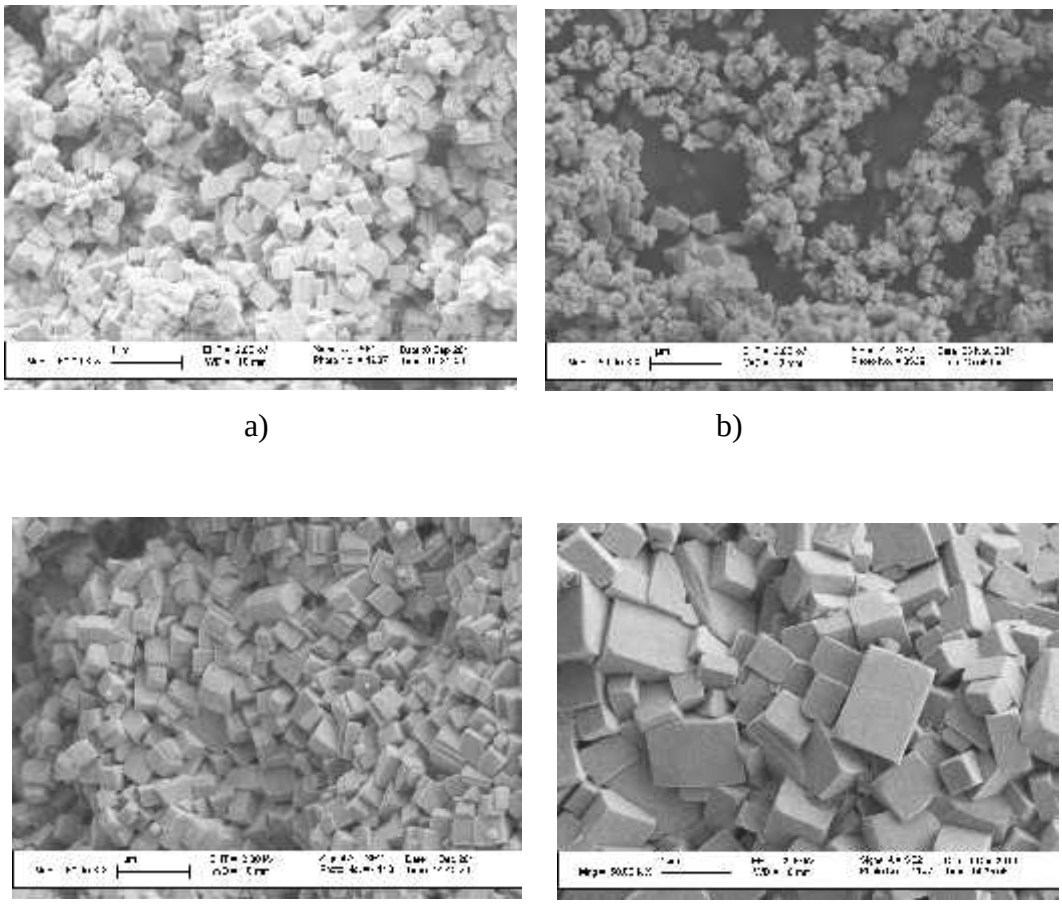

a) b)

c) d)

Fig.3.12. SEM micrographs of excess KNN powders prepared with Na-K tartrate source a) Stoichiometric,, b) 1% B-excess c) 1% A-excess, d)2% A-excess.

3.3.6. Sintering Analysis of KNN Powders Produced by Tartrate Precursor

3.3.6.1. Water-Washed of KNN powder

Sintering behavior of KNN powders prepared with Na-K tartate source was investigated with dilatometer. Fig.3.13 shows the results of dilatometer analysis of KNN. Stoichiometric KNN began to sinter at 845°C as shown with an arrow in linear shrinkage curve in Fig.3.13-a) and shrinkage continued as the temperature increased (Fig.3.13-b) shows the shrinkage rate curves. The minima in the shrinkage rate curves resembles the highest shrinkage rate at the corresponding temperature. Two shrinkage rate (minima) peaks were observed. Low temperature peak appeared at about 900°C and high temperature peak appeared at about 1095°C. Latter one was deeper.

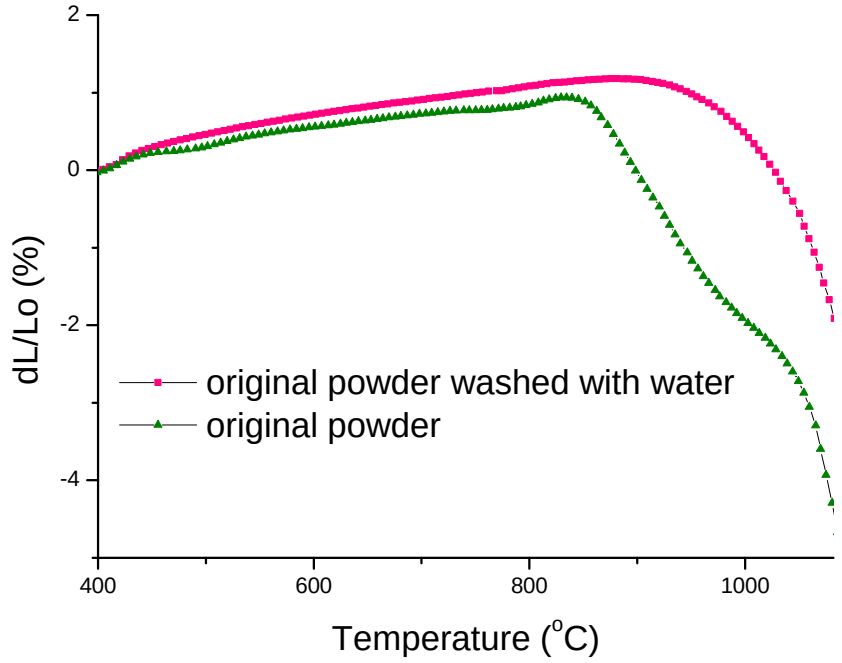

a)

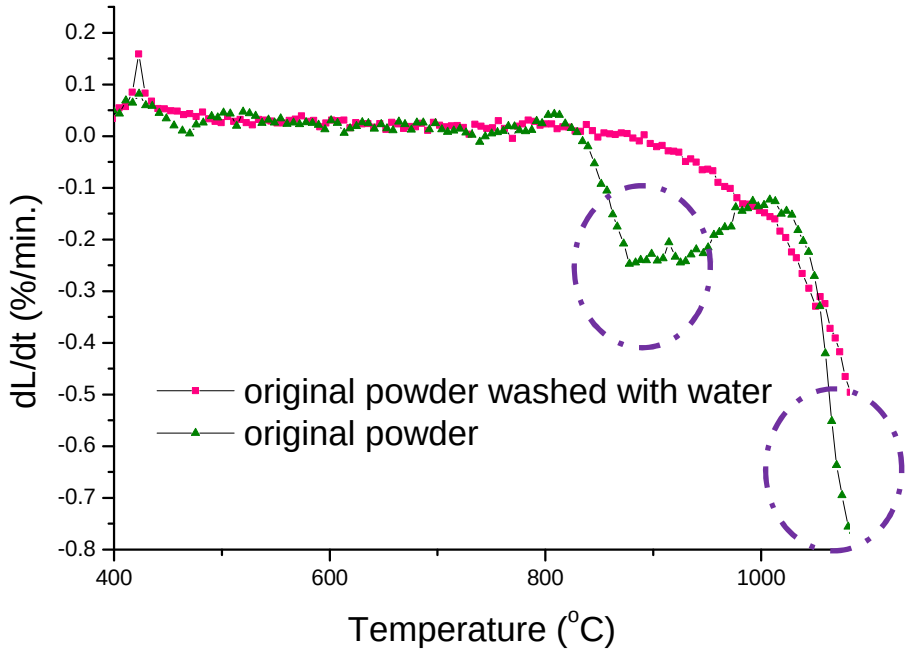

b)

Fig.3.13. Dilatometer analysis a) Shrinkage curves, b) Shrinkage rate curves

KNN powder was washed with water and dried. Dilatometer analysis was done with washed powder. The comparison of the shrinkage and shrinkage rate curves of 1)

washed-dried powder and 2) powder before washing as its original state was shown in Fig.3.13. Low temperature shrinkage rate peak was disappeared whereas high temperature peak kept stable when the powder was washed. The low temperature shrinkage peak may be related with water soluble K and Na alkaline phase in the composition. XRD analysis of the washed powder shows trace amount of NbO.

3.3.6.2. Effect of Alkaline and Niobium Excess

Dilatometer analyses were done with different amounts of A or B excess compositions prepared with Na-K tartrate method. Linear shrinkage curves in Fig.3.14 shows shrinkage begins at about 700°C for 3% A excess composition, 750 °C for 2 % A excess composition, 790°C for 1% A excess composition and 950°C for 1% B excess composition. There was no low temperature shrinkage rate peak for B excess composition. 1% and 2% A-excess compositions showed two shrinkage rate peaks. First and second shrinkage rate peak temperatures were 822°C and 1043°C for 1% A excess. 2% A excess composition has two shrinkage rates peaks at 768°C and 854°C. 3% A excess composition has one broad peak.

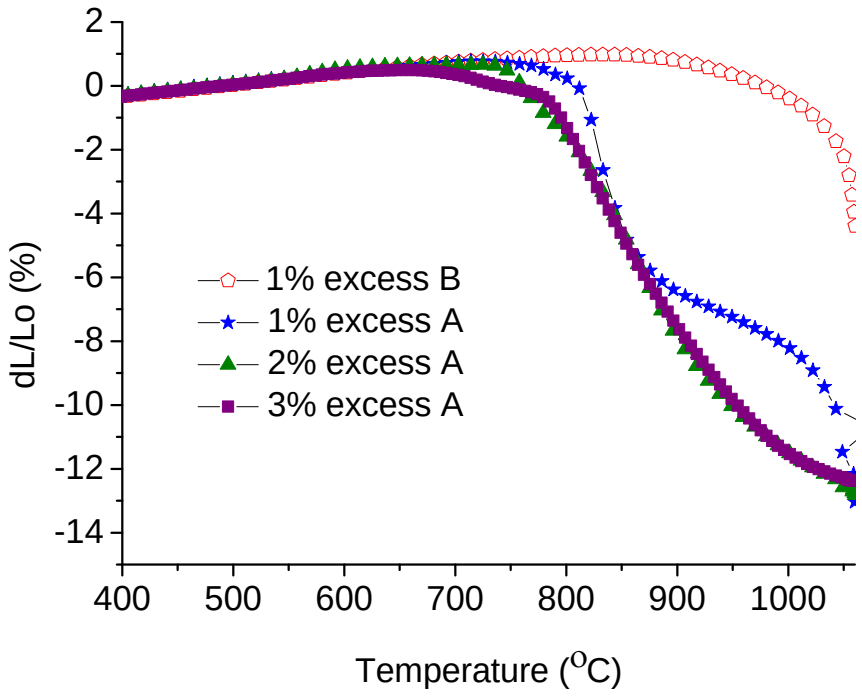

a)

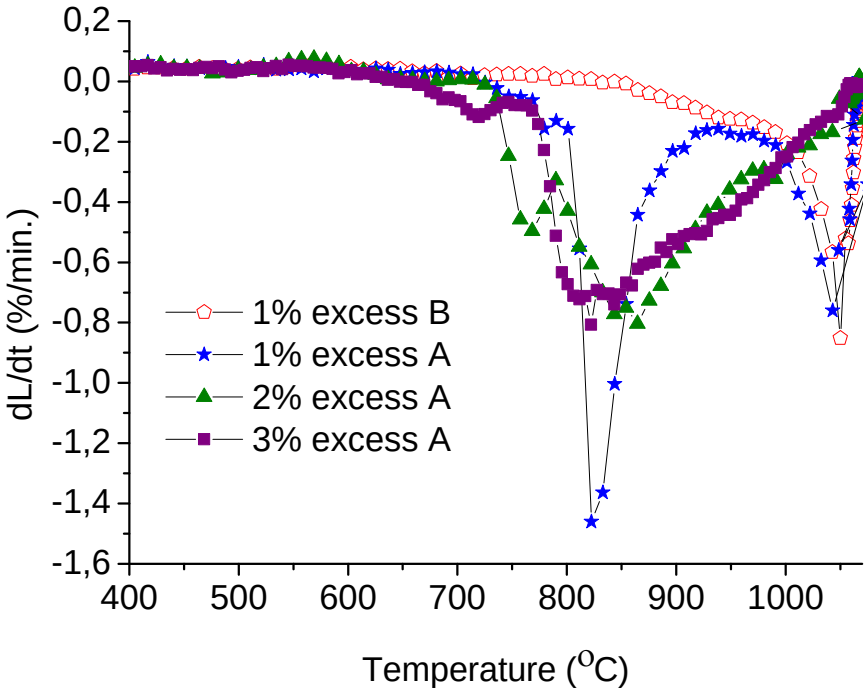

b)

Fig.3.14. Dilatometer analysis a) Shrinkage curves, b) Shrinkage rate curves of A and B excess KNN prepared with tartrate source.

3.3.7. Microstructure Investigation of Alkaline and Niobium Excess KNN Samples Produced by Tartrate Precursor

SEM micrographs of sintered 1 %A and 1% B excess compositions prepared with Na-K tartrate source were shown in Fig.3.15 . Smaller gains size were obtained for B excess composition and bigger grains were obtained for 1% A excess compositions sintering for two hour. Grain sizes was very small when the sample reached at 800°C. Grain growth was observed when the temperature reached at 925°C. This temperature resembles the end of the first shrinkage rate peak.

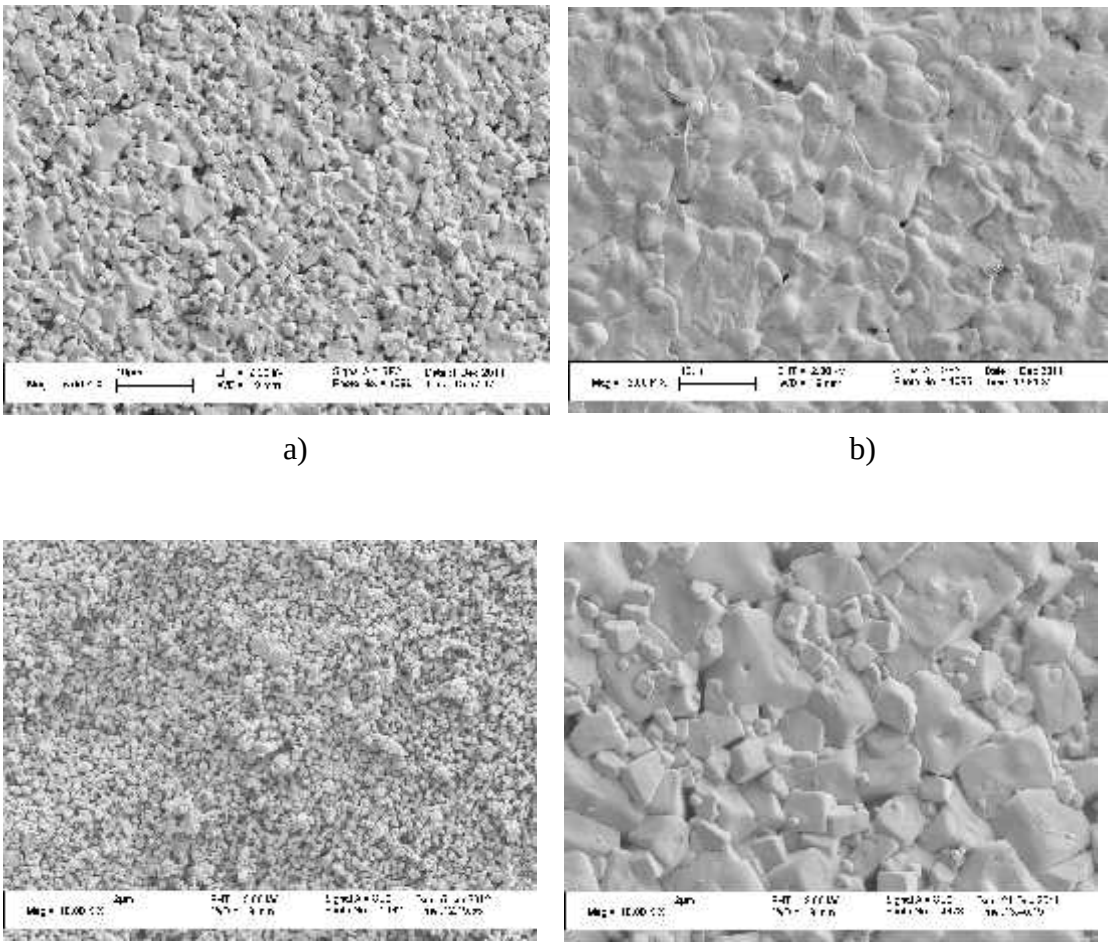

Fig.3.15. SEM micrographs of sintered A and B excess KNN samples prepared with Na-K tartrate source. a) 1% B-excess-1085°C-2h, b) 1 % A-excess-1085°C -2h, c) 1 % A-excess-800°C, d) 1 % A-excess-925°C -2h

3.4. Discussion

In this session, first, phase identifications of the synthesized powders will be analyzed for: System 1) Na and K carbonates and (monoclinic+orthorhombic) Nb_2O_5 powder and System-2) Na-K tartrate and (orthorhombic) Nb_2O_5 powder. Through the discussion C-KNN refers to system-1 and T-KNN refers to system-2 and A-excess refers to alkaline excess, B-excess refers to Nb excess. The deviation from the stoichiometry will be

discussed depending on the synthesis steps. After that, effects of excess alkaline and niobium on the morphology of the powder discussed for C-KNN and T-KNN.

After the powder synthesis, sintering of the powder compacts were analyzed by dilatometer for C-KNN and T-KNN. Sintering behavior of alkaline and niobium excess C-KNN and T-KNN compositions were studied in order to find out the effects of powder stoichiometry to the sintering. T-KNN powder washed with water and dilatometer analysis repeated. Dilatometer results of original T-KNN powder compact and water-washed T-KNN powder compact were analyzed.

Na-rich $K_{1-x}Na_xNbO_3$ solid solution appeared for niobium excess compositions produced for C-KNN . The distribution of the precursors were random for C-KNN. As the reaction in the Na_2CO_3/Nb_2O_5 diffusion couple started at 500°C, while the reaction between K_2CO_3 and Nb_2O_5 started at 600°C (the parabolic rate constant at 600°C for the Na_2CO_3/Nb_2O_5 diffusion couple was ten times higher than that of the K_2CO_3/Nb_2O_5 diffusion couple, 1×10^{-14} m^2/s versus 3×10^{-15} m^2/s, respectively) first reaction would be between Nb_2O_5 and Na_2CO_3 [53]. This preference remained constant as the reaction proceeded. First, Na rich $K_{1-x}Na_xNbO_3$ formed and then, K ions diffused through the Na-Nb oxide phases.

Another reason of this non-stoichiometry may be related to the different morphology of the monoclinic phase of the niobium oxide used for the production of C-KNN. Monoclinic Nb_2O_5 had larger particle size. As a result, the reaction rates may be different than the smaller orthorhombic niobium oxides.

Single phase KNN was obtained for alkaline and niobium excess T-KNN. The difference in the composition of T-KNN and C-KNN may be related to the reaction proceeded during the formation of KNN.

In addition, Hedwall effect might be another reason of different reactivity during the formation of KNN since KNN formation temperature was coinciding with the orthorhombic phase transformation of Nb_2O_5. Hedwall effect is defined as the reactivity increase during the phase transformation [33].

Grain sizes of the powders increased with alkaline excess composition and decrease with niobium excess composition for C-KNN. Grain size of alkaline excess KNN powder reached 1-1.5 µm which is 3 times larger than the stoichiometric composition. Bomlai [63] and co-workers explained this increased size effect of alkaline excess composition with secondary crystallization. In this process large particles grow with the consumption of small particles. They stated that if one observes secondary

crystallization mechanism during sintering of powders this could be a good indication of the presence of liquid phase in the system. As the particle size distribution of alkaline excess KNN powders were very broad, secondary crystallization and liquid formation might occurred during sintering.

Sintering behavior of T-KNN was analyzed with dilatometer. Sintering temperatures was determined as 845°. Two shrinkage rate peaks were observed.

KNN powder prepared by tartrate method washed with water and dried. Dilatometer analysis of washed powder showed only high temperature shrinkage rate peak whereas it was two before washing the powder. Therefore, low temperature shrinkage rate peak may related to Na and K rich water soluble phases which initiate rearrangement of the grains during sintering.

The sintering temperatures of T-KNN system were 700°C for 3% A excess composition, 746 °C for 2 % A excess composition, 790°C for 1% A excess composition and 950°C for 1% B excess composition. The incorporation of excess alkaline and niobium into the KNN is successful when the sintering temperature were compared with the literature.

Acker and co workers [37] reported the sintering temperature of stoichiometric, A excess and B excess KNN as 848°C, 696°C, 933°C, respectively. They observed one shrinkage rate peak for niobium excess composition, and two shrinkage rate peaks for alkaline excess and stoichiometric compositions. General trend observed in that study is similar with our results with T-KNN. They reported that although the sintering temperature was lower than liquid-solid solution formation temperature, (845°C for K_2CO_3/Nb_2O_5 and 987°C for Na_2CO_3/Nb_2O_5) low temperature shrinkage rate peak attributed to premelted grain boundary wetting film referring to the phase diagram of K_2CO_3/Nb_2O_5 and Na_2CO_3/Nb_2O_5.

Sintering temperatures (onset of shrinkage) were determined as 980°C, 750°C and 1020°C for stoichiometric, alkaline excess and niobium excess compositions for C-KNN. 2% niobium excess composition showed one high temperature shrinkage rate peak at 1060°C. 2% alkaline excess composition showed two shrinkage rate peak at 800°C and at 1050°C. 3% alkaline excess composition showed one broad and deep shrinkage rate peak between 800°C and 950 °C.

XRD analysis of sintered alkaline and niobium excess compositions prepared with Na and K carbonates showed single phase KNN. Na rich $K_{1-x}Na_xNbO_3$ phases observed in the powders disappeared.

There are important observations that link the low temperature shrinkage rate peak to liquid formation. First one is the removal of the first shrinkage rate peak of water - washed KNN. Second one is the increase in the strength of low temperature shrinkage rate peak with increasing amount of A excess composition.

Phase diagram of ternary Na_2CO_3-K_2CO_3-Nb_2O_5 system does not exist in the literature. If we imagine a ternary phase diagram composed of Nb_2O_5-K_2O-Na_2O, the binary phase diagram of $KNbO_3$ and $NaNbO_3$ would be represented by a solid line in Fig.3.16. The A excess composition is below that line. The general composition range studied was shown with red color. A excess composition is closer to the low melting temperature corners. This indicated that sintering temperature of A excess composition was lower than stoichiometric composition as we observed in our experiments.

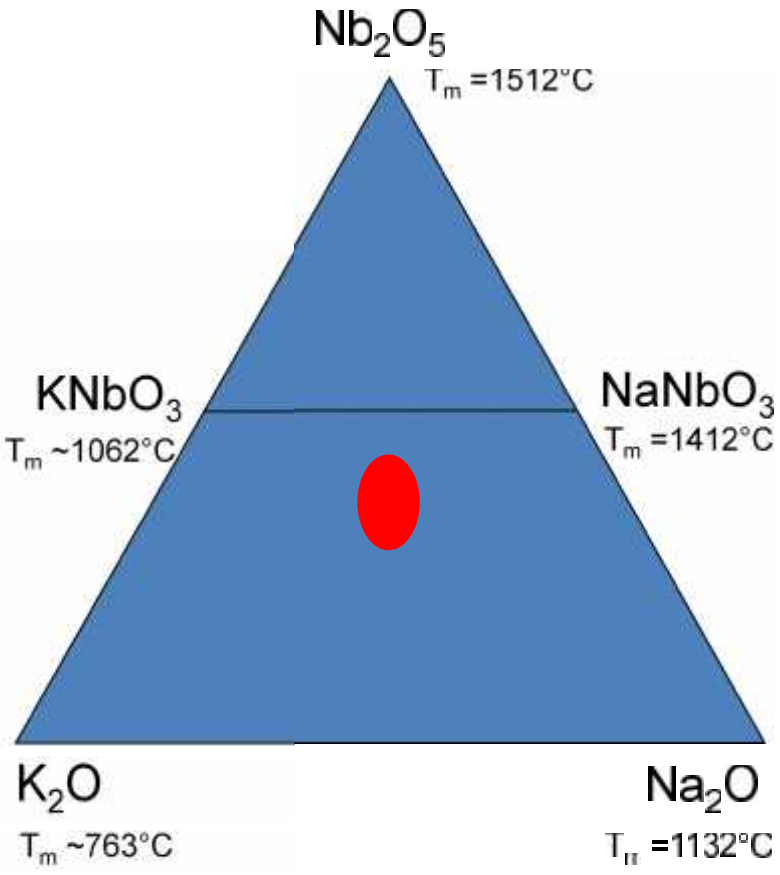

Fig.3.16. Representative ternary phase diagram

The binary phase diagram of $NaNbO_3$-$KNbO_3$ shows the melting temperature of $K_{0.5}Na_{0.5}NbO_3$ as 1140°C [39]. On the Na-rich side the solidus line starts around 1412-1425°C. On the K-rich side the solidus is as low as 1039-1075°C. Besides, pure Na_2CO_3

and K_2CO_3 have melting temperatures as 851°C and 891°C, respectively. These temperatures were too high to explain the liquid phase formation that is suspected to be below 850°C. However, Na_2CO_3 - K_2CO_3 system has a eutectic temperature at 710°C at 55 mole% Na_2CO_3 composition. Therefore, liquid formation can be explained by eutectic melting of excess alkali carbonates. This liquid phase helps the rearrangement of the grains and reduce sintering temperature during sintering.

Transient liquid phase sintering (TLPS) is a sintering technique that uses a liquid phase to facilitate densification. The liquid phase (a thin liquid film) covers and pulls the particles together by capillary forces. During TLPS, particle rearrangement, increased mass transport, and densification occurs. The advantages of transient liquid-phase sintering (TLPS) are rapid densification, lower sintering temperatures, and reduced microstructural coarsening. Low temperature melting additives produce a low melting point eutectic during sintering. As the sintering proceeds this liquid re-solidifies into the base material by diffusion. The important parameters during TLPS are the amount of transient liquid formed and its time-duration it stays as liquid phase and its interaction with the base material. There are many parameters that control these effects such as; powder size, green powder packing density, heating rate and sintering temperature [64,65].

The liquid film had appeared during the sintering of alkaline excess powder compacts and it initiate the transient liquid phase sintering. The first shrinkage rate peak was related to the rearrangement of the particles in the presence of a thin liquid film. As the sintering proceeded this liquid film favor grain growth. When it was consumed, particle-particle contacts formed and solid state sintering initiated. This sintering step was observes as a high temperature shrinkage rate peak (second shrinkage rate peak) during the sintering analysis.

Table 4.1 summarized the sintering temperatures of C-KNN and T-KNN systems. A excess compositions showed two shrinkage rate peaks. These two peaks were well separated for 2% excess A composition for C-KNN and 1% excess A composition for T-KNN. The difference was related to the Na rich $K_{1-x}Na_xNbO_3$ phases observed in the C-KNN powders. Part of the K rich excess used to rearrange the stoichiometry.

Table 4.1. Sintering temperatures of A or B excess KNN compositions prepared with tartrate, carbonate

		2%(1*%) B exc	**$K_{0.5}Na_{0.5}NbO_3$ Stoichiometric**	**1% A exc**	**2% A exc**	**3% A exc**
Sintering	**C-KNN**	1020(s)	980(s)	-	750(d)	750(d)
Temp. (îC)	**T-KNN**	950*(s)	845(s)	790(d)	750(d)	700(d)

4.5. Conclusions

Grain size of the powder increased as the alkaline amount increase. The non-stoichiometry during powder synthesis may be linked to larger grain size of monoclinic Nb_2O_5 powder compared to the smaller grain size of orthorhombic Nb_2O_5 powder, higher reaction rate of Na_2CO_3/Nb_2O_5 diffusion couple compared to K_2CO_3/Nb_2O_5 and Hedwall effect. Dilatometer analysis showed that sintering temperature decreased as A excess amount increased. Two shrinkage rate peaks were observed for A excess compositions. Low temperature shrinkage rate peak was linked to liquid phase produced by Na_2CO_3-K_2CO_3 eutectic that favor the rearrangement of the grains during sintering. The intensity of first shrinkage rate peak was related to A excess amount. Transient liquid phase sintering was proposed as the active sintering mechanism of A excess compositions.

CHAPTER 4

4. MICROSTRUCTURE AND MICROCHEMISTRY OF FLASH SINTERED SODIUM POTASSIUM NIOBATE ($K_{0.5}Na_{0.5}NbO_3$)

4.1. Abstract

Flash sintering experiments were performed, for the first time, on sodium potassium niobate (KNN) ceramics. A theoretical density of 94% was achieved in 30 seconds under 250 V/cm electric-field at 990°C. These conditions are ~100°C lower and faster than the conventional sintering conditions. Grains tended to grow after 30 s. flash sintering duration under constant electric-field. Detailed microstructural and chemical investigations of the sample showed that there was inhomogenous Na, K distribution and it resembles a core-shell structure where K is more in the shell and Na is more in the core region. The inhomogenous distribution of Na and K was correlated with the doubling of the unit cell within the grain along 002 direction. Compositional equilibrium is achieved after a heat treatment at 1000°C for 4 hours. The compositional variations appeared to have been linked to grain boundary melting during flash and consequent recrystallization as the sample cooled.

4.2. Experimental Procedure

$K_{0.5}Na_{0.5}NbO_3$ powders were synthesized by conventional solid-state method. Calculated amounts of Na_2CO_3, K_2CO_3 and Nb_2O_5 were ball milled for 12 hours in isopropanol environment with zirconia balls. Prior to mixing the powders in stoichiometric ratios were dried for 3 hours at 200°C to remove the adsorbed water from these compounds. KNN powders were synthesized at 800°C for 2 hours. After mixing the synthesized powders with binder, 2 wt % polyvinyl butyral (PVB), dog bone-shaped specimens were uniaxially pressed at 200 MPa. The gauge section of the dog bone was 20 mm x 3.5mm x 1.2 mm. The green density of the sample was around 0.63. Samples were held at 550°C for 1 hr. for binder burn out. Sintering experiments were conducted by applying a voltage to the specimen while the furnace temperature was increasing at a constant heating rate. Fig.5.1 shows a schematic of flash sintering experimental set up. Two platinum electrodes were used both to suspend the dog bone shaped sample and to apply electric-field to the sample. Constant voltage was applied to the sample after 550°C while the temperature was increasing at a rate of 10°C/min. Sintering was performed at 250 V/cm, 20 mA/mm^2 for 10, 30 and 60 s. in air atmosphere. Conventional sintering of pellets made up of the same powders was conducted at 1100°C for 2 hours in air for comparison.

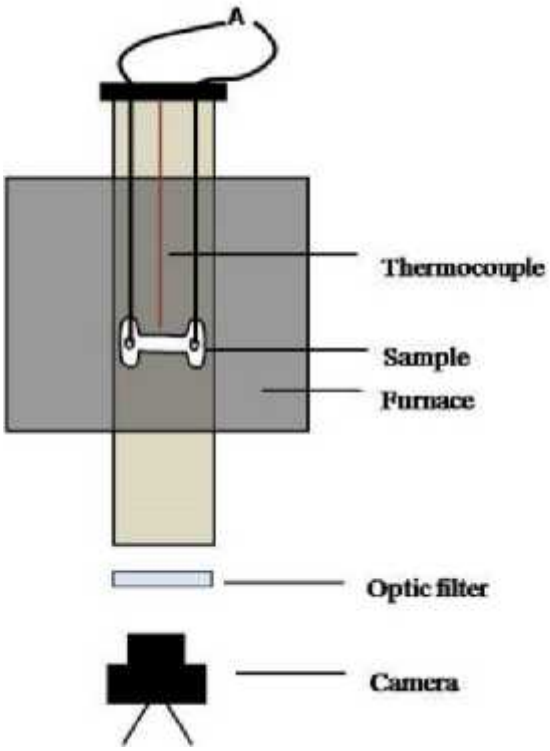

Fig. 4.1. The schematic of flash sintering set up.

Shrinkage data were recorded by a CCD camera by taking photographs of the sample ten frame per second. Densities were both measured by Archimedes method and analyzed from SEM micrographs of the polished samples by UTHSCSA Image Tool Program (developed in the Department of Dental Diagnostic Science at The University of Texas Health Science Center, San Antonio, Texas).

Platinum paste was used to provide good electrical contact between sample and platinum wires and to form a uniform electric-field through the gauge section of the sample.

Density of the sample was calculated by linear shrinkage data of the sample. Linear shrinkage strain was calculated with the equation $\varepsilon=\ln(L/L_o)$, where L_o is initial length, L is time dependent gauge length, $^{\circ}{}_{g}$ is green density. Density is calculated with the equation $\rho=\rho_g e^{-3\varepsilon}$ where ε is linear shrinkage strain.

Specimen temperatures were estimated from Black- Body radiation model. Steady-state power density values were used to calculate the specimen temperature. According to the model, relation between the specimen temperature and furnace temperature is given by the formula [25].

$$\frac{T^*}{T_0} = \left[1 + \frac{1}{\sigma T_0^4}\frac{W}{}\left(\frac{V}{A}\right)\right]^{1/4} \qquad \text{(Eq.1)}$$

where T_0 is the furnace temperature (K), T^* is the specimen temperature (K), *Wv is* the power dissipation per unit volume of the specimen (mW/mm^3), *V/A* is volume to surface area of the specimen and σ is the blackbody radiation constant equal to 5.67×10^{-8} W/(m^{2}K^4). Structural characterization was performed by using X-Ray powder diffractometer, (Bruker AXS D8 Advance, Karlsruhe, Germany), by using Cu Kα radiation. SEM micrographs and chemical analysis were done by SEM JEOL 6010 LV equipped by EDX detector. Polished (down to 1μm by diamond paste) surfaces were examined by secondary electron mode. TEM sample was prepared by Focused Ion Beam (FIB) and was examined in a JEOL ARM200 ColdFEG, high-resolution, scanning transmission electron microscope (HR-STEM). Chemical composition was investigated by analytical electron microscopy utilizing a STEM equipped with an EDS spectrometer (JEOL Centurion EDX spectrometer).

4.3. Results

4.3.1. Investigation of Flash Sintering Parameters

Sample was recorded with a CCD camera during the experiment. Fig. 4.2 shows the images of the sample taken during flash sintering. Picture number 1 resembles just before the flash, number 2: initiation of flash and number 3: during flash.

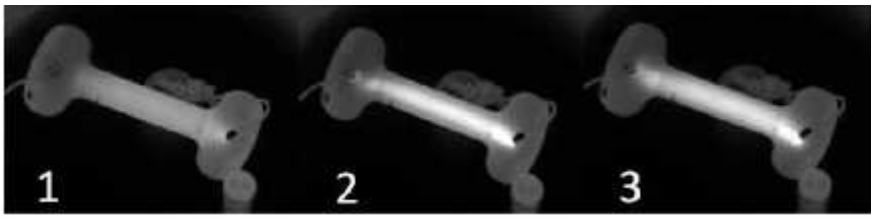

Fig. 4.2. Images of the sample before the flash, initiation of flash and during flash sintering.

X-Ray Diffraction analysis showed that both conventional sintered and flash sintered samples had a “single phase” KNN. There were no secondary ‘phases’ forming during flash sintering. Results of a constant heating rate experiment conducted at 250 V/cm and 20 mA/mm^2 are shown in Fig.4.3. The flash sintering has two main regimes. The first part of the event spanned the time from the start of the experiment until the power spike was observed. During this period the voltage was kept constant. This part is named voltage-control region. After the power spike, when the current limit of 20 mA/mm^2 was obtained, the current-control region commenced. During constant current region, electric-field and the power dissipation settled into a quasi-steady state value at about 50 V/cm and 109 mW/mm^3, respectively. Power dissipated in the sample was calculated by multiplying applied voltage with the current. The sharp increase in the power was related to the sudden increase in the conductivity of the sample in the voltage-control region. When current limit was reached, the voltage in the specimen began to drop causing a decrease in power dissipation. After a short period, power dissipation tended towards a quasi-steady state as shown in Fig.4.3 (current-control region). In this stage, the conductivity of the sample is higher as it is shown in the drop of the voltage value .

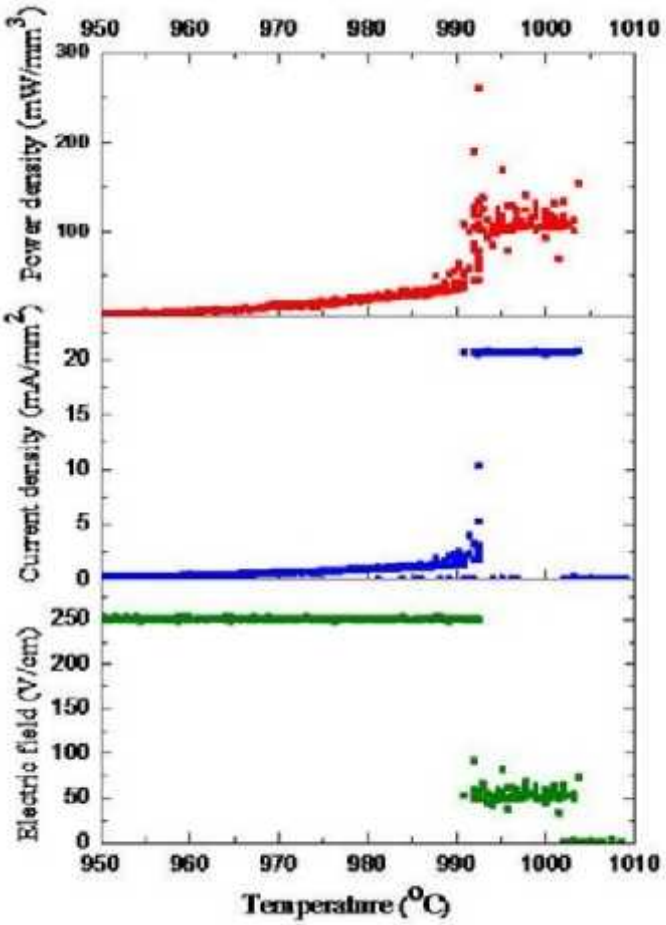

Fig.4.3: Flash sintering cycle with applied field, current density, power density with respect to temperature.

Constant heating rate experiments were conducted to investigate the flash sintering temperature at different electric-fields between 100-500 V/cm. The reported flash temperatures were taken as the temperature where steep increase in power density (i.e. in conductivity) was observed (Fig.4.4).

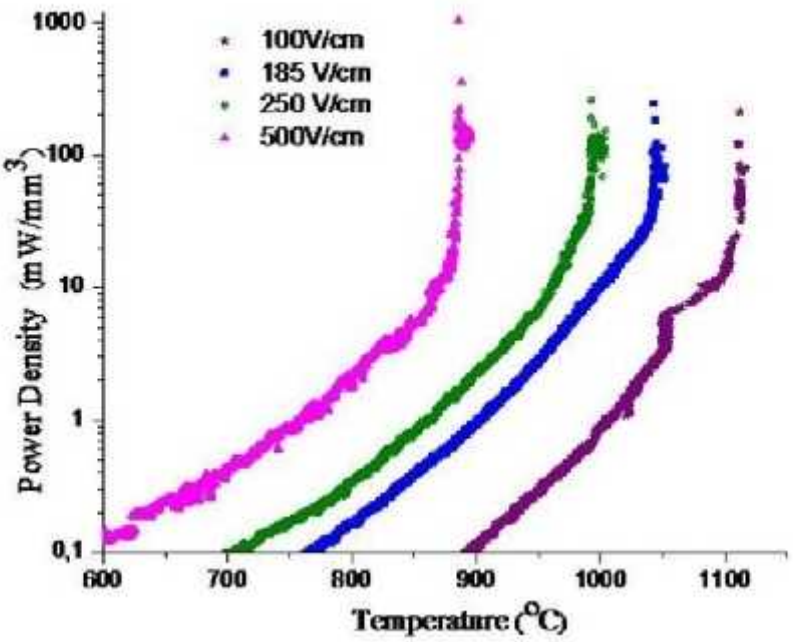

Fig.4.4. Power densities for the samples with different electric-fields at 20 mA/mm^2 current density for constant heating rate experiments (logarithmic scale was used for y-axis)**.**

As the applied electric-field increased both peak value of power dissipation and power dissipation at quasi-steady state (i.e.current control region) increased. Power densities for different field strengths at quasi-steady state are shown in Table 4.1. Specimen temperatures were calculated depending on the black body radiation model in Eq.1. Sintering at lower electric-fields required high temperatures to flash. The (calculated) specimen temperatures for lower fields were very close to the melting point (1140°C) of the sample taken from the phase diagram.

Table 4.1. Change in flash sintering temperature at different electric-fields, at 20 mA/mm^2 for constant heating rate experiments**.**

E.Field-Current Density (V/cm)- (mA/mm^2)	**PowerDissipation (mW/mm^3)**	**SpecimenTemp. (Calculated) (îC)**	**FlasTemp. (îC)**
100-20	54	1127	1090
185-20	80	1120	1040
250-20	109	1096	990
500-20	135	1029	900

Fig. 4.5. shows the correlation between power density and densification. Power density is plotted on left y-axis and relative density is plotted with dotted curve referring to on the right y-axis. A rise in conductivity (power density) and rapid densification in the sample appeared to be simultaneous. Sample continued to shrink during current control region.

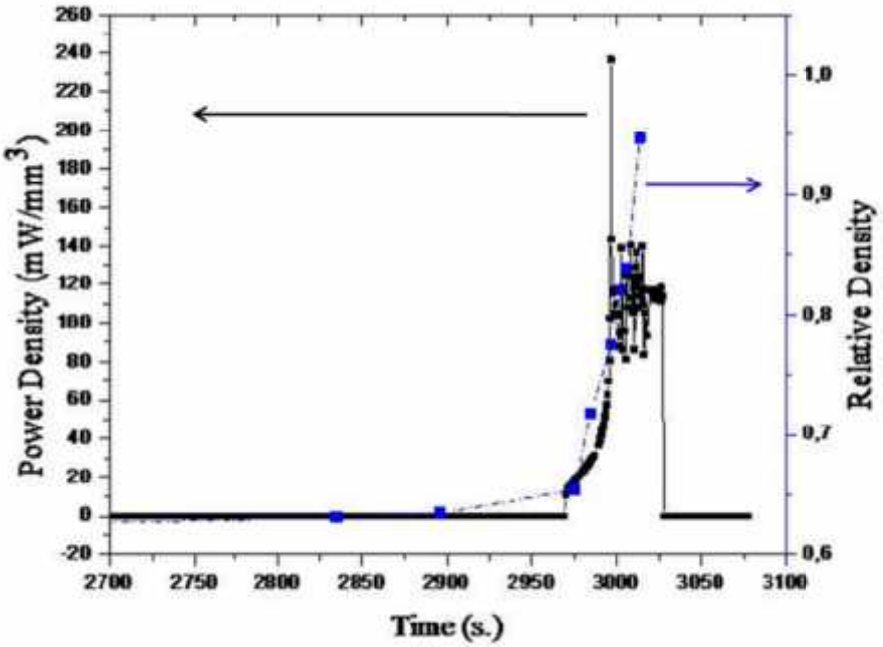

Fig.4.5: Power density and relative density data of flash sintered sample at 250 V/cm, 20 mA/mm^2.

Linear shrinkage strain data of conventionally sintered and flash-sintered samples at different electric-fields are shown in Fig.4.6. During flash sintering experiments the sample moved at the later stages of the measurement. Therefore, the full shrinkage range could not be measured/observed for flash sintered samples. Therefore, the last data point in the linear shrinkage curves did not correspond to the final shrinkage. For conventionally sintered sample (black curve) after 900 °C a gradual decrease in length of the sample was observed. For flash sintered samples a sharp shrinkage was observed starting at the power spike temperature. With increasing the field strength, flash temperature and the shrinkage temperature decreased. The highest linear shrinkage was observed at a field strength of 250 V/cm. Current localization was observed for a sample that was flash sintered at a very high field of 500 V/cm. (image not shown). This sample was not sintered homogenously and the final density was rather low. While keeping the electric-field at 250 V/cm, when the current density was increased to 40 mA/mm^2 , melting was observed in certain regions of the sample that were close to the platinum wires. At the low current density limit (7 mA/mm^2), the current was not enough to spread the flash through the sample.

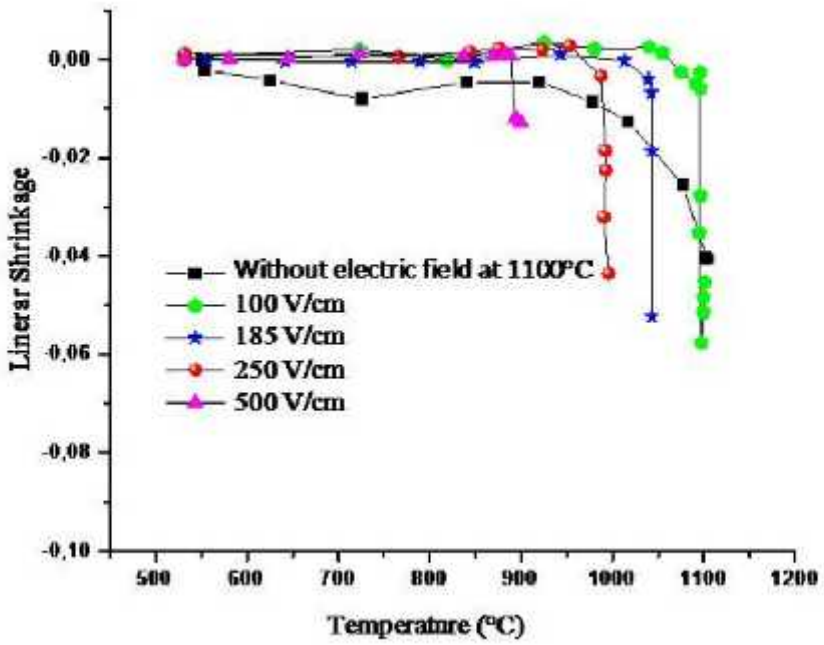

Fig. 4.6. Linear shrinkage strain for conventional and flash sintered samples at different electric-fields. (All samples were flash-sintered at a constant 20 mA/m^2 current density)

Density of the samples were measured by Archimedes method and analyzed by UTHSCSA Image Analysis Program from polished surfaces of the samples shown in

Table 5.2. For samples with low density, Archimede's technique consistently gave lower densities due to incomplete wetting of open pore surfaces (i.e. for samples with densities lower than 95 % of theoretical density). The highest density (94.6 ± 0.1 %ThD) was obtained for the sample flash sintered at 250 V/cm-20 mA/mm^2 for 30 s. The density of the samples decreased for samples subjected to prolonged flash-sintering conditions. The de-densification tendency in KNN ceramics with longer sintering times could be seen in the samples flash-sintered for 60 s under 250 V/cm field strength and 20 mA/mm^2 current density. Grain growth was observed after 30 s. sintering duration (Fig.4.7).

Table 4.2. Density of the samples flash sintered and conventional sintered**.**

E.field-Current density-time	**Density (Th.D)** % **(Archimedes)**	**Density (Th.D)** % **(Image Analysis)**
100 V/cm-20 mA/mm^2-30 s.	79	89.8 ± 1.3
185 V/cm-20 mA/mm^2-30 s.	84	89.0 ± 1.3
250 V/cm-20 mA/mm^2-30 s.	94	94.6 ± 0.1
250 V/cm-20 mA/mm^2-60 s.		92.0 ± 0.8

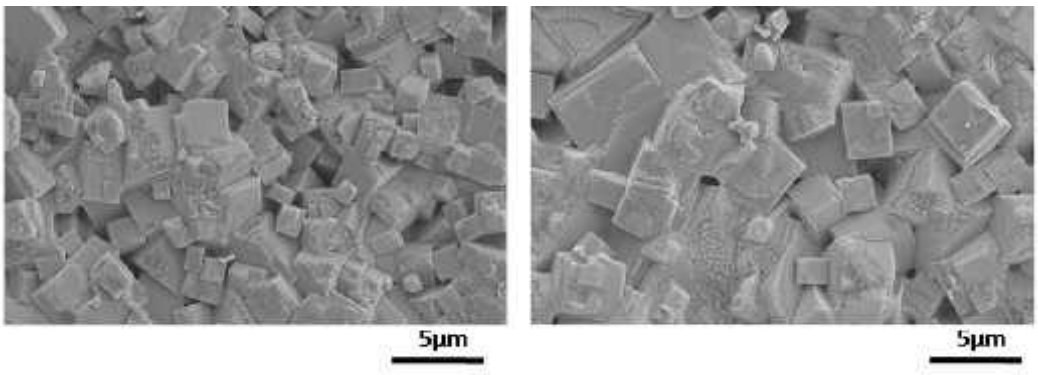

Fig.4.7**.** SEM micrographs of flash sintered samples at 250 V/cm, 20 mA/mm^2 for a) 30 s**,** b) 60 s. (After 30 seconds of flash-sintering grain growth became obvious).

4.3.2. Micro-chemistry Analysis of Flash Sintered KNN

Chemical composition of flash sintered sample (250 V/cm electric-field, 20 mA/mm^2 for 30 s.) at micrometer level was investigated using an SEM (JEOL 6010 LV) equipped with an EDX detector. EDX mapping analysis, shown in Fig.5.8, revealed

while O and Nb distributions were homogenous, the distributions of Na and K were not. Regions rich in Na was depleted of K and vice versa. The EDX mapping revealed a core-shell type microstructure where K-rich regions seemed to constitute the shell around the Na-rich regions.

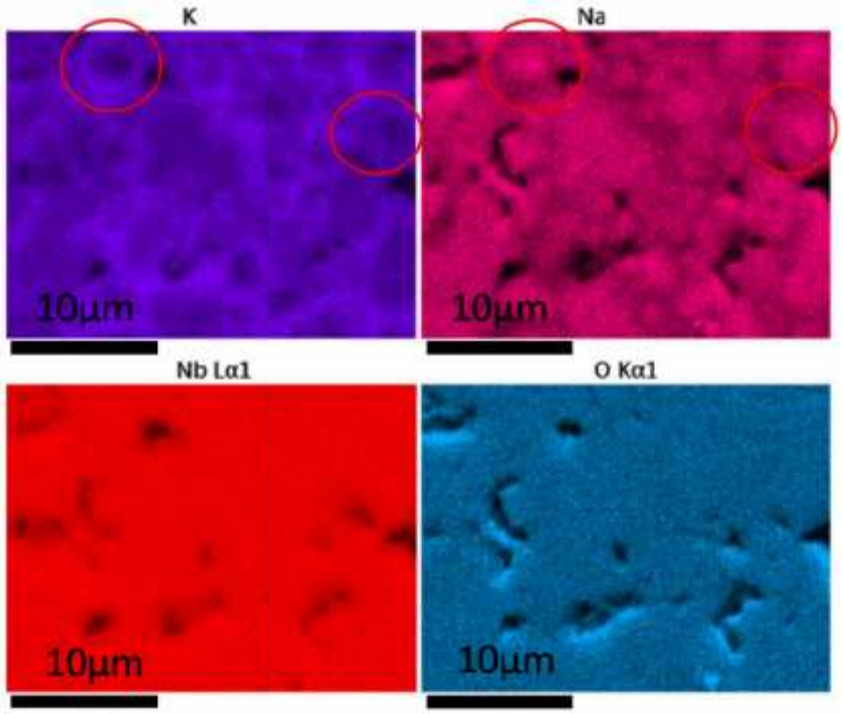

Fig.4.8**.** Elemental mapping of Na, K, O, and Nb for flash sintered sample at 250 V/cm electric-field, 20 mA/mm^2 for 30 s. Circles indicate core-shell regions.

When a flash sintered sample was heat treated at 1000 °C after 4 hours the core-shell morphology has disappeared (Fig.4.9). It was observed that 4 hours of conventional heat treatment was enough to diffuse K ions into the core and Na ions outwards to shell to establish the equilibrium stoichiometry of KNN.

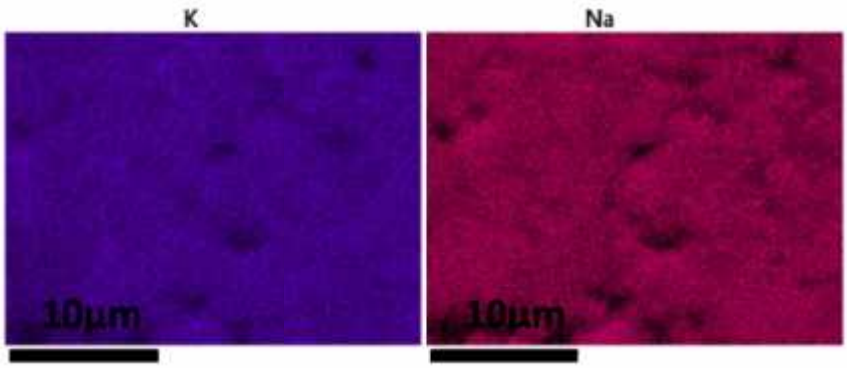

Fig.4.9**.** Elemental mapping of Na and K for flash sintered and heat treated sample at 1000 °C for 4 hrs

Densities of flash sintered for 30 s. and flash sintered + heat threated samples are 94% and 95.5%, respectively. Reduction in the pore size was observed with the heat treatment.

Table 4.3 shows the results of EDX chemical composition of Na, K and Nb. During the point analysis of different regions for quantification Na Kα, K Kα and Nb Lα spectral lines were used. Na/K ratio in the shell is about 0.75 whereas it is 1.53 in the core. After the 4 hour heat treatment Na/K ratio became 0.90. For quantification, k-correction factors listed in the manufacturer's tables were used.

Table 4.3**.** EDX Quantification values of flash sintered and flash sintered+heat treated sample

		Na	**K**	**Na/K**
Flash sintered	Shell-K rich region (% atomic)	42.7	57.3	0.75
	Core-Na rich region (% atomic)	60.5	39.5	1.53
Flash sintered+heat treated		44.6	49.4	0.90

For conventionally sintered sample Na and K distribution was homogenous. Na/K value was 0.90. Na value is slightly lower than K. In the literature Na_2O evaporation was given as the main cause of this discrepancy (Fig.4.10). Another reason for this deviation from nominal Na/K ratio could be the difficulties in measuring Na/K ratio without an internal standard [66].

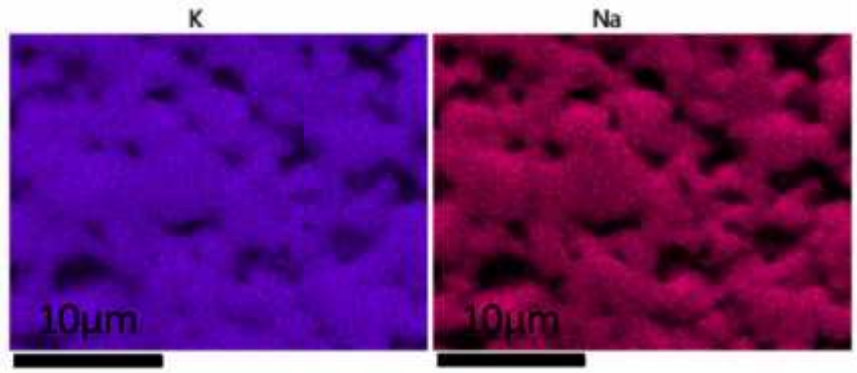

Fig.4.10. Elemental mapping of Na and K for conventionally sintered sample at 1100 °C for 2 hrs**.**

The sample flash sintered at 250 V/cm electric-field, 20 mA/mm^2 for 30 s. was investigated with a scanning transmission electron microscope (STEM) to have a better understanding of this heterogeneous cation distribution. HRTEM image of the grain

boundary in flash-sintered sample is shown in Fig.4.11. The image was taken with the part of the boundary set at edge-on condition. Neither an amorphous layer nor second phase were observed within grain boundary.

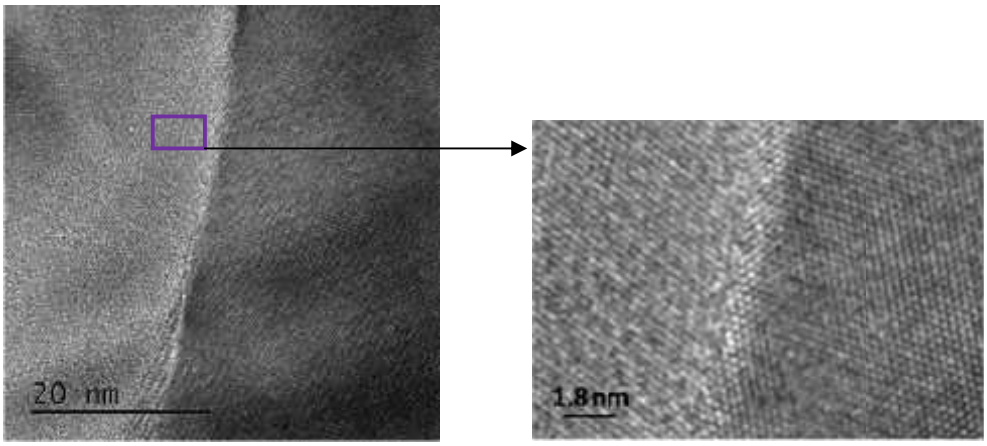

a) b)

Fig. 4.11**.** a) HRTEM image of the grain boundary, b) Enlarged view of grain boundary in the rectangle**.**

Annular dark field scanning transmission electron microscope (ADF-STEM) image and the corresponding EDX elemental distribution maps for Na and K are shown in Fig.4.12. The microstructure appears to be chemically heterogeneous in terms of sodium and potassium distribution. In the EDX map sodium-rich regions were presented with red color and potassium-rich regions were presented with green color. Therefore the orange color corresponded to sodium rich regions that also contained some amount of potassium. The predominantly green grain in the middle of the map appeared to be potassium niobate. The edges of triple point pockets appeared to be sodium covered. A closer examination of ADF-STEM image along with EDX maps revealed that the chemical heterogeneity was at the intra-grain level, i.e. a certain core-shell appearance was observed in some of the grains.

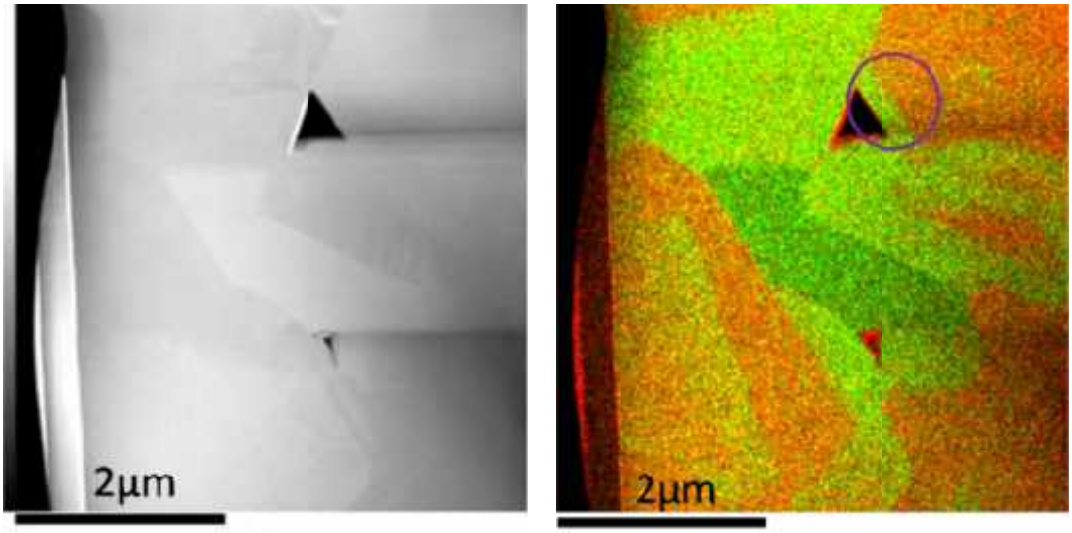

a) b)

Fig.4.12. a) STEM ADF image, b) STEM-EDX color maps: K and Na ion distribution (K: green, Na: red)**.**

The region shown in the upper right corner of Fig.4.12-b (circled) was analyzed by dark field imaging (DF-TEM) This region was composed of only one grain. DF-TEM image of that region is shown in Fig.4.13. It revealed that the chemical boundary was within a single grain. Inside this grain several defects could be observed. The chemical boundary was in between these defects (indicated with red arrow) and did not overlap with any visible defect (Fig.4.13).

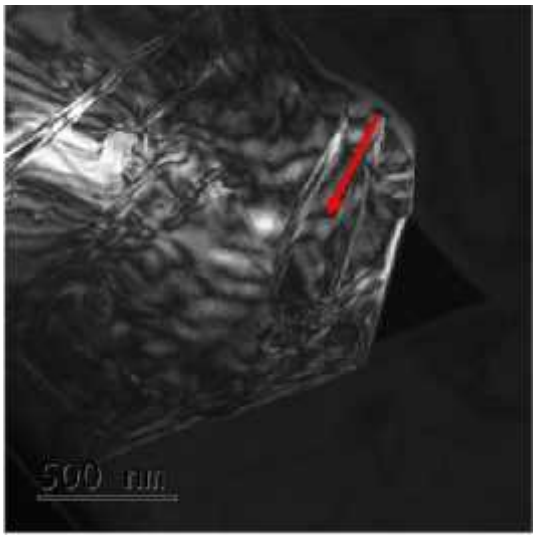

Fig.4.13**.** Dark field TEM image of the region shown in Fig 4.12-b indicated with a circle. The two images are rotated with respect to each other. The triangular hole (dark in both images) is the reference feature.

Chemical boundaries were not coinciding with structural boundaries as would be expected. From TEM bright field images and from diffraction analysis, the grain boundaries were determined and overdrawn on to the EDX elemental map in Figure 4.14. In the chemically heterogeneous region diffraction analyses were performed. Indexing of diffraction patterns were done by using FindIt and JEMS computer programs. Fig.4.14-a) shows how Na and K atoms were distributed between and within the grains.

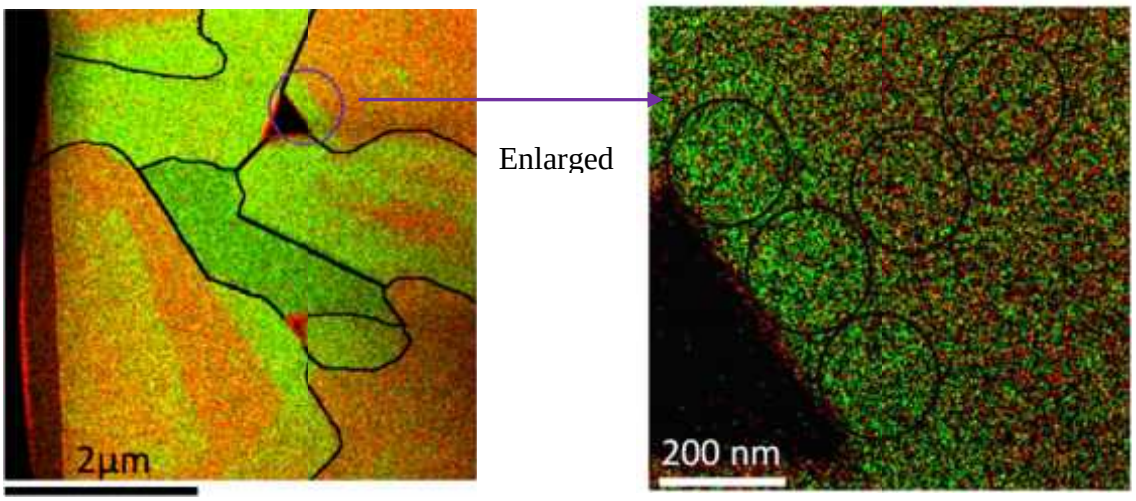

a) b)

Fig.4.14. STEM-EDX color maps showing K and Na ion distributon (K: green, Na: red), a) Grain boundaries as determined from diffraction analysis b) Enlarged view of the edge region encircled near the triple point pore.

Fig.4.14-b shows the zoomed-in area that is indicated in Fig 4.14-a with a circle. Although the boundary between the two regions with different chemical compositions was roughly parallel to a crystallographic plane, the boundary was not atomically sharp, i.e. not bound by a single crystallographic plane. Diffraction analyses done in the two chemically different regions within the same grain revealed that the two regions are structurally not equal either. The diffraction patterns taken from the K-rich region showed , orthorhombic [120] zone axis pattern belonging to Bmm2 space group where [00l] is present if l is even (or pseudo-cubic [112] zone axis) (Figure 5.15-a). On the other hand, the diffraction patterns taken from Na-rich regions showed same zone axis with extra weak spots between the (002) strong spots (or pseudo-cubic [112] zone axis with weak spots between the $(\bar{1}10)$ strong spots) (Figure 4.15-b).

Further crystallographic studies are underway to determine the structural modification that will give rise to such superlattice spots. At the moment it should suffice to say that they may be indicative of an ordering in [001] direction. It appears that the unit cell in this direction may be doubling in size. One possible reason for this could be a cation ordering giving rise to the diffraction pattern as shown in Fig.4.15-b. Another explanation was given by Woodward and Reaney as alternation of octahedra tilt in consecutive unit cells [67]. Two more grains with chemical K-Na zoning were studied and similar structural modification was observed.

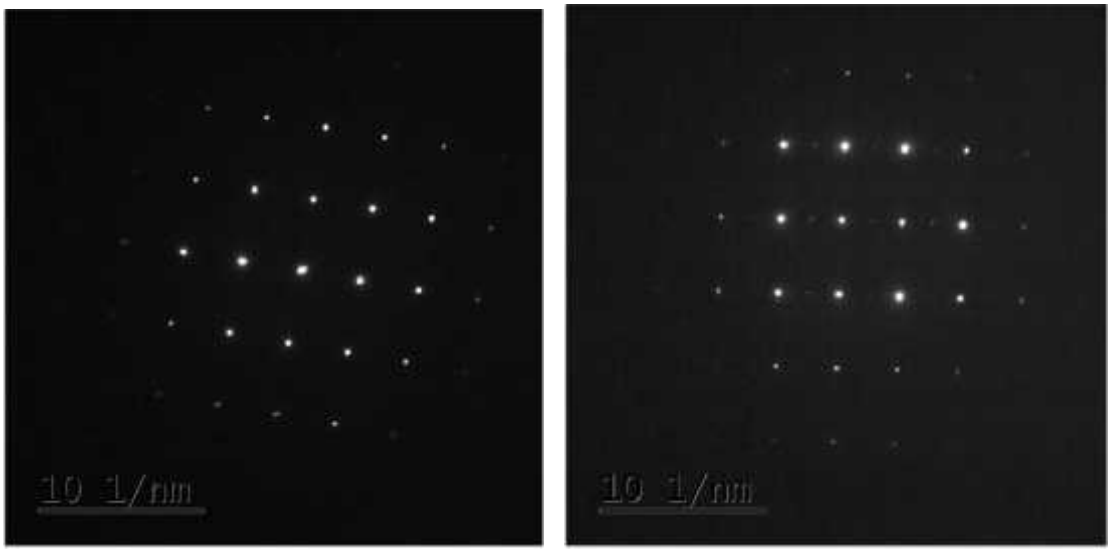

Fig.4.15**.** Diffraction patterns of a) K rich region, b) Na rich region**.**

In the literature Zhang S. and co-workers [68] investigated $K_{0.5}Na_{0.5}NbO_3$ ceramic by TEM. They observed two different regions along [112] zone axis. One of them contained strip-like domains. The other region was without domain contrast (featureless-domain). They claimed that depending on the KN–NN phase diagram, room-temperature $K_{0.5}Na_{0.5}NbO_3$ is a mixture of two phases without oxygen octahedral tilt: the K-rich Amm2 ($a^0a^0c^0$) phase and the Na-rich Pm ($a^0b^0c^0$) phase. They found a correlation between striplike domain and higher K content by EDX–measurements. Certainly, further studies are necessary to bring a better explanation to the structural modifications happening to KNN during flash-sintering.

4.4. Discussion

After the flash sintering a strong tendency for facetting was observed under all sintering conditions (Fig.4.7). Cube-like grains with large number of surface steps parallel to dominant crystallographic planes comprise the microstructure. Such steps are possibly reminiscent of strong facetted grain growth during flash sintering [69] . Highest density, 94% Th.D., was observed for 30 s. sintering duration. Rapid grain growth started after 30 s. of sintering. This rapid grain growth coupled with strong facetting may be the reason for a reduction in density after 30 s. Although facetting was observed in the conventionally sintered samples it was not as dominant as it was in flash-sintered ones.
Table 5.4 shows flash sintering temperatures and corresponding applied fields for other materials. Although flash sintering is applicable to a different range of materials (ionic or electronic conductors or even to dielectric materials), (flash) sintering temperature and corresponding applied field are material dependent. For a mixed conductor like $CoMnO_4$, flash sintering was achieved at 7.5 V/cm and 400 °C, whereas for the insulator Mg doped Al_2O_3 higher than 1000 V/cm was necessary at 900 °C to achieve a flash. As the conductivity (both ionic and electronic) of the "insulator" is increasing, both the electric-field and temperature required for flash-sintering tends to decrease. KNN being a piezoelectric insulator ceramic with negligible electronic conductivity behaves more similar to alumina than $CoMnO_4$ in flash sintering.

Table 4.4. Flash sintering temperatures and corresponding applied fields for materials.

Materials	**Flash Temperature**	**Applied Electric-Field**	**References**
ZnO-single crystal	870	300	30
ZnO powder	553	44	30
0.5 mol Bi_2O_3+ZnO	620	21	30
$SrTiO_3$	900	500	24
Co_2MnO_4	400	7.5	22
Mg doped Al_2O_3	900	>1000	21
TiO_2	800	250	25
$8Y_2O_3$-ZrO_2	900	~100	20
KNN	990	250	this study

KNN samples flash sintered in this study revealed a core-shell structure and intra-granular variation in Na and K concentrations. There could be several origins for the existence of the observed "chemical" core-shell structure. One reason may be incomplete reactions during powder synthesis. The different decomposition temperatures of potassium and sodium carbonates could have caused heterogeneity in the KNN powders. However, powders used in these experiments were examined using SEM for core-shell structure before compacting. The powders did not show any chemical core-shell morphology. Another reason of this core-shell structure may be local melting starting at the grain boundaries due to joule heating. During the flash, the joule heating might have raised the temperature near the grain boundaries above the solidus temperature. This would create a K-rich liquid at the boundaries according to the equilibrium phase diagram between $KNbO_3$ and $NaNbO_3$ [2,39]. During the flash because of local heating, the compositions of the melt and the neighboring core will change due to inter-diffusion between liquid shell and the solid core. During cooling liquid phase would recrystalize with a compositional gradation.

After flash sintering the Na/K+Na ratio of the core region was measured as ~60.5% with the help of EDS system attached to a SEM. The same ratio was ~43% in the shell.

KNN is a complete binary solid solution between $KNbO_3$ (Tm ~1090°C) and $NaNbO_3$ (Tm ~1420°C) [2,39]. Small temperature changes below and above the solidus would create large compositional variations in the liquid and the solid. The KNN composition used in this study was 50% $KNbO_3$/50% $NaNbO_3$. However, the composition of the shell was measured as 57% $KNbO_3$ and 43% $NaNbO_3$. The composition of the core was nominally 40% $KNbO_3$ and 60% $NaNbO_3$. Assuming that the compositional variations during cooling would be slower in the solid phase, i.e. in the core region, one can estimate the most likely temperatures that the boundaries in the polycrystalline ceramic could have reached during the flash. The 40:60 $KNbO_3$:$NaNbO_3$ solid composition would correspond to 1150°C for a 50:50 starting composition. This 40:60 $KNbO_3$:$NaNbO_3$ solid composition would be in equilibrium with a 78:22 $KNbO_3$:$NaNbO_3$ liquid composition as predicted in the phase diagram. The $KNbO_3$-level in the re-crystallized shell region of the sample was lower than expected. It was observed that some of the excess K was accommodated in the $KNbO_3$ grains that formed in the microstructure as shown in Figure 4.12-b. Some of the K_2O may have evaporated during the flash.

A model for the systematic of core-shell formation was explained in Fig.4.16 and in the following text;

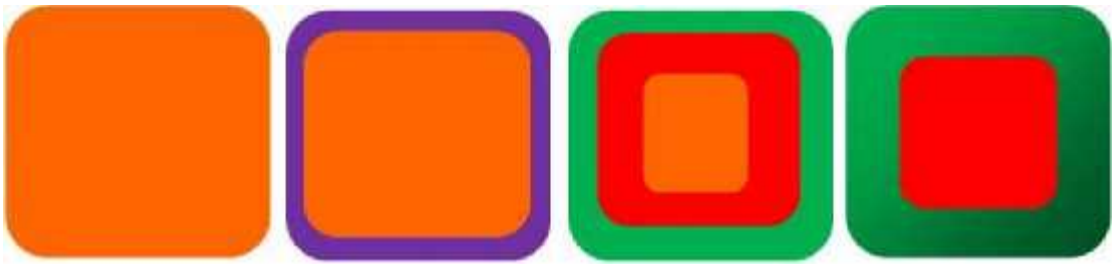

a) b) c) d)

Fig.4.16. Schematic of core-shell formation a) original compositon $K_{0.5}Na_{0.5}NbO_3$, b) liquid formation, c) solidification of liquid with new composition, d) rearrangement of the solid composition)**.**

The starting composition was 50%$NaNbO_3$-50%$KNbO_3$ (a). During the flash grain boundary melting occurs and renders the liquid composition rich in potassium (b). After the flash during cooling (c) a K-rich shell and Na-rich core appear with maybe a small amount of original composition in the very center of the original grain. During the further sintering this small original composition may also be adjusted as shown in (d).

Different levels of homogeneity in the particle chemistry were possible due to different particle sizes and corresponding diffusion distances during the chemical variation in sintering.

Most of the studies on the subject claim there is a link between core-shell formation and liquid phase during sintering not only in KNN ceramics but also in other ceramic materials like $BaTiO_3$. Core-shell structure was observed for (1 - x) $Na_{0.5}K_{0.5}NbO_3$– $xLiTaO_3$, modified with $BiScO_3$, x=0.5 composition [70]. In this study core-shell segregation was explained with an absence of a liquid phase during sintering. Addition of liquid-phase forming excess alkali metal oxides prevented core-shell appearance. It was suggested that producing a transient liquid phase promoted inter-diffusion and improved chemical homogeneity. Zhang and co-workers [68] investigated cooling effect on the microstructure of KNN samples sintered in the solid+ liquid region (sintered at 1170-1200 °C) of the phase diagram for x=0.5 composition. Na and K inhomogeneity was mostly reported in quenched samples. In those samples, they obtained disproportionation of alkalis into (i) K poor region, (25% K/K+Na), with an excess K-rich liquid film (57% K/K+Na) in the boundary and (ii) K richer regions (K/K+Na 37-44%). For furnace cooled or slow cooled samples, chemical heterogeneity

was observed in different regions of the samples with K/K+Na ratios between 44% to 24%. They concluded that slow cooling let system to establish a more homogenous distribution of Na and K.

The formation of core-shell type chemical segregation during sintering was studied with different dopants in $BaTiO_3$ ceramics. Two mechanisms were proposed: First one explains the shell formation by solid-state diffusion of dopants into $BaTiO_3$ particles. Second one explains the shell formation by dissolution/precipitation of dopant from a liquid [69].

Jeon S.-C and co workers worked with bi-layer samples with different chemical compositions ($94BaTiO_3–2Y_2O_3–2MgO –2SiO_2$ (mol%) and $98BaTiO_3–2SiO_2$ (mol%)) and grain sizes. They found a close crystallographic relationship between the core and the shell which was interpreted as an indication of an epitaxial grown layer by dissolution of small grains and precipitation of the dissolved material onto the growing grains. The electron-diffraction patterns from the core and the shell region showed that they have the same crystallographic orientation and the coherent interface between the core and the shell observed by HRTEM (High-Resolution TEM) confirming epitactic relationship [71].

Randall et al. suggested that [72] formation of liquid phase is a prerequisite for the formation of core-shell structure. In addition, they suggest other prerequisites such as: solubility of $BaTiO_3$ into the glass, reprecipitation of $BaTiO_3$ including additives in perovskite structure, limited grain-growth process and limited inter diffusion such that a homogeneous distribution of dopants would be retarded. The process was explained as follows: for $BaTiO_3$ system when the saturation level of liquid phase was established in terms of $BaTiO_3$, solution-precipitation proceeded by dissolution of smaller grains and growing of larger ones. As the process continued, concentration of the additives in the solid increased whereas it was depleted in the liquid. They claimed that the concentration difference between the core and shell created a driving force for diffusion. Since the core-shell morphology was a thermodynamically unstable structure, high sintering temperatures and/or long sintering times provided a more homogeneous distribution and eliminated the core-shell. Lu et al. reported homogenization in the $BaTiO_3$-ZrO_2 system with up to 60 h of sintering [73]. Chemical homogenization was also shown in this study when the flash-sintered core-shell structures were annealed at high temperatures.

In this study EDX quantification of core-shell morphology indicated that a liquid grain boundary region formed during flash. A rise in the temperature caused by Joule heating during flash brought the system into the two-phase region in the phase diagram. In this two-phase region grain boundaries were liquid and rich in potassium whereas neighboring core was solid and deficient in potassium. The liquid at the boundaries increased conductivity (stronger Joule-heating) and the sintering rate. Compositional variation persisted during cooling thereby creating a core-shell microstructure.

4.5. Conclusions

When KNN polycrystalline compacts were flash sintered at 990°C in 30 seconds 94% of theoretical density was obtained. Similar densities can only be obtained at 1100 °C and after 2-8 of conventional sintering. Core-shell like chemical disproportionation was observed by SEM-EDX studies where the shell was rich in K and the inner layers were rich in Na. Joule-heating driven selective grain boundary melting which was one of the proposed mechanisms to explain flash sintering in the literature, appears to be the reason of this core-shell like structure. EDX quantification showed that Na/K+Na ratio in the shell was on the average 43% whereas in the core it was around 60.5%. The coexistence of these compositions in the (molten/re-crystallized) shell and in the (solid) core regions would correspond to an effective temperature of ~1150 °C in the existing $KNbO_3$-$NaNbO_3$ binary phase diagram. This temperature is in the liquid+solid two phase region for a starting composition of 50:50 $KNbO_3$ and $NaNbO_3$. During the flash and consequent cooling diffusion between the shell and the core created a compositional variation. A heat treatment homogenized the Na/K ratio at 0.90 closer to the nominal value of 1.0. Additional diffusion during heat treatment let the system come to an equilibrium chemical composition with a more homogenous Na and K distribution. STEM-EDX analysis showed that this variation of Na and K was in an intra-grain level and it appeared to have led to a ordering (cation or octahedral tilt) along 002 direction in the Na rich core.

CHAPTER 5

5. FLASH SINTERING OF ALKALINE OR NIOBIUM EXCESS KNN

5.1. Abstract

Flash sintering experiment were done for stoichiometric, A excess and B excess compositions. Sintering conditions were 250 V/cm and 185V/cm electric field, 20 mA/mm^2 current density. Flash sintering temperature of A excess composition is 900°C for 250 V/cm. electric field. The temperature was lower than the temperature of stoichiometric composition which was 990°C and the temperature of B excess composition which was 950°C. A excess composition has the highest power dissipation 132 mW/mm^3. Isothermal experiment were conducted at 1000°C to find out the incubation times. The lowest incubation time 7 s. was recorded for A excess composition for 250 V/cm electric field. It was 37 s and 200 s. for B excess and stoichiometric compositions, respectively. Power dissipation for AC field experiments were higher than DC field experiments.

5.2. Experimental

Stoichiometric ($K_{0.5}Na_{0.5}NbO_3$), alkaline (A site excess) and niobium (B site excess) excess powders were synthesized by conventional solid-state method. Calculated amounts of Na_2CO_3, K_2CO_3 and Nb_2O_5 were ball milled for 12 h in isopropanol

environment with zirconia balls. Prior to mixing the powders in stoichiometric ratios were dried for 3 h at 200°C to remove the adsorbed water from these compounds. KNN powders were synthesized at 800°C for 2 h. After mixing the synthesized powders with binder, 2 wt% polyvinyl butyral (PVB), dog bone-shaped specimens were uniaxially pressed at 200 MPa. The gauge section of the dog bone was 20mm x 3.5mm x 1.2 mm. The green density of the sample was around 0.63. Samples were held at 550°C for 1 h. for binder burn out.

Constant heating rate experiments were conducted by applying a DC voltage to the specimen while the furnace temperature was increasing at a constant heating rate. Isothermal experiments were conducted by applying a DC voltage to the specimen when the sample reach at a constant temperature. AC field experiment were conducted by applying 185 V/cm AC electric-field to specimen while the furnace temperature was increasing at a constant heating rate.

Specimen temperatures were estimated from Black-Body radiation model. Steady-state power density values were used to calculate the specimen temperature. According to the model, relation between the specimen temperature and furnace temperature is given by the formula

$$\frac{T^*}{T} = \left[1 + \frac{1000W}{\sigma T_0^4}\left(\frac{V}{A}\right)\right]^{1/4}$$

where To is the furnace temperature (K), T* is the specimen temperature (K), Wv is the power dissipation per unit volume of the specimen (mW/mm^3), V/A is volume to surface area of the specimen and is the blackbody radiation constant equal to 5.67 x $10^{-8} W/(m^2K^4)$). Structural characterization was performed by using X-ray powder diffractometer, (Bruker AXS D8 Advance, Karlsruhe, Germany), by using CuKα radiation. SEM micrographs and chemical analysis were done by SEM JEOL 6010 LV equipped by EDX detector. Polished (down to 1 μm by diamond paste) surfaces were examined by secondary electron mode.

5.3.Results

Fig.5.1 shows the power density values for excess A site, excess B site and stoichiometric compositions. For 185 V/cm values are very closer to each other. As the electric field increased from 185 to 250 V/cm separation in the values are more distinct. For 250 V/cm excess A site composition has the highest value and stoichiometric composition has the lowest value.

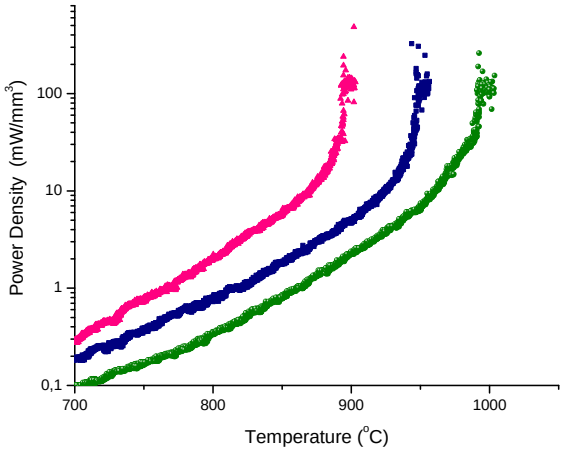

a)

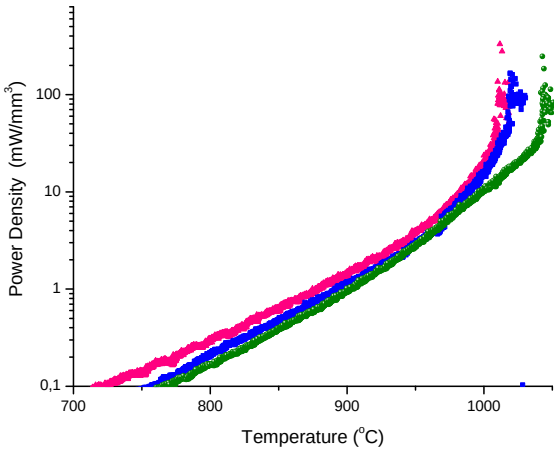

b)

Fig.5.1. Power densities for different compositions at a) 250 V/cm and b) 185 V/cm electrical fields for constant heating rate experiments

Both 185 V/cm and 250 V/cm electric fields, as the temperature increases flash is observed in excess A composition, excess B composition, and stoichiometric composition, respectively. Highest temperature is reached in stoichiometric composition for both fields depending on the black body radiation model. Power dissipation, flash temperature and calculated specimen temperature values are shown in Table 5.1.

Table 5.1. Power dissipation, flash temperature and calculated specimen temperature

	Flash Temperature (îC)		**Power Dissipation (mW/mm^3)**		**Specimen Temperature (îC)**	
Electric Field	250 V/cm	185 V/cm	250 V/cm	185 V/cm	250 V/cm	185 V/cm
Stoichiometric	990	1040	109	80	1096	1120
A excess (Na-K)	900	1010	132	82	1057	1094
B excess (Nb)	950	1020	117	88	1070	1110

Density values are calculated by Image Analysis Program and shown in Table 5.2. Highest shrinkage was observed for excess A and B compositions. SEM micrograph in Fig.5.2.

Table 5.2 :Density of the samples flash sintered (CHR) at 185 V/cm-20 mA/mm^2

Composition	**Density (T.D) (Image Analysis)**
Stoichiometric	0.89±1.3
A Site excess	0.91±0.9
B Site excess	0.91±0.5

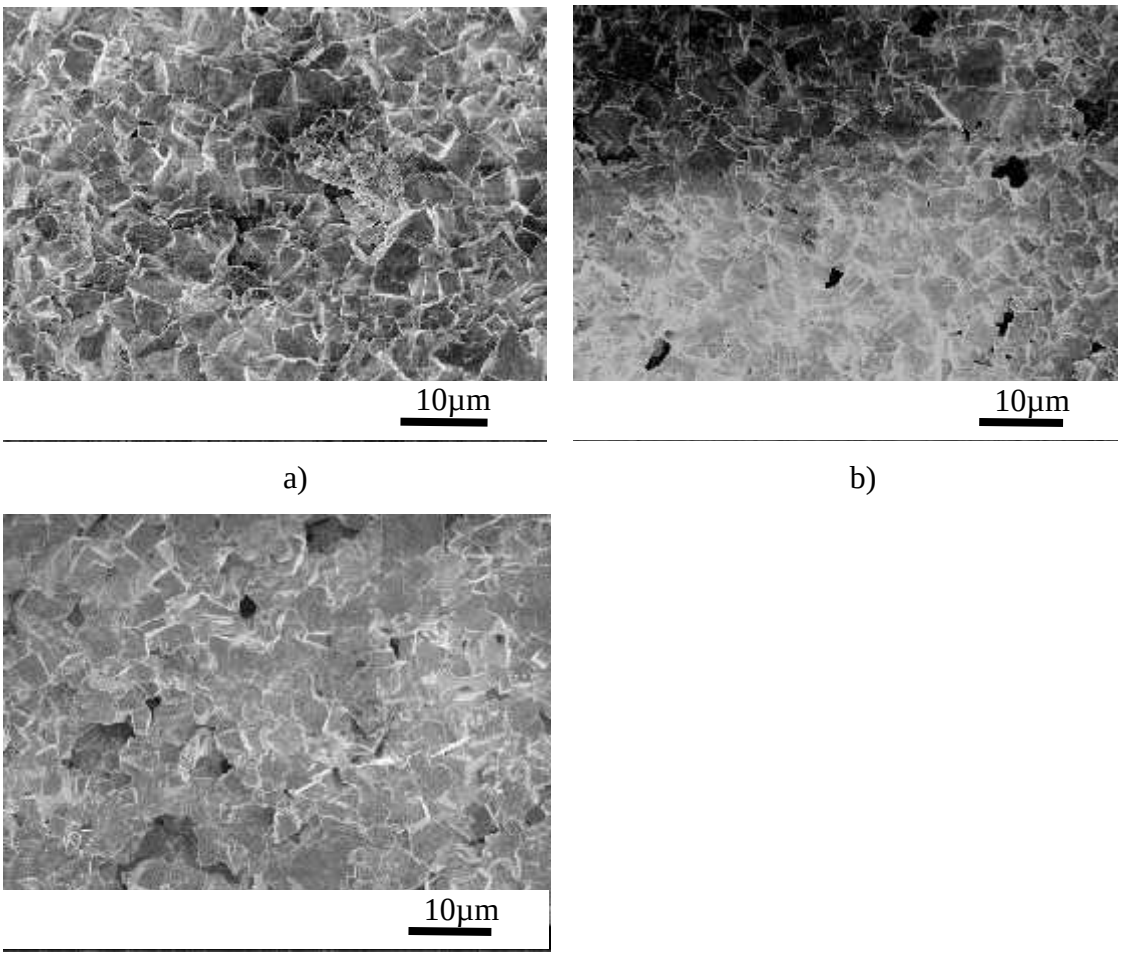

Fig 5.2: SEM micrographs of the flash sintered samples at 250 V/cm,20 mA/mm^2 a) A site excess, b) B site excess c) stoichiometric composition

Fig. 5.3. and Fig. 6.4 showed the EDX elemental mapping (Na and K distribution) of A excess and B excess composition. They resembled a core-shell structure Na in the core and K in the shell.

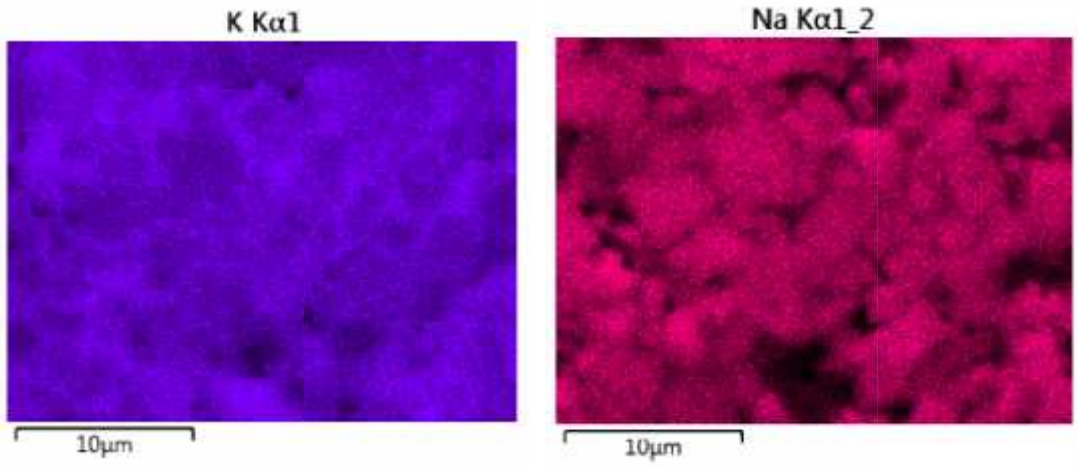

Fig.5.3: Elemental mapping of Na and K for flash sintered A excess sample at 185V/cm electric-field, 20mA/mm^2 for 30 s.

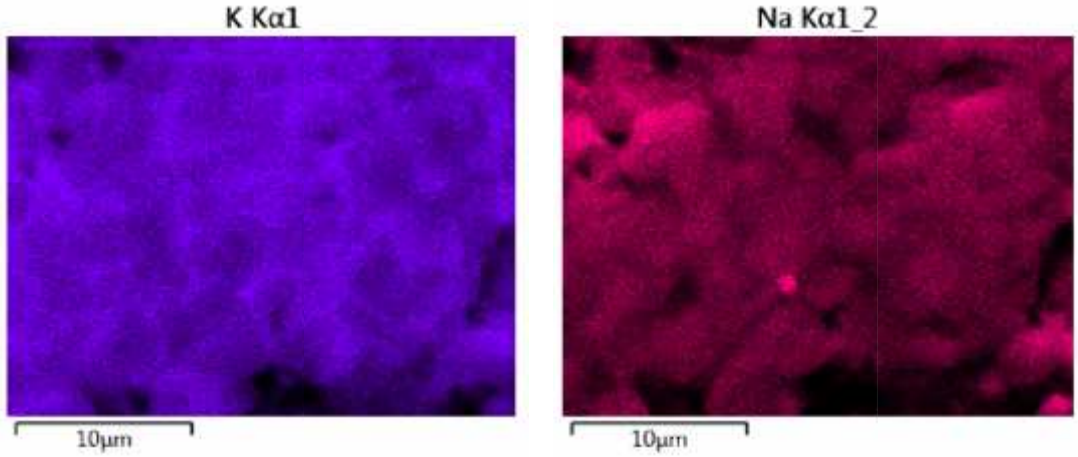

Fig.5.4: Elemental mapping of Na and K for flash sintered B excess sample at 185V/cm electric-field, 20mA/mm2 for 30 s.

5.3.2. Isothermal Experiments

Flash sintering experiments were applied at constant temperature. Samples were heated to 1000°C, and waited for stabilization of the temperature. After that electric field was applied to the sample. Power dissipation, flash temperature and calculated specimen temperature are shown in Table 5.3.

Because the sample kept at constant temperature during flash sintering, power dissipation values and specimen temperature values are very close to each other for

every composition when different electric fields are applied. The lowest power dissipation value is observed in excess A composition whereas the highest power dissipation value is observed in B excess composition.

Table 5.3. Power dissipation and calculated specimen temperatures for isothermal experiments

	Power Dissipation (mW/mm^3)				**Specimen Temperature (îC)**		
	200 V/cm	240 V/cm	250 V/cm	300 V/cm	240/200 V/cm	250 V/cm	300 V/cm
Stoichiometric	-	137	108	103	1118	1103	1085
A excess (Na-K)	94	-	96	94	1089	1095	1089
B excess (Nb)	-	88	115	115	1084	1105	1107

Incubation time is the time required the flash to happen after the application of electric field at constant temperature. Table 5.4. shows the incubation times of samples for different compositions. At constant temperature as the field increased incubation time was reduced. For 300 V/cm electric field it takes 5 s. to flash for excess A site composition. It was observed that for stoichiometric and excess B composition at 200 V/cm electric field, incubation times were larger than 1 hr.

Table 5.4. Incubation times for stoichiometric, A excess and B excess compositions for different electric fields at

	Incubation Time (s.)			
Electric Field (V/cm)	200	240	250	300
Stoichiometric	>1 hr	967	200	27
A excess (Na-K)	25	-	7	5
B excess (Nb)	>1hr	39	37	6

5.3.3. AC Experiments

AC electric field experiments were done for 185 V/cm- 24 mA/mm^2 for different compositions. Square wave form was applied with a frequency of 1000 kHz. Voltage and current behavior were shown in Fig.5.5-a) .Voltage was set for 370 V. First 200 data on x-axis shows the voltage behavior before the flash event for one of the data set. After flash temperature was reached, system switched to current control. This region was shown on x-axis between the data 200 and 400. Same phenomenon was valid for current behavior in Fig. 5.5- b) . Power dissipation, flash temperature and calculated specimen temperature values were shown in Table 5.5. Highest flash temperature were observed for B site excess composition.

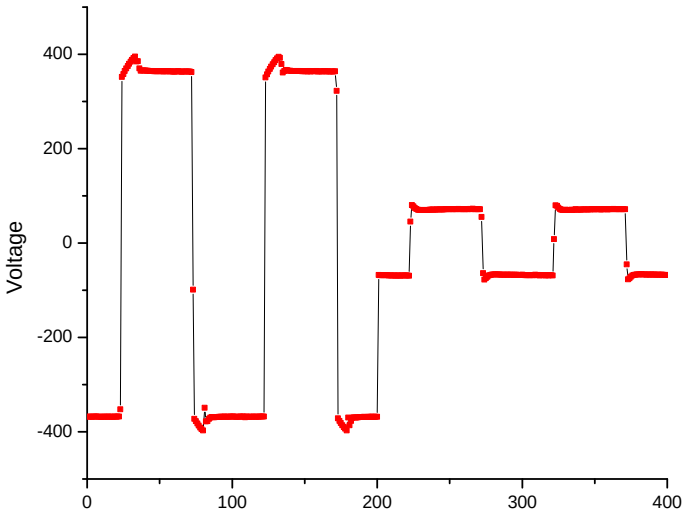

a)

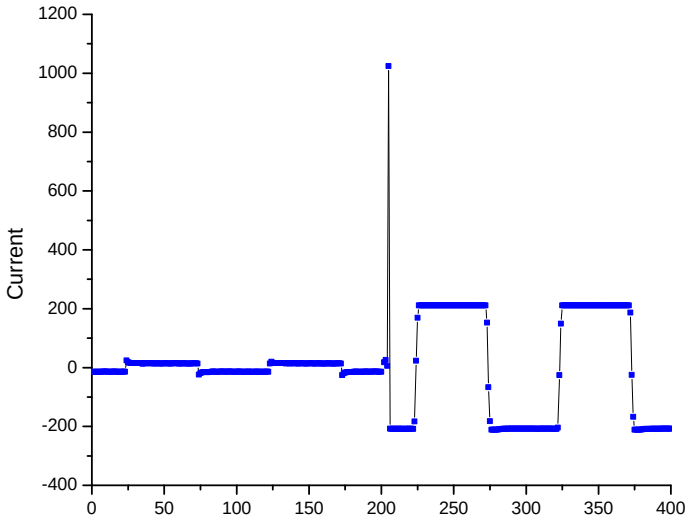

b)

Fig.5.5, a)Voltage and b) current behavior before and during flash for AC electric field (Range between 0-200 refers to voltage control region, range between 200-400 refers to current control region).

Table 5.5. Power dissipation, flash temperature and calculated specimen temperature

AC-Electric Field 185 V/cm

	FlashTemperature (îC)	**Power Dissipation (mW/mm^3)**	**SpecimenTemperature (îC)**
Stoichiometric	996	98	1138
A excess (Na-K)	970	113	1138
B excess (Nb)	1027	89	1150

SEM micrographs of the flash sintered samples with different compositions were shown in Fig.5.6. It was shown that grain size and morphology of the samples were similar.

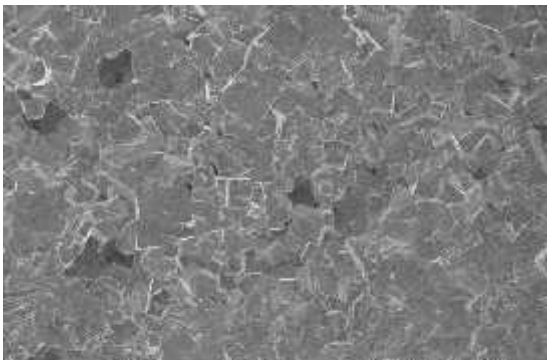

a)

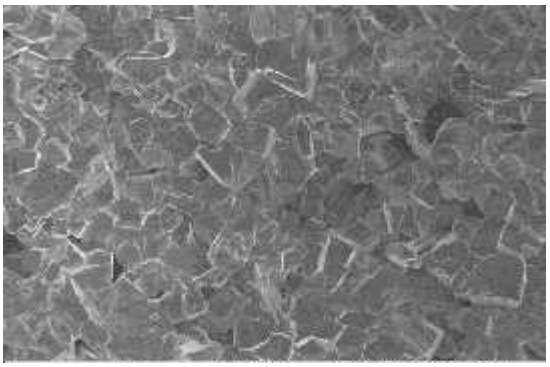

b)

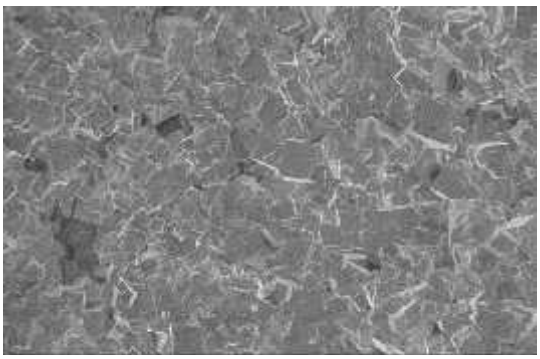

c)

Fig.5.6. SEM micrographs of the flash sintered samples at 185 V/cm, 24 mA/mm^2 at AC field a) stoichiometric composition, b) A site excess, c) B site excess

Table 5.6 :Density of the samples flash sintered with AC electric field at 185 V/cm-20 mA/mm^2

Composition	**Density (T.D) (Image Analysis)**
Stoichiometric	0.91±0.8
A excess (Na-K)	0.94±1.1
B excess (Nb)	0.91±0.9

Table 5.7 shows the comparison of flash temperatures between DC and AC electric. Although flash sintering temperature for AC field was lower than flash sintering

temperature for DC field for stoichiometric and A-site excess composition, it was comparable for B-site excess composition.

Table 5.7. Flash temperature comparison for DC and AC electric fields for stoichiometric composition.

	Flash Temperature (îC)	
Electric Field	**AC-185 V/cm**	**DC-185 V/cm**
Stoichiometric	996	1040
A excess (Na-K)	970	1010
B excess (Nb)	1027	1020

5.4. Discussions

Flash sintering temperature of A excess composition is 900°C and it was lower than B excess and stoichiometric composition for 250 V/cm. electric-field. Flash sintering occurs at 990°C for stoichiometric composition and at 950°C for B excess composition. Same sequence was observed when the electric-field was lowered to 185 V/cm. Flash sintering temperatures were 1010°C, 1020°C and 1040°C for A excess, B excess and stoichiometric compositions, respectively. The magnitude of power dissipations were in the range of 80-90 mW/mm^3 at 185 V/cm. and 110-120 mW/mm^3 for 250 V/cm. Highest density was obtained for A excess KNN. Microstructure of all three compositions were homogenous. Abnormal grain growth did not observed.

EDX analysis showed that there was Na and K variation in the composition that resembled a core shell structure after flash sintering. It may be linked to grain boundary melting during flash via joule heating.

Isothermal experiment showed that A excess composition has the shortest incubation time (7 s) compared to B excess (37 s) and stoichiometric (200 s) KNN for 250 V/cm. electric-field.

The flash sintering temperature of AC field experiments showed the same sequence with DC field experiment for different compositions. Highest sintering temperature was observed for stoichiometric KNN and the lowest sintering temperature was observed for A excess KNN. Power dissipation values of AC field experiment were higher than DC field experiment. This indicate that resistance was slightly higher for AC experiments during flash.

5.5. Conclusions

Conventional sintering experiments showed that A excess KNN has the lowest sintering temperature and B excess KNN has the highest sintering temperature. However, in flash sintering A excess KNN has the lowest sintering temperature and highest density. Stoichiometric KNN has the highest sintering temperature independent from magnitude or characteristic (DC or AC) of applied electric-field. The non-stoichiometry in B excess composition favored the flash event. B excess composition was used to create A site vacancies to favor diffusion and densification for conventional sintering. Isothermal experiments showed that A excess composition has the lowest incubation time. A excess composition sintered with AC electric field has lower flash temperature and higher density.

CHAPTER 6

6. CONCLUSION

Compositional variation during synthesis of KNN was linked to larger grain size of monoclinic Nb_2O_5 powder compared to the smaller grain size of orthorhombic Nb_2O_5 powder, higher reaction rate of Na_2CO_3/Nb_2O_5 diffusion couple compared to K_2CO_3/Nb_2O_5 and Hedwall effect.

Grain size of KNN powder increased as the alkaline amount increased.

Dilatometer analysis showed that sintering temperature decreased as the alkaline amount increased. Two shrinkage rate peaks were observed for A-site excess composition whereas a single shrinkage rate peak (higher temperature peak) was observed for stoichiometric ($K_{0.5}Na_{0.5}NbO_3$) and B-site excess compositions.

First shrinkage rate peak during sintering was explained by water soluble alkaline excess. The intensity of the low temperature shrinkage rate peak correlated with the amount of alkaline excess. Liquid formation during sintering explained by the eutectic formation by Na_2CO_3-K_2CO_3 system. Liquid film formed during initial stages of sintering facilitated the rearrangement of the grains. Transient liquid phase sintering was proposed as the active sintering mechanism for alkaline excess compositions

Flash sintering experiments were conducted to KNN for the first time. 94% Th.D was obtained in 30 s. at 250V/cm electric-field and 20 mA/mm^2 current density. EDX analysis showed that there was a core-shell structure Na rich in the core and K rich in the shell. This core shell structure disappeared after heat treatment. The maximum temperature reached was estimated around 1150 C° depending on EDX quantification results and binary phase diagram ($KNbO_3$-$NaNbO_3$). A new model was proposed to explain the core-shell formation. According to this model core-shell was formed due to grain boundary melting via Joule heating.

TEM Dark field and STEM-EDX analysis showed that chemical boundaries were not grain boundaries as expected. Chemical inhomogeneity was within the grain. Diffraction pattern of Na regions showed extra spots which may be related to octahedral tilting or cation ordering.

The lowest flash sintering temperature was obtained for alkaline rich KNN under DC and AC electric-fields. Shortest incubation time was obtained for alkaline rich KNN.

Obtaining fully dense KNN ceramics with an energy efficient (low temperature, shortest time- 30s.- in air) method will make a positive impact on the race of lead-free piezoelectric industry.

Further analysis will focus on the role of electric field on the sintering and electrical properties of KNN. Impedance analysis will be done, diffraction pattern simulations will be done to find out the reason of the extra spots and STEM-EDX composition profiles will be improved.

CHAPTER 7

7. REFERENCES

1- T.L. Jordan, Z. Ounaies, "Piezoelectric Ceramics Characterization", ICASE, Hampton, Virginia, NASA/CR-2001-211225,ICASE Report No. 2001-28, 2001

2- B. Jaffe, H. Jaffeand and W. R. Cook, "Piezoelectric ceramics", Academic Press, London (1971).

3- D. Vatansever, E. Siores and T. Shah, "Alternative Resources for Renewable Energy:Piezoelectric and Photovoltaic Smart Structures", http://dx.doi.org/10.5772/50570

4- https://www.americanpiezo.com/knowledge-center/piezo-theory

5-Ballato A., "Piezoelectricity: History and New Thruts", IEEE Ultrasonic Symposium, 575-583, 1996

6-http://www.rsc.org/chemistryworld/News/2012/March/improved-solar-cell efficiency.asp

7-http://www.idtechex.com/research/articles/piezoelectric-energy-harvesting developments-challenges-future-00005074.asp

8- Gene H. Haertling, "Ferroelectric Ceramics: History and Technology", *J. Am. Ceram. Soc.*, 82 [4] 797–818 (1999)

9- Pena M.A., Fierro J.L.G., "Chemical Structures and Performance of Perovskite oxides", Chem. Rev. 2001, 101, 1981-2017

10- J. Rödel, W. Jo, K. T. P. Seifert, E. M Anton and T. Granzow, "Perspective on the Development of Lead-free Piezoceramic", J. Am. Ceram. Soc., 92, 11531177 (2009).

11-Kang Suk-J.L., "Sintering, Densificaiton Grain Growth Microstructure", Elsevier, (2008)

12- M.H. Rahaman, "Ceramic Processing and Sintering of Ceramics", Marcel Dekker Inc, 2nd Edition, (2003)

13- German R.M., Suri P., Park S.J., "Review: Liquid Phase Sintering", J Mater Sci.,44,1–39, (2009)

13- Guillon O., Julian J.G., Dargatz B., Kessel Tobias, Schierning G., Rathel j., Herrmann M. "Field Assisted Sintering Technology/ Spark Plasma Sintering: Mechanisms, Materials, and Technology Developments", Advanced Engineering Materials, (2014)

14- K. Wang and J.-F. Li, "(K,Na)NbO3-based lead-free piezoceramics:Phase transition, sintering and property enhancement", J. Advanced Ceramics, 1, 24-37 (2012).

15- Panda, P.K., "Review: environmental friendly lead-free piezoelectric materials", J Mater Sci (2009) 44:5049–5062

16- C. Sen, B. Alkan, I. Akın, O. Yucel, F. C. Sahin and G. Goller, "Microstructure and ferroelectric properties of spark plasma sintered Li substituted $(K_{0.5}Na_{0.5})NbO_3$ ceramics", J. Ceram. Soc. Japan, 119, 355-361, (2011).

17- M. Cologna, B. Rashkova and R. Raj, Flash sintering of nanograin zirconia in<5 s at 850◦C, J. Am. Ceram. Soc., 93,3556-3559, (2010).

18- R. Raj, M. Cologna and J. S. C. Francis, "Influence of externally imposed and internally generated electrical fields on grain growth, diffusional creep, sintering and related phenomena in ceramics", J. Am. Ceram. Soc., 94, 1941-1965, (2011).

19- R. Raj, "Joule heating during flash-sintering", J. Eur. Ceram. Soc., 32, 2293-2301, (2012).

20- H. Yoshida, Y. Sakka, T. Yamamoto, J.-M. Lebrun and R. Raj, "Densification behaviour and microstructural development in undoped yttria prepared by flash-sintering", J. Eur. Ceram. Soc., 34, 991-1000, (2014).

21- M. Cologna, J. S. C. Francis and R. Raj, "Field assisted and flash sintering of alumina and its relationship to conductivity and MgO-doping", J. Eur. Ceram. Soc., 31, 2827-2837, (2011).

22- A. L. G. Prettea, M. Cologna, V. Sglavoa and R. Raj, "Flash-sintering of Co_2MnO_4 spinel for solid oxide fuel cell applications" J. Power Sources, 196, 2061-2065, (2011).

23- E. Zapata-Solvas, S. Bonilla, P. R. Wilshaw and R. I. Todd, "Preliminary investigation of flash sintering of SiC", J. Eur. Ceram. Soc., Short communication 33, 2811-2816, (2013).

24- A. Karakuscu, M. Cologna, D. Yarotski, J. Won, J. S. C. Francis, R. Raj and B. P. Uberuaga, "Defect Structure of Flash-Sintered Strontium Titanate", J. Am. Ceram. Soc., 95, 2531-2536, (2012).

25- S. K. Jha and R. Raj, "The Effect of Electric Field on Sintering and Electrical Conductivity of Titania", J. Am. Ceram. Soc., 97, 527-553, (2014).

26- Francis J.S.C., Raj. R., "Influence of the Field and the Current Limit on Flash Sintering at Isothermal Furnace Temperatures", J. Am. Ceram. Soc., 96 [9] 2754–2758 (2013)

27- J.-W. Jeong, J.-H. Han and D.-Y. Kim, "Effect of Electric Field on the Migration of Grain Boundaries in Alumina", J. Am. Ceram. Soc., 83, 915-918 (2000).

28- V. Ravikumar, R. P. Rodrigues and V. P. Dravid, "Space-Charge Distribution across Internal Interfaces in Electroceramics Using Electron Holography: II, Doped Grain Boundaries", J. Am. Ceram.Soc., 80, 1131-1138 (1997).

29- J. Narayan, "A new mechanism for field-assisted processing and flash sintering of materials", Scr. Mater., 69, 107-111 (2013).

30- Y. Zhang, J.-I. Jung and J. Luo, "Thermal runaway, flash sintering and asymmetrical microstructural development of ZnO and ZnO–Bi2O3 under direct currents", Acta Mater., 94, 87-100 (2015).

31- Zhang S., Xia R., Shrout T.R., "Lead free piezoelectric ceramics vs. PZT", J. Electroceram 19, 251-257, (2007),

32- Koruza J., Malic B., "Initial stage sintering mechanism of $NaNbO_3$ and implications regarding the densification of alkaline niobates" J.Eur. Ceram. Soc., 34,1971–1979, (2014).

33- Hrescak J., Bencan A., Rojac T., Malic B., "The influence of different niobium pentoxide precursors on the solid-state synthesis of potassium sodium niobate", J.Eur. Ceram. Soc. 33, 3065–3075, (2013)

34- Du H., Li Z., Tang F., Qu.S., Pei Z. Zhoua W., "Preparation and piezoelectric properties of (K0.5Na0.5)NbO3 lead-free piezoelectric ceramics with pressure-less Sintering", Mater. Sci. and Eng. B 131, 83–87, (2006)

35- Fisher J. G., Kang S-J.L., "Microstructural changes in $(K_{0.5}Na_{0.5})NbO_3$ ceramics sintered in various atmospheres, J.Eur. Ceram. Soc. 29, 2581–2588, (2009)

36- Wanga D., Zhua K., Jia H., Qiua J., "Two-Step Sintering of the Pure $K_{0.5}Na_{0.5}NbO_3$ Lead-Free Piezoceramics and Its Piezoelectric Properties Ferroelectrics", 392, 120–126, (2009)

37- Acker J., Kungl H., Hoffmann M.J., "Influence of Alkaline and Niobium Excess on Sintering and Microstructure of Sodium-Potassium Niobate $(K_{0.5}Na_{0.5})NbO_3$", J. Am. Ceram. Soc., 93, 5, 1270–1281, (2010)

38- Zheng L., Wang J., "Received:Nonstoichiometric $(K_{0.5}Na_{0.5})NbO_3$ ceramics: Densification and electrical properties", J. Electroceram 32,192–198, (2014)

39- Ringgaard E., Wurlitzer, T., "Lead-free piezoceramics based on alkali niobates", J. Eur. Ceram. Soc., 25, 2701-2706 (2005).

40- Zhang S., Xia R. , Shrout T.R., "Lead-free piezoelectric ceramics vs. PZT?" J. Electroceram., 19, 251-257(2007).

42- Fang J., Wang X., Tian Z., Zhong C., Li L., "Two-Step Sintering: An Approach to Broaden the Sintering Temperature Range of Alkaline Niobate-Based Lead-Free Piezoceramics", J. Am. Ceram. Soc., 93, 11, 3552–3555, (2010)

43- Hollenstein E., Davis M., Damjanovic D., Setter N., "Piezoelectric properties of Li- and Ta-modified $(K_{0.5}Na_{0.5})NbO_3$ ceramics", Applied Physics Letters, 87, 182-905 (2005).

44- E. Mensur Alkoy and M. Papila, "Microstructural features and electrical properties of copper oxide added potassium sodium niobate ceramics", Ceram. Int., 36, 1921-1927, (2010).

45- Zuo R., Rödel J., Chen R., Li.L., "Sintering and Electrical Properties of Lead-free $Na_{0.5}K_{0.5}NbO_3$ Piezoelectric Ceramics", J.Am.Ceram.Soc., 89, 6, 2010-2015, 2006

46- Lanfredi S. , Dessemond L., Rodrigues A.C.M., "Dense ceramics of $NaNbO_3$ produced from powders prepared by a new chemical route",J. Eur. Ceram. Soc., 20, 983-990, (2000)

47- Ravi B.G., Chaim R. Gedanken A., "Sintering of Bimodal Alumina Powder Mixtures with a Nanocrystalline Component", NanoStructured Materials, 11, 7, 853–859, (1999)

48- Tajika M., Rafaniello W., Niihara K., "Sintering behavior of direct nitrided AlN powder", Materials Letters 46, 98–104, (2000)

49- Wang X.X., Mukarami K., Sugiyama O., Kaneko S., "Piezoelectric Properties, Densification Behavior and Microstructural Evolution of Low Temperature Sintered PZT Ceramics with Sintering Aids", J. Eur.Ceram.Soc., 21,1367-1370, (2001)

50- Chick L.A., Liu J., Stevenson J.W., Armstrong T.R., Mc Cready D.E., Maupin G.D., Coffey G.W., Coyle C.A., "Phase Transitions and Transient Liquid-Phase

Sintering in Calcium Substituted Lanthanum Chromite", J. Am. Ceram. Soc., 80, 8, 2109–20, (1997)

51- Kanka B., Schneider H., "Sintering Mechanisms and microstructural develeopment of coprecipitated mullite", J.Mater.Sci., 29, 1239-1249, (1994)

52- Stevenson A.J., Kupp E.R., Messing G.L., "Low temperature, transient liquid phase sintering of B_2O_3-SiO_2- doped Nd:YAG transparent ceramics", J. Mater. Res., 26, 9, (2011)

53- Malic B., Jenko D., Holc J., Hrovat M., Kosec M., "Synthesis of Sodium Potassium Niobate: A Diffusion Couples Study", J. Am. Ceram. Soc., 91,6, 1916–1922, (2008

54- Jaeger, R. E., Egerton, L., "Hot Pressing of Potassium Sodium Niobates", J. Am. Ceram. Soc., 45, 209–213, (1962),

55- Birol H. Damjanovic D., Setter N., "Preparation and Characterization of ($K_{0.5}Na_{0.5}NbO_3$) Ceramics J. Eur. Ceram.Soc. 26, 861–866, (2006)

56- http://www.chemicalbook.com/ChemicalProductProperty_EN_CB32702659.htm

57-Zhao Y., Zhou X., Lin Ye L., Tsang S.C.E., " Nanostructured Nb2O5 catalysts", Nano Reviews 2012, 3: 17631

58- B.D. Cullity, "Elements of X-Ray Diffraction", Addison-Wesley Publishing, (1956)

59- Brandon D., Kaplan W. D., "Microstructural Characterization Of Materials", 2nd Edition, Wiley, (2013).

60- Speyer R. F., "Thermal Analysis of Materials", Marcel Dekker Inc., (1993)

61- David B.; Williams, C. Barry Carter, "Transmission Electron Microscopy: A Textbook for Materials Science", Springer; 2nd edition. 2009

62- Glatz A.C., Pinella A., "Thermal Decomposition Studies of Sodium and Potassium Tartrates", Analytical Calorimetry, 3, 713-721, (1974)

63- Bomlai P., Wichianrat P., Muensit S.,Milne S.J., "Effect of Calcination Conditions and Excess Alkali Carbonate on the Phase Formation and Particle Morphology of $Na_{0.5}K_{0.5}NbO_3$ Powders", J. Am. Ceram. Soc., 90,5, 1650–1655, (2007)

64-Corbin S.F. , Mc Isaac D.J., "Differential scanning calorimetry of the stages of transient liquid phase sintering", Mater. Sci.and Eng. A346, 132-140, (2003)

65-German R. M., Dunlap J.W., "Processing of Iron-Titanium Powder Mixtures by Transient Liquid Phase Sintering", Metallurgical Transactions A, 17A, 205-213, (1986)

66- S. Sturm, A. Bencan, M. A. Gulgun, B. Malic and M. Kosec, "Determining the Stoichiometry of (K,Na)NbO_3 Using Optimized Energy-Dispersive X-Ray

Spectroscopy and Electron Energy-Loss Spectroscopy Analyses in a Transmission Electron Microscope, J. Am. Ceram. Soc., 94, 2633-2639 (2011).

67- D. I. Woodward and I. M. Reaney, "Electron Diffraction of Tilted Perovskites", Acta Crystallogr., Sect. B: Struct. Sci., 61, 387-399, (2005).

68- S. Zhang, H. J. Lee, C. Ma and X. Tan, "Sintering Effect on Microstructure and Properties of (K,Na)NbO_3 Ceramics", J. Am. Ceram. Soc., 94, 3659-3665 (2011).

69- S.-J. L. Kang, "Sintering Densification Grain Growth Microstructure", Elsevier (2005).

70- F. Zhu, M. B. Ward, J.-F. Li and S. J. Milne, "Core-shell grain structures and dielectric properties of $Na_{0.5}K_{0.5}NbO_3$–$LiTaO_3$–$BiScO_3$ piezoelectric ceramics" Acta Mater., 90, 204-212, (2015).

71- S.-C. Jeon, C.-S. Lee and S.-J. L. Kang, "The Mechanism of Core/Shell Structure Formation During Sintering of BaTiO3-Based Ceramics", J. Am. Ceram. Soc., 95, 2435-2438, (2012).

72- C. A. Randall, S. F. Wang, D. Laubscher, J. P. Dougherty and W. Huebner, "Structure property relationships in core-shell $BaTiO_3$-LiF ceramics", J. Mater. Res., 8, 871-879, (1993).

73- H. Y. Lu, l. S. Bow and W. H. Deng, "Core-Shell Structures in ZrO_2-Modified $BaTiO_3$Ceramic", J. Am. Ceram. Soc., 73, 3562-3568 (1990).